Lava Flow Hazard Assessment for the Idaho National Laboratory, Idaho Falls, and

Pocatello, Idaho, U.S.A.

by

Elisabeth Gallant

A thesis submitted in partial fulfillment
of the requirements for the degree of
Master of Science
School of Geosciences
College of Arts and Sciences
University of South Florida

Major Professor: Charles Connor, Ph.D.
Paul Wetmore, Ph.D.
Sylvain Charbonnier, Ph.D.

Date of Approval:
October 31, 2016

Keywords: Eastern Snake River Plain, Spatial Density, Volcanic Event, Eruption Model,
Inundation Probability

TABLE OF CONTENTS

LIST OF FIGURES

LIST OF TABLES

Abstract

This study presents a probabilistic lava flow hazard assessment for the Idaho National Laboratory (INL) and the cities of Idaho Falls and Pocatello, Idaho. The impetus of this work is to estimate the conditional probability that a lava flow on the eastern Snake River Plain (ESRP) will impact the areas of interest given the formation of a new volcanic vent in the region. A list of 288 eruptive events, derived from a previously published inventory of 506 surface and 32 buried vents, was created to reduce the biasing of spatial density maps towards eruptions with multiple dependent vents. Conditional probabilities of new vents and events occurring on the ESRP were modeled using the the Sum of Asymptotic Mean Squared Error (SAMSE) optimal pilot bandwidth estimator with a bivariate Gaussian kernel function. Monte Carlo analyses of potential eruption scenarios were performed using MOLASSES, a cellular automata fluid flow simulator. Results show that Idaho Falls is impacted <1% of the time for both the vent and event simulations; Pocatello is not impacted by any simulated flows. 25.45% of vent flows and 33.74% of event flows breach the boundaries of INL. 18.27% of vent and 25.85% of event simulations initiate on the INL property. Annual inundation probabilities of 1.06 x 10^{-4} for vent-based flows and 7.12 x 10^{-5} for event-based flows are reported for INL; annual probabilities of an eruptive center initiating on INL property are 7.60 x 10^{-5} for vents and 5.45 x 10^{-5} for events. All of these values exceed the International Atomic Energy Agency's acceptable risk probability of 10^{-7} by several orders of magnitude.

1. Introduction

The intersection of nuclear facilities and natural hazards has been thrust into the public awareness since the 2011 Tōkohu, Japan earthquake and subsequent tsunami claimed the lives of 15,894 individuals. Although no deaths have been directly attributed to the resultant nuclear disaster, cancer rates are expected to climb within the region as time progresses, especially in younger demographics (World Health Organisation, 2013). This tragedy highlights the need for accurate assessments of natural hazards and plans that incorporate them when designing nuclear facilities and selecting their locations.

Volcanoes, like earthquakes and tsunamis, have the ability to cause extreme devastation in a short period of time. Hazards associated with volcanoes include lava flow, seismic activity, ground deformation, gas emission, ballistic impact, tephra fallout, pyroclastic density current, flank failure, tsunami, and more. Volcanic hazard assessments are designed to qualify and/or quantify the potential impacts of volcanic eruptions (Connor and Hill, 1995; Bebbington and Lai, 1996; Hill et al., 1998; Martin et al., 2004; Weller, 2004; Turner et al., 2008; Mahony et al., 2009; Bebbington and Cronin, 2011; Marzocchi and Bebbington, 2012; Sandri et al., 2012). They may also be utilized to increase awareness of the possible destructive effects of future volcanic activity at a variety of timescales. Long-term forecasts often depend on statistical modeling of the distribution of past volcanic events, the timing of these events, and their volume or magnitude.

This study joins a suite of other hazard assessments for INL and the ESRP, but is the first long-term forecast to use computational models to predict the area of inundation for future lava flows. This work uses published data on ESRP eruptive centers and incorporates this information into spatial density models following the approach of Wetmore et al. (2009).

Potential future vents were selected from these models and were then input into a lava flow simulator. The conditional probabilities of lava flow inundation of INL and two large municipalities on the eastern ESRP was then resolved. The outcome of this study can help stakeholders assess the scale of lava flow hazards on the plain.

2. Background Information and Review of Literature

2.1 Tectonic and Geologic Setting of Southern Idaho

Topography in southern Idaho is controlled by two major ongoing forces: crustal extension and the passage of the North American plate over a mantle plume currently seated below the Idaho-Montana-Wyoming boarder (Rodgers et al., 2002). Extensional tectonics pre-date the emergence of the Yellowstone Hotspot (YSHS) in southern Idaho by ~7 Ma, resulting in the overprinting of surficial features and subsurface structures of the Basin and Range by the track of the YSHS (Kuntz et al., 1982, 1992).

2.1.1 The Yellowstone Mantle Plume and Hotspot

The concurrent eruptions of the McDermitt caldera and Columbia River Flood Basalts mark the emergence of the YSHS at the surface in both space and time. These eruptions occured ~17 Ma and are located on Figure 2.1. As the North American plate moves over the mantle plume, the volcanic centers migrate progressively eastward. Understanding the impact the transit of the YSHS has had on the region is important because it is responsible for the creation of the ESRP.

The caldera within Yellowstone National Park is a small component of the current YSHS system. The three most recent eruptive centers, Huckleberry Ridge (2.0 Ma), Mesa Falls (1.29 Ma), and Lava Creek (0.6 Ma), all reside atop the current location of the mantle plume and form a topographic high within the region. The heat imparted to the base of the crust from the mantle plume, the temperature differential between the injected magma and the surrounding rock, and the increase in rock volume from this injection causes the overlying lithosphere to expand and swell, manifesting on the surface as a broad plateau (Pelton and Smith, 1979; Leeman, 1982a). The Yellowstone plateau rises abruptly to an
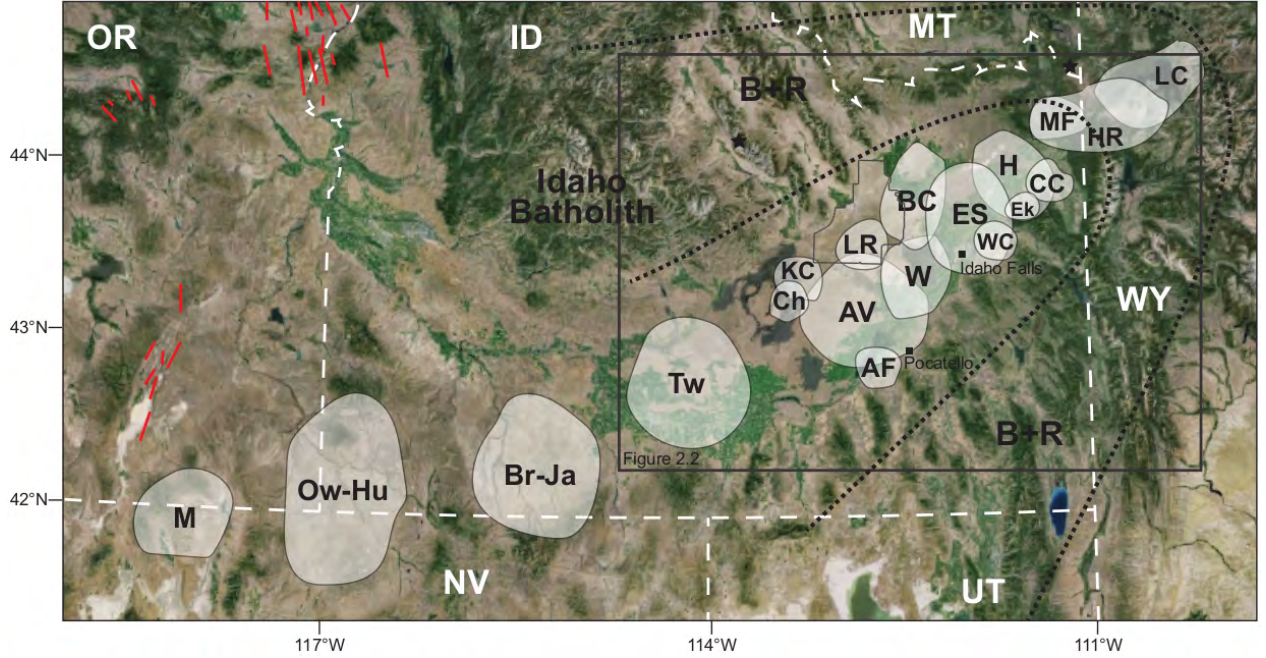
Figure 2.1: Satellite image of southern Idaho with past calderas of the Yellowstone hotspot illustrated, adapted from Anders et al. (2009). The boundary of INL is shown with a black line near the caldera marked 'LR'. The dotted line notes the seismically active zone around the ESRP, discussed in the 'Extension of southern Idaho' section. The black star within Idaho indicates the location of the 1983 Mw 6.9 Borah Peak earthquake. The black star on the Idaho-Montana-Wyoming boarder indicates the location of the 1959 Mw 7.3 Hebgen Lake earthquake. The red lines indicate dike swarms associated with the Columbia River Flood Basalts. The black box outlines the extent of Figure 2.2. M = McDermitt (16.1 Ma); Ow-Hu = Owyhee-Humbolt (13.9-12.8 Ma); Br-Ja = Bruneau-Jarbridge (12.8-10.0 Ma); Tw = Twin Falls (10.0-8.6 Ma); AV = Arbon Valley (10.27-10.09 Ma); Ch = Chokecherry Canyon (9.34 Ma); KC = Kyle Canyon (9.17 Ma); LR = Lost River Sinks (8.75 Ma); AF = America Falls (7.48 Ma); BC = Blue Creek (6.19 Ma); W = Walcott (6.19 Ma); CC = Conant Creek (5.94 Ma); Elkhorn Springs (5.37 Ma); H = Heise (4.49 Ma), HR = Huckleberry Ridge (2.0 Ma), MF = Mesa Falls (1.29 Ma); LC = Lava Creek (0.6 Ma).

4

elevation 400 m above the adjacent segment of the ESRP at Henry's Fork near Ashton, Idaho. The topographic anomaly is so great that it affects the drainage systems of the area, with the location of the Continental Divide corresponding to its migration. This long-wavelength signal (600 km wide) is comparable with that of other known mantle plumes, such as the Cape Verde, Galapagos, Azores, and Hawai'i (Turcotte and Schubert, 2002). The geoid anamoly is greater still and extends to 1,000 km in width (Cochran and Talwani, 1977). The predecessors of Yellowstone were once similar in appearance and structure. When the motion of the North American plate transposes activity further east the previous section, now removed from the greatest extent of the thermal swelling, contracts and collapses (Brott et al., 1981). Subsidence of the ESRP occurs because of a combination of this process and isostatic loading due to higher density basaltic intrusive material (Brott et al., 1981; Leeman, 1982a; Anders and Sleep, 1992; McQuarrie and Rodgers, 1998; Rodgers et al., 2002). The ESRP is a curved topographic trough 50–100 km in width that extends for 350 km across southeastern Idaho and represents the track of the last 10 My of YSHS activity (Anders and Sleep, 1992).

Seismic tomography, aeromagnetic, and gravity methods have been used to image the ESRP and surrounding area at various depths. Crustal thicknesses are approximately 35, 45, and 50 km for the Basin and Range, ESRP, and Yellowstone areas, respectively (Sparlin et al., 1982; Braile et al., 1982; Greensfelder and Kovach, 1982). These varying depths are a direct result of the activity of the YSHS and widespread extension throughout the region (Greensfelder and Kovach, 1982; Shervais et al., 2006, 2008). These methods identified a velocity anomaly 12 km thick that resides beneath the ESRP at a depth of 8–20 km, inferred to be an intrusive mafic body (Sparlin et al., 1982; Braile et al., 1982). Correlating spatial relationships between surface and sub-surface features provide insight for the location of magma storage and transport through the lithosphere. Confirming the findings of this thesis with the results of these geophysical surveys imparts confidence into the process (Kinman-Tavarez, 2015). Models from these surveys can be found in Appendix A.

2.1.2 Extension of southern Idaho

Extension throughout the western United States began 28 Ma in the Mojave region (McQuarrie and Wernicke, 2005), reached central Nevada ~17 Ma (Allmedinger, 1982), and remains continuous through the present across Idaho, Nevada, Utah, and western Wyoming (Dixon et al., 1995). Intraplate extensional tectonics express topographically as linear valleys and mountain ranges bounded by normal faults. The extreme variation in landscapes between the Basin and Range and ESRP, the abrupt topographic transition between them, and the unique distribution of seismicity across them have raised questions regarding how extensional forces are accommodated throughout the area. An arcuate zone of seismic quiescence overlies the ESRP and is bounded by a parabolic region of increased seismic activity (Anders et al., 1989)(Figure 2.1). Assuming that the ESRP is experiencing the same stress regime as the surrounding Basin and Range, how is plain-wide extension being accommodated? Deciphering the partitioning of strain throughout the region aids in understanding the processes that allow for magma transport below the ESRP, which in turn control the locations of eruptions (Takada, 1994; Connor et al., 2000; Kiyosugi et al., 2010).

Aseismic creep, fault slip that occurs with no associated seismic event, was an early hypothesis to explain the aforementioned observations (Smith and Sbar, 1974). This was bound to the idea that heat from the YSHS weakened the crust to such an extent that it was no longer able to respond to extension through discrete brittle failure (Furlong, 1979). Brott et al. (1981) argue that this requires a mechanically decoupled boundary between the ESRP and the Basin and Range; strike-slip faulting or shear zones are the most likely expression of this decoupling. Although Payne et al. (2012) argue the existence of a shear zone inferred from geodetic data, no such structures have been identified, which suggests that the ESRP is likely coupled to its surroundings in some fashion (Anders and Sleep, 1992; Rodgers et al., 2002; Payne et al., 2012). Creep is not thought to occur on normal faults inside of the ESRP or within 20 km of its boundary because these faults do not show signs of recent offset (Anders and Sleep, 1992). A recent field study identified young scarps

(possibly Quaternary) along the fronts of the Lemhi and Lost River Ranges (Hemphill-Haley et al., 1994; Olig et al., 1995), but further examination is needed to confirm this (P. Wetmore, Personal Comm., May 2016). Regardless, Anders and Sleep (1992) assert that little evidence exists to suggest faulting structures from the Basin and Range extend into the ESRP; others argue the contrary (Kuntz et al., 1992), although Wetmore (1998) states that the presence of such faults would not play a major role in the distribution of volcanism in the region. This is demonstrated in Wetmore et al. (2009).

Another hypothesis explores the possibility of increased crustal resilience through extensive mafic intrusions as the mode of extensional adaptation. Anders and Sleep (1992) state that faulting in this area pre-dated the emergence of the hotspot and was eventually arrested by its passage. Early extension associated with an increase in tectonic strain due to the heating of the lithosphere from an influx of magma initially increased fault activity along the axis of the ESRP. This early, rapid extension was then followed by the crystallization of mafic magma at the base and mid-levels of the crust, which in turn slowly strengthened the ESRP (Anders et al., 1989). Laboratory experiments show that the maximum tensile strength of basalt (~60 MPa) would be greatly exceeded by the amount of strain accumulated over the 10 Ma period since the inception of volcanism in south-central Idaho (~600 MPa)(Okui and Horii, 1997). Although material strength varies with the rate at which it is deformed, the differential between accumulated strain and basaltic strength is sufficiently large to overcome even the most favorable of conditions, prohibiting crustal strengthening as the lone mechanism for strain accommodation throughout the region.

An additional hypothesis, the one most germane to the distribution of vents, asserts that strain is accommodated through the increase in volume associated with dike injection (Parsons et al., 1998; Rodgers et al., 2002). The presence of volcanic rift zones, a collection of aligned vents and fissures perpendicular to the horizontal least principal stress, is the main driver of this idea. These rift zones are inferred to be the surface expression of a network of dikes at depth. Wetmore et al. (2009) call into question the existence of such zones (with

the exception of the Great Rift) through the inclusion of buried eruptive centers in a re-examination of plain-wide vent distribution through spatial density analysis. Parsons et al. (1998) state that a cumulative dike width of ~6.8 m/1000 years is needed to extend the ESRP at the same rate as the Basin and Range. In order to attain this value, an eruption is required every ~140 years (assuming a dike width of 1 m); this rate of volcanism differs greatly from the published recurrence intervals of eruptions every 1,000 to 10,000 years (Kuntz et al., 1992; Kuntz, 1992). It is likely that a combination of dike injection, shearing, and strengthening of the lithosphere impact strain accommodation in the region, though it is not yet known to what extent each contributes. It is important to consider these uncertainties when choosing the appropriate approach to modeling the distribution of potential volcanic centers on the plain.

2.2 Geomorphology of the ESRP

The ESRP is a structural depression partially filled in by late Cenozoic volcanic material and sediment (McQuarrie and Rodgers, 1998). Bimodal volcanism (basalt-rhyolite) and sedimentation are the major depositional geomorphic processes of the ESRP (Figure 2.2).

2.2.1 Basaltic Volcanism

Approximatey 95% of the ESRP is paved over by basaltic lava (Kuntz et al., 1992) (Figure 2.4). The area inundated by a lava flow depends on the effusion rate, erupted volume, and rheological properties of the magma. These elements are a function of magma composition, temperature, and response to the topographic surface on which they flow (Dragoni and Tallarico, 1994; Griffiths, 2000; Costa and Macedonio, 2005). The majority of the basaltic lava flows on the surface of the ESRP are younger than 730 ka, with 13% of the region covered by flows late Pleistocene and Holocene in age ($<$15 ka)(Figure 2.2). The youngest of these flow fields, Wapi, erupted 2,270 ($\pm$50) years ago (Kuntz et al., 1986). Volumes of the latest Pleistocene/Holocene monogenetic eruptions range from $<$1 to 6 km^3. A more chemically
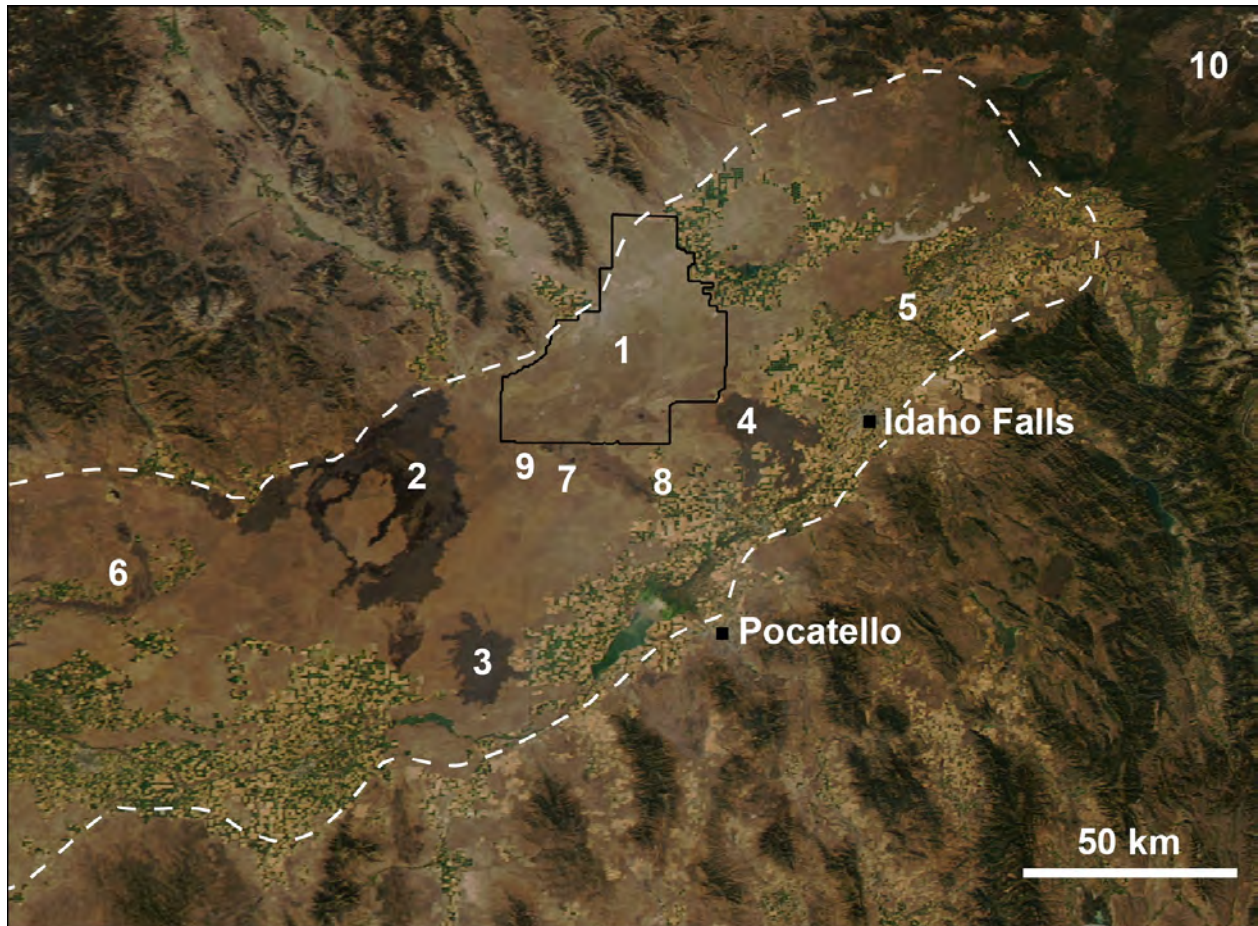
Figure 2.2: MODIS image of the ESRP, captured on August 29, 2008. Major features are numerically highlighted and substantial municipalities are labeled. 1 - Boundary outline for INL; 2 - Craters of the Moon (Active 15,000-2,076 YBP); 3 - Wapi/King's Bowl (2,222 YBP ±1 100); 4 - Hell's Half Acre (5,500YBP); 5 - Menan Buttes (~10,000 YBP); 6 - Shoshone Lava Flow (10,130 YBP ±1 350); 7 - North and South Robbers Lava Flows (11,940-11,980 YBP ±1300); 8 - Cerro Grande Lava Flow (13,380 YBP ±1 350); 9 - Big Southern Butte; 10 - Yellowstone.
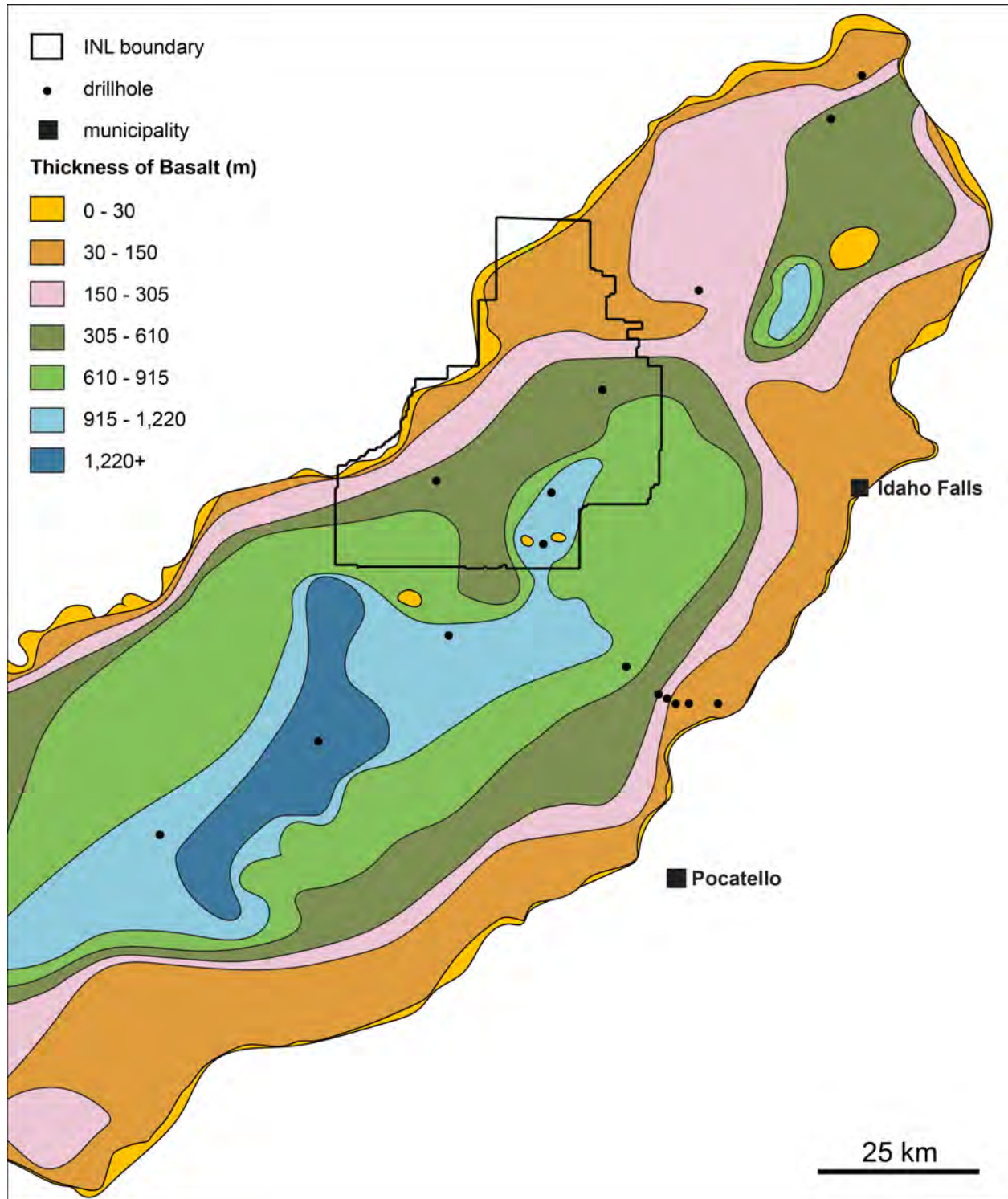
Figure 2.3: Sub-surface basalt thickness on the ESRP. Two additional NW-SE transects (not shown on map) were used to determine thicknesses. The thickening of the basalt stack in the center of the plain the mimics the surface expression of the axial volcanic zone. Sub-surface expressions of suggested volcanic rift zones are not apparent. Adapted from Idaho State University (2015).

evolved loci of eruptive activity, Craters of the Moon, contains some of the most prominent basaltic features on the ESRP, with tephra cones in the area reaching 250 m in height. Rare phreatomagmatic eruptions occur on the plain, most notably at Menan Buttes (Hackett and Morgan, 1988). Cumulative lava flow thickness ranges from 1 - 1.25 km throughout the ESRP, with the thickest stacks located centrally along the axial volcanic zone (Figure 2.3)(Kuntz et al., 1992). The repose interval between eruptions is approximately $10^3 - 10^4$ yr in duration, and, when coupled with the relatively small eruptive volumes of Holocene monogenetic fields, indicates episodic local melting, little or no accumulation of magma in reservoirs, and rise of magma to the surface fairly directly from the source depth (Kuntz et al., 1992; Wetmore et al., 2009).

Basalts of olivine tholeiite and alkaline basalt affinities dominate flow composition on the ESRP. Limited variation along textural, chemical, and mineralogical scales indicate they are resultant from partial melting of the lithospheric mantle at depths of 60 km (Leeman and Vitaliano, 1976; Stout and Nicholls, 1977; Leeman, 1982b). A small number of ESRP flows are more evolved hawaiite to trachyandesite, particularly at Craters of the Moon. Radiogenic isotopes (Sr, Nd, Pb, and Hf) suggest a derivation from basaltic parent material via some combination of fractional crystallisation and assimilation (Hildreth et al., 1991; Nash et al., 2006; McCurry and Rodgers, 2009).

Basaltic activity on the ESRP is a multi-stage process, similar to Hawai'i, and is described extensively by Kuntz et al. (1992). Hawaiian style stage-I volcanism (eg. North and South Robbers) is thought to be preceded by harmonic tremors, ground cracking, and gas/steam emissions. It is characterized by an annular flow regime that produces a curtain of fire hundreds of meters to several kilometers in length that can reach up to 500 m high and may persist from hours to days. These eruptions seem to be similar to the 2011 Kamoamoa eruption on Kīlauea (Orr et al., 2015). Sustained stage-I activity eventually transitions into Strombolian activity (stage-II). Eruptions of this type localize on discrete points along the fissure and form tephra cones. Towards the end of stage-II flows may emanate from

or below the cone, destroying the cone and rafting away segments on surface-fed pahōehōe flows. This stage may continue for several weeks. Hawaiian analogues include the 1950 and 1984 eruptions of Mauna Loa (Lockwood and Lipman, 1987). Stage-III (Hell's Half Acre) eruptions are long lived events that persist for months or years and effuse sufficient volume to produce a pronounced shield. Lava lakes are common and often exhibit cycles of filling and draining. The 1969-1974 Mauna Ulu eruption of Kīlauea is an excellent historical example of stage-III activity (Swanson et al., 1979). Stage-IV activity is not present on the ESRP and is expressed in Hawai'i as the entirety of Mauna Loa or Kīlauea, the sum of thousands to millions of years of centralized activity and are polygenetic.
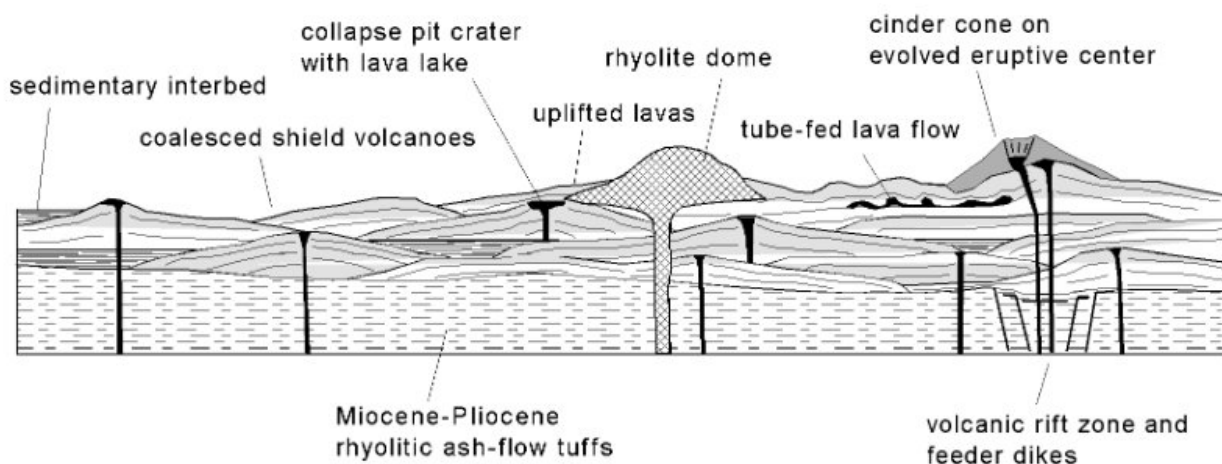
Figure 2.4: Scematic cross section of "plains-style" volcanism and the ESRP, from Hughes et al. (2002). This illustration shows the coalesced, overlapping shield volcanoes and the subdued relief common place on the ESRP. These overlie a thick layer of older ignimbrites (ash-flow tuffs). Sedimentary interbeds are also shown; alternating layers of rock and sediments attenuate seismic signals to a greater extent than uniform rock. Rhyolitic domes, such as Big Southern Butte, are shown centrally in the drawing. This illustration is not to scale and is assumed to be along axis with the length of the ESRP, as no thickening towards the center is shown.

2.2.2   Rhyolitic Volcanism

The hazard potential from rhyolitic eruptions is not assessed for this study, but understanding the presence of such material is fundamental to appreciating the geology processes that formed the ESRP. Large ignimbrite sheets pre-date basaltic material in most coreholes

(Lanphere et al., 1993; Anderson et al., 1996; Anderson and Liszewski, 1997). Basaltic volcanism associated with the passage of the hotspot follows the cessation of rhyolitic caldera activity by 2-3 My (Kuntz et al., 1992). Surficial rhyolites on the ESRP are mostly confined to a series of endogenous and crypto-domes (Kuntz et al., 1994). Big Southern Butte (300 ka), the most prominent structure on the ESRP, rises ~760 m above the plain and is composed of two coalesced domes (Spear and King, 1982). Several smaller domes dot the landscape to the east of Big Southern Butte. A small amount of ash associated with several YSHS eruptions is present, though the bulk of this material has has been paved over by younger lava flows or has been eroded away. A smaller complex of domes (~50 ky) reside to the SE of the plain near the Blackfoot reservoir. The magnitudes of these eruptions were VEI 2-3 (Welhan et al., 2014). Pyroclastic density currents and tephra fallout are the major hazards associated with these structures, but are not likely to greatly impact INL or the ESRP (Kuntz and Dalrymple, 1979; Volcanism Working Group, 1990; Hackett et al., 2002).

2.2.3 Sedimentary Processes and Hydrology

Surface cover from alluvial fans (Holocene to Pleistocene), lacustrine sediments (upper Pleistocene), eolian deposits (Holocene to upper Pleistocene), and colluvium (Holocene to Miocene(?)) is present within the boundaries of the ESRP (Kuntz et al., 1994). Continued subsidence, in conjunction with these deposits and younger lava flows, help to obscure older vents and hamper the ability to create a comprehensive list of all past eruptive centers (Wetmore, 1998). Anderson et al. (1996), Anderson and Liszewski (1997), and Wetmore (1998) took the first steps in rectifying this incomplete record in the INL region through the interpretation of well and corehole stratigraphy.

The subsidence of the ESRP has had a profound effect on fluvial drainage in the region; rivers flow towards the plain on the northwest and southeast margins and rotate towards the ESRP along the boundaries (McQuarrie and Rodgers, 1998). Rivers that extend onto the plain from the north are diverted by the topography of the axial volcanic zone and end up flowing into ephemeral lakes. The Snake River Plain aquifer underlies the entirety

of the SRP from Yellowstone to the shared border between Idaho and Oregon (Whitehead, 1994). This aquifer is crucial for the success of Idaho's agricultural industry and is at risk for further contamination should INL be inundated by lava flow(s).

2.2.4   INL Surface Geology

The surface of INL is covered by a combination of igneous and sedimentary strata (Figure 2.5). The majority (60.97%) is covered by basaltic flows ranging in age from 13.38 ka (Cerro Grande) to 4.5 Ma (unnamed Pliocene flows). The largest of these units is a 358 ka unnamed flow that covers 12.86% of INL's surface area. Other large flows include a 325 ka unnamed flow (11.78% coverage), a 268 ka unnamed flow (10.49% coverage), a 299 ka unnamed flow (10.07% coverage), and the 292 ka Crater Butte flow (9.47% coverage).

The majority of rhyolite deposits are ignimbrites, the bulk which originates from the Walcott, Blacktail Creek, Kyle Canyon, and Arbon Valley eruptive centers. These ignimbrites, along with East Butte and several lesser, unnamed buttes, account for only 0.32% of surface strata within INL boundaries.

Sedimentary units that include alluvial fans, colluvial aprons from endogenous rhyolite domes, eolian sands and dunes, lacustrine deposits, and flood sediments associated with jökulhlaups of the last glaciation (eg. Pinedale flood 19 ka) account for 38.70% of the surface strata.

2.3   INL Background

INL is a 2,310 km^2 Department of Energy managed nuclear research and development facility located on the northern edge of the ESRP. Previous monikers include INEL (Idaho National Engineering Laboratory) and INEEL (Idaho National Engineering and Environmental Laboratory). INL is Idaho's fifth largest employer, with a workforce of 3,900+ individuals (Idaho National Laboratory, 2016a).

The facility has housed 52 separate nuclear reactors since its inception in 1949. Significant events include: the first use of fission powered electricity by EBR-1 (Experimental
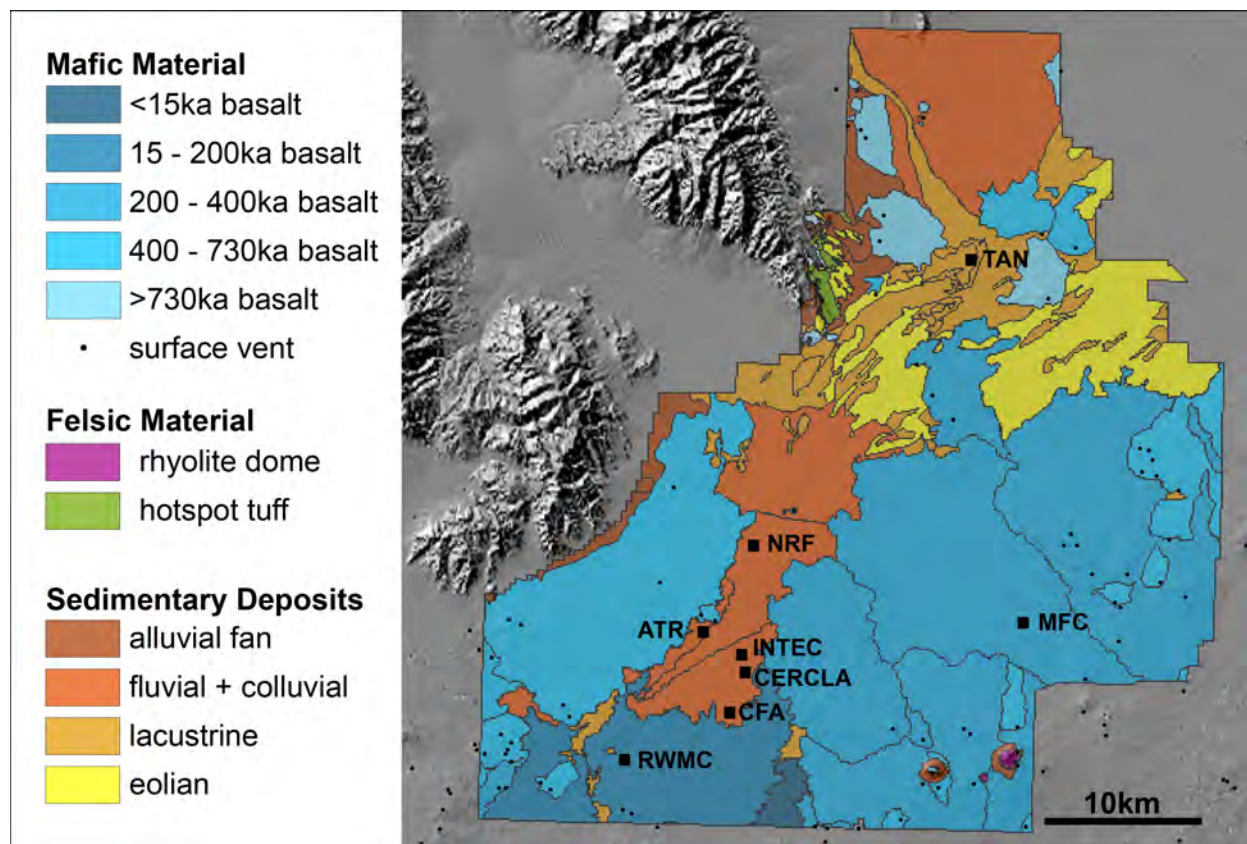
Figure 2.5: Surface geology of INL. The small black dots indicate locations of surface volcanic vents [I think I should add dots for the sub-surface vents, in a different colour].[TAN = Test Area North; MFC = Materials and Fuels Complex; RWMC = Radioactive Waste Management Complex; CFA = Central Facilities Area; CERCLA = Comprehensive Environmental Response, Compensation, and Liability Act Disposal Facility; INTEC = Idaho Nuclear Technology and Engineering Center; ATR = Advanced Test Reactor; NRF = Naval Reactors Facility.]

Breeder Reactor) in 1951; the building of a reactor prototype for the first nuclear submarine, Nautilus, in 1953; and the first illumination of a municipality by nuclear energy (Arco, ID) from BORAX-III in 1955. Current infrastructure includes the Advanced Test Reactor Complex (ATRC), Materials and Fuels Complex (MFC), Test Area North (TAN), Critical Infrastructure Test Range Complex (CITRC), and the Radioactive Waste Management Complex (RWMC) (Figure 2.5). An off-site facility in Idaho Falls, ID, houses the Center for Advanced Energy Studies (CAES), Matched Index of Refraction facility (MIR), and a Geocentrifuge (Idaho National Laboratory, 2016b).

2.4   Hazard Assessment and Mitigation Strategies

Hazard assessments are often utilized to create informed disaster management plans and site-specific designs for areas of potential impact (Connor et al., 2009). Volcanic hazard assessments originally focused *solely* on past eruptive events as indicators of future activity; while this approach is still widely employed today, many researchers are now incorporating a region's history into computational models as predictors of future behavior (Newhall and Hoblitt, 2002; Marzocchi et al., 2004, 2008, 2010; Aspinall et al., 2006; Marzocchi and Zaccarelli, 2006; Marti et al., 2008; Sobradelo and Marti, 2010; Sobradelo et al., 2011). Statistical treatment of data has powerful implications for creating a comprehensive catalog of possible scenarios because it allows researchers to extrapolate for events that may not be present in the current geologic record due to burial or poor preservation (Wetmore et al., 2009).

Mitigation strategies for lava flow hazards pre-date their hazard assessments. Flow diversion was first recorded in 1669, when the city of Catania was saved at the expense of Paterno (Crisci et al., 2003). In-situ diversion structures were created to combat the progress of the 1973 Eldfell flow (Iceland) by pumping sea water onto the advancing flow front (Williams and Moore, 1983). Although the efforts in Iceland are often cited as one of the most successful attempts to control the path of lava, the ability to save Heimay harbor was more dependent on the eruption duration and magma supply than on human

16

intervention. The same approach was unsuccessful at saving Hawaiʻi Volcanoes National Park's Wahaʻula Visitor Center in 1989 due to a more persistent effusion rate and eruption duration (Hawaiian Volcano Observatory, 2007). Bombing of lava flows in order to breach levees and divert flow out of the active channel was unsuccessfully attempted on the 1935 and 1942 Mauna Loa eruptions (Lockwood and Torgerson, 1980). However, this same method was successfully employed on Mt Etna in the 1980's and 1990's to save the city of Zafferana (Tanner and Calvari, 2012). These scenarios illustrate the uncertain nature of lava flow inundation mitigation and highlight the need for comprehensive lava flow hazard assessment and careful site planning.

2.4.1 Volcanic Hazard Assessment for Nuclear Facilities

Volentik et al. (2009) examined the various volcanic hazards present for the Bataan Nuclear Facility in the Philippines and highlighted the need for a comprehensive geologic assessment prior to the beginning of a hazard assessment plan. Valentine and Perry (2009) assessed volcanic hazards and their associated risks at Yucca Mountain, Nevada. Their approach identified possible eruption scenarios, estimated the probability of these events, and obtained the constraints on potential consequences of such events on the proposed nuclear waste storage facility.

Connor et al. (2012) examined the inundation probability for the Armenian Nuclear power plant. They employed a two-stage process using a two-dimensional elliptical Gaussian kernel function to estimate the spatial density of previous eruptive vents. Eruptions emanating from vents, sampled from the spatial density model, were executed using a lava flow inundation model. This method resolved the conditional probability of lava flow inundation, given the opening of a new vent on the Shamiram Plateau. A map of vent locations that produced flows inundating the area of interest (AOI) was also presented. The work of this thesis follows a similar process with several modifications.

2.4.2 Previous INL Natural Hazard Assessments

Previous hazard assessments for INL have been conducted by Kuntz (1978); Kuntz and Dalrymple (1979); Volcanism Working Group (1990); Hackett and Smith (1994); Hackett et al. (2002). This collection focuses on a multitude of potential hazards, including; volcanic phenomena, gas emission, seismic activity, and ground deformation. Much of these early efforts, specifically those of Kuntz (1978) and Kuntz and Dalrymple (1979), take an approach of cataloging the nature and extent of potential hazards similar to Volentik et al. (2009). Hackett et al. (2002), a revision of Hackett and Smith (1994), is the most comprehensive and thorough of these studies. Appendix B contains tables from Hackett et al. (2002) that combine information assembled from several of these previous assessments and a list of volcanic phenomena of the ESRP.

Hackett et al. (2002) report the probability of lava flow inundation of INL as a range from 6 x 10^{-5}/yr (16-17 ka between eruptions) along the southern border to 1 x 10^{-5}/yr (100 ka between eruptions) along the Howe-East Butte volcanic rift zone. Detailed analysis of lava flow lengths provided the basis for assignment of inundation hazard, where distances <10 km from a vent <400 ka constituted the zone of highest hazard (Figure 2.6). This approach was based on previous assessments for the Island of Hawai'i (Mullineaux et al., 1987; Wright et al., 1992). The substantial slope differences between Hawaiian Volcanoes and the ESRP have important implications for the flow heights, distances, and potential for channelization (Rowland et al., 2005); Mauna Loa has an average slope of 16° and Kīlauea an average of 8° (Bleacher and Greeley, 2003), while slopes on the ESRP average <5° (Weren et al., 2004). For this reason, the inclusion of volumes in a hazard assessment for the ESRP is paramount in determining the area of inundation accurately.

Wetmore et al. (2009) utilized the spatial density estimation technique of Connor and Connor (2009) to examine the distribution of eruptive vents for INL. Vents from both the surface and sub-surface were utilized in the study (Anderson et al., 1996; Wetmore, 1998). The inclusion of buried vents drastically altered the spatial density estimation and high-

lighted the need for comprehensive stratigraphies to improve hazard modeling. This thesis completes the lava flow inundation hazard assessment with these vent data by simulating a multitude possible flow scenarios using a cellular automata code. It employs a new method to examine the vent distribution by clustering vents into eruptive events, described further in section 3.1.
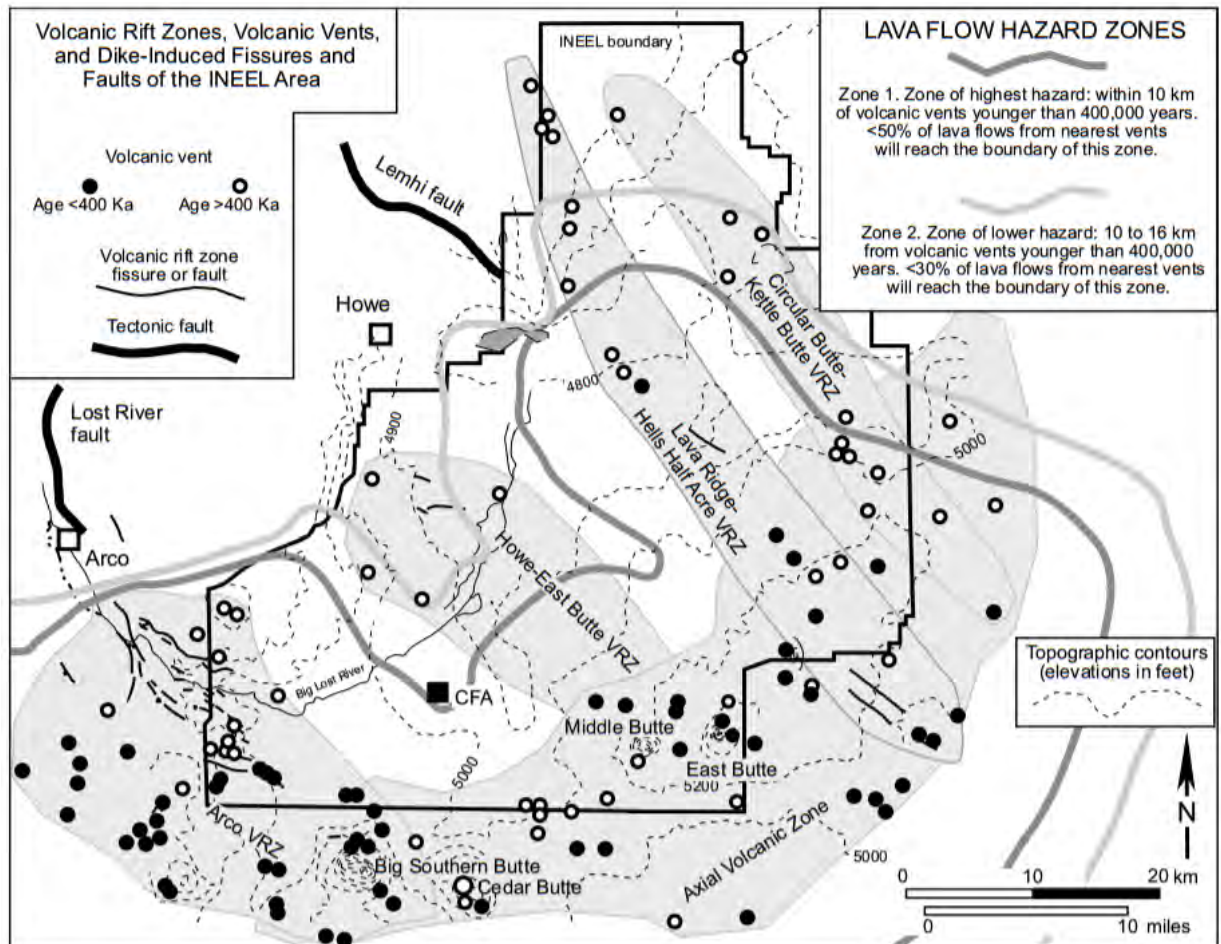
Figure 2.6: Lava flow hazard zones from Hackett and Smith (2002). This map follows the current Hawaiian model of assigning zones of hazard by likelihood of lava flow inundation based on proximity to the most recent eruptions.

3. Methods

The process utilized for this thesis incorporates vent ages and locations, lava flow thicknesses, erupted volumes, and an accurate topographic model to calculate inundation probabilities for locations on the ESRP (Figure 3.1). The conditional probabilities of new eruptive centers on the ESRP were modeled using the SAMSE method, a smoothed asymptotic mean squared error approach, to optimally determine smoothing bandwiths for bivariate Gaussian kernel functions (Duong and Hazelton, 2003). These kernel density estimates were used to model possible eruption sources through stochastic sampling. Monte Carlo simulations were run using these sampled source lists as inputs for MOLASSES (**MO**dular **LA**va **S**imulation **S**oftware for **E**arth **S**cience), described in section 3.5, as well as modeled data sets of eruptive volumes and modal lava flow thicknesses, also stochastically sampled from geologic data. These modeled flows were then effused onto a digital elevation model (DEM). The results of this process are reported as probabilistic inundation maps, estimates of the likelihood of lava flow inundation given the assumption of a future eruption.

3.1 Defining Eruption Models

Volcanic eruptions are extremely complicated multi-phase processes and are therefore difficult to model. Although the definition of an eruption is fairly straightforward, the explosive ejection of fragmented new magma or older solidified material and/or the effusion of liquid lava (Siebert et al., 2015), further examination raises some questions about what process is being captured by this definition and its associated timeline. Does continuous activity, such as the 1983-ongoing eruption of Pu'u Ō'ō, count as many individual eruptions or as a single eruption? Can a single eruption occur simultaneously from two spatially close but separate vents, such as the 2012-2013 Tobalchik flows, or does this concurrent activity

20
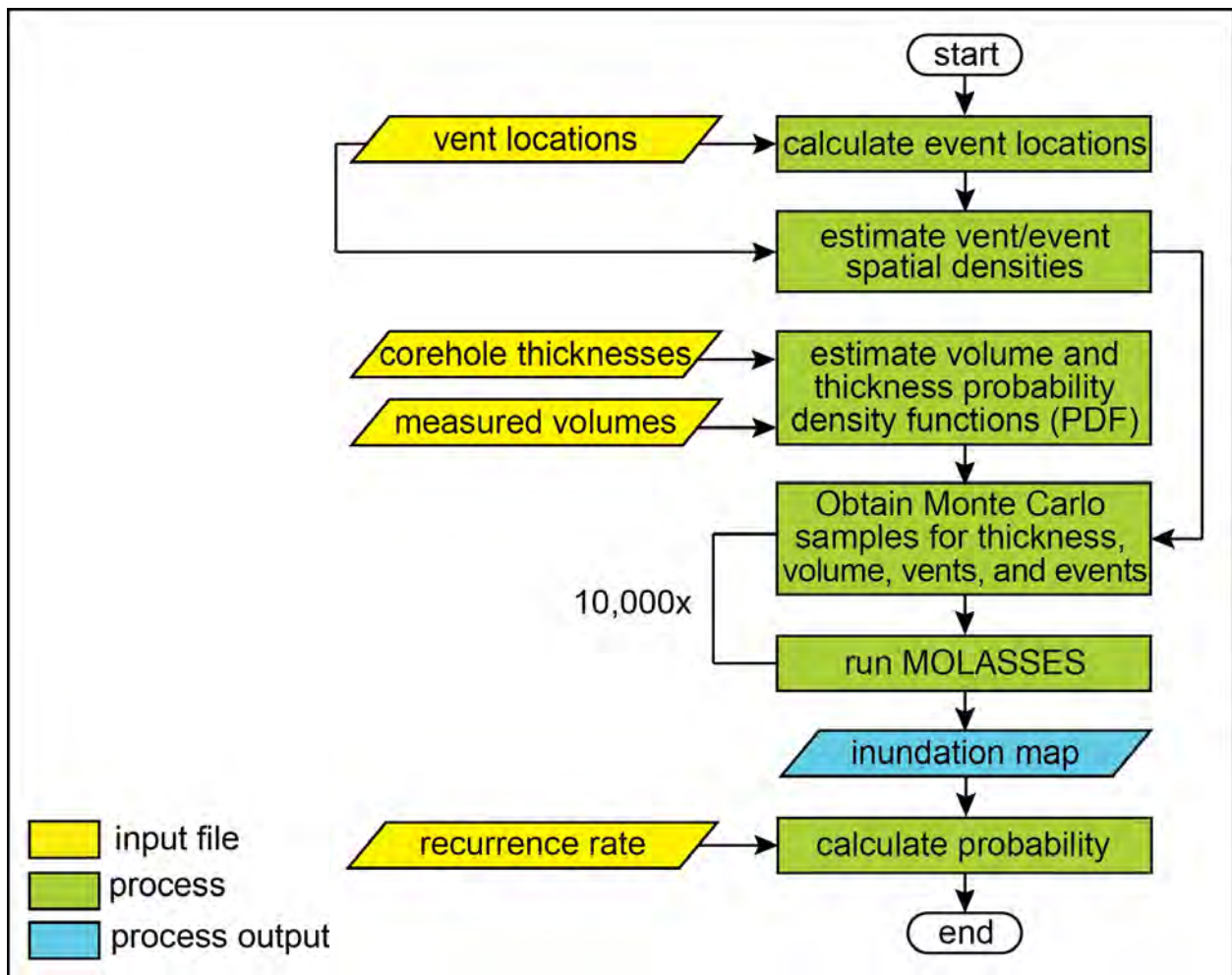
Figure 3.1: High-level workflow for assessing inundation probability. This process is a modification of the method established by Connor et al. (2012).

count as two eruptions? These questions explore whether the definition is conceptually capturing deep or superficial processes associated with eruptions. This thesis defines what types of spatial and temporal restrictions should be assigned to the definition of an eruption as it relates to activity on the ESRP.

For the purpose of this study, the term 'vent' is assigned to a single point where a single eruption occurred. The term 'event' is assigned to a point that is independent of all other points. An event may represent an eruption with a single vent or a group of vents that formed during the same time period and are dependent on the same network of dikes and sills. The event is an eruption model used to capture deeper magma ascent processes, while the vent model explores surficial eruption processes. The difference between these two definitions is illustrated using eruptive structures within the Robbers Volcanic Field on the ESRP (Figure 3.2).

Elucidating a list of Events from Vents

The list of ESRP surface vents and associated ages was compiled from the publications and maps of Lanphere et al. (1993); Kuntz et al. (1994); Anderson and Liszewski (1997); Kuntz et al. (2007). These data sets were incorporated into Matlab programs to cluster vents into two separate lists of eruptive events, one for vents with reported ages and another for vents without reported ages (Figure 3.2). A recent study of the Harrat Rahat in Saudi Arabia has also explored the relationship between vents and events and establishes event parameters, but did so through use of expert elicitation (Runge et al., 2014). A data driven approach is preferred for this work in order to better define spatial and temporal constraints as they specifically relate to the ESRP.

Step 1: Separation by Age

Vents were separated into two categories, those with a reported age and those without. A total of 506 surface vents were identified; 355 vents had an assigned age, and 151 did not. Table 1 of Appendix C contains this list.
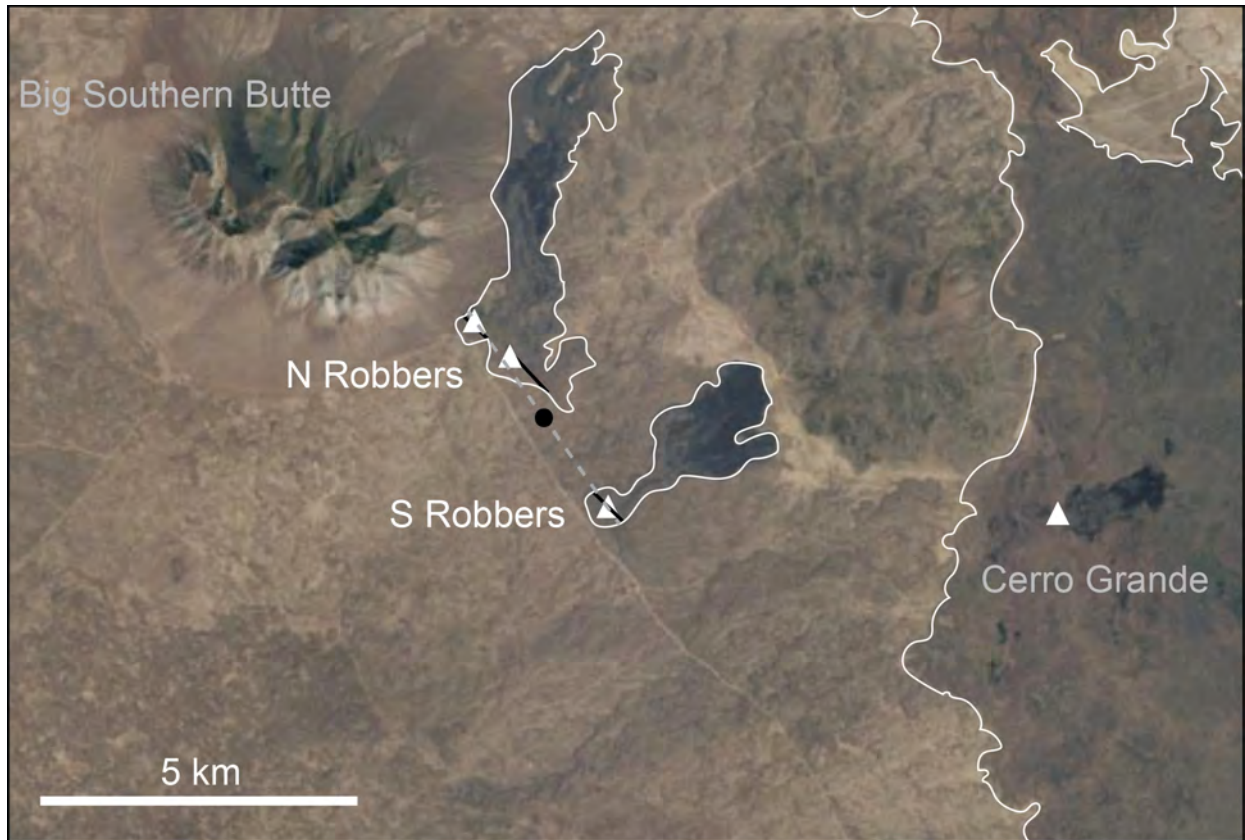
Figure 3.2: An example on the ESRP of vents vs. events. North and South Robbers are two small Hawaiian style flow fields that erupted concurrently 11,940-11,989 ya ($\pm$ 300). The white triangles represent vents in the region, with 3 separate vents assigned to the Robbers Volcanic Field. The black lines are mapped fissures. The black dot at the center of the two flows illustrates the theorized event location. The dashed grey line is the orientation of an assumed dike that fed the the 3 simultaneously erupting vents.
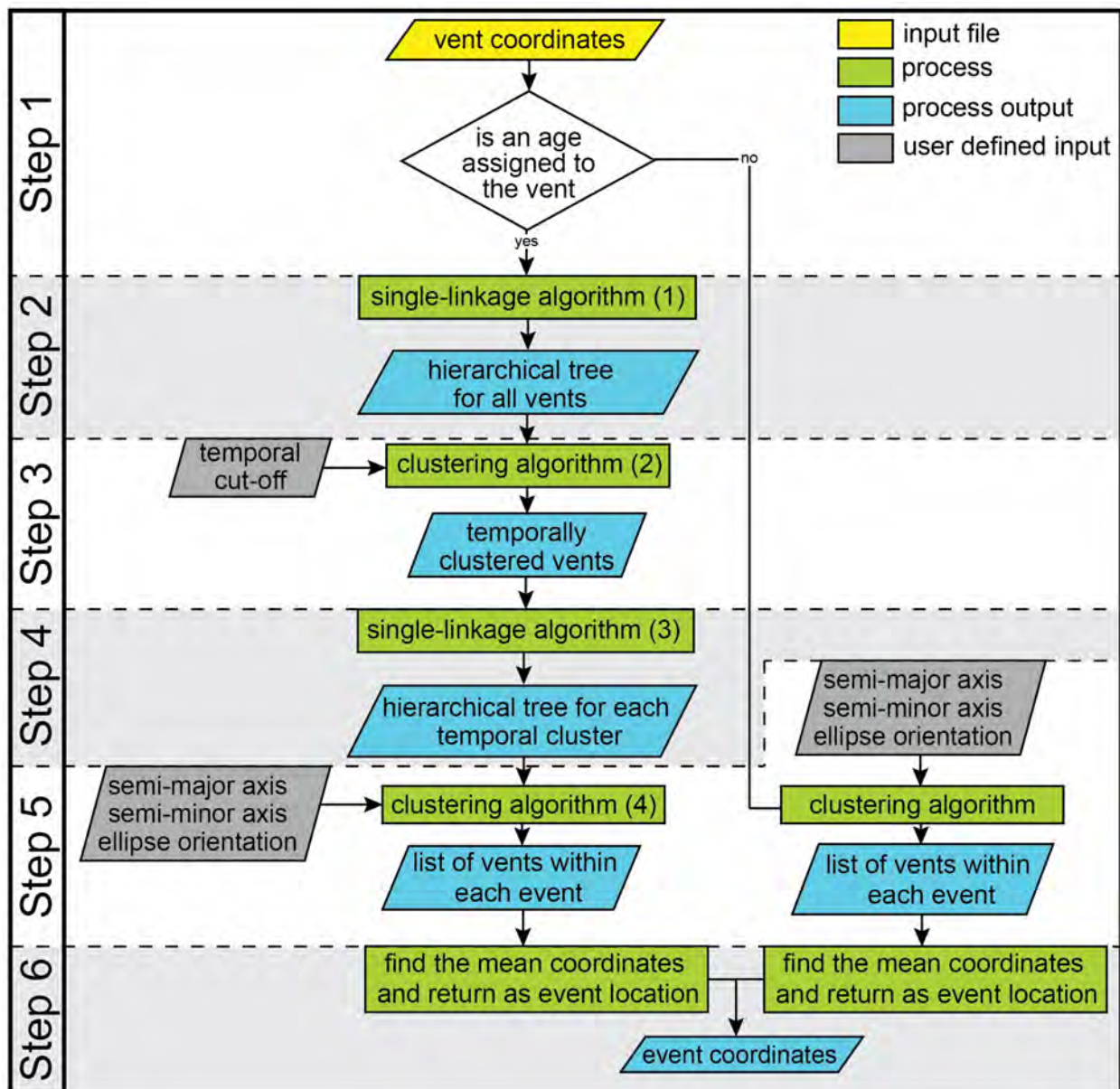
Figure 3.3: Workflow of vents to events process. This flowchart shows a six step process for defining a list of eruptive events from a list of surface vents on the ESRP.

Step 2: Temporal Linkage

The relationship between vents with reported ages was defined by an agglomerative single-linkage algorithm (algorithm 1). The temporal relationships between the linked vents were then organized into a minimal spanning tree, also referred to as a dendrogram (Figure 3.4).

Algorithm 1 - Temporal Agglomerative Single-linkage Algorithm

begin initialise $c, \hat{c} \leftarrow n$, $T_i \leftarrow$ **x**i, $i = 1,...,n$
        do $\hat{c} \leftarrow \hat{c}$-1
                find nearest clusters, T_a and T_b
                merge T_a and T_b
           until $c = \hat{c}$
      return c clusters
end

where; c = desired number of final clusters (1 in our case), T_i = start time, T_a = vent whose age is closest to T_i, and T_b = vent whose age is closest to T_a

The dendrogram was formed by iteratively linking the two temporally closest data as a single cluster, whose age is the mean of estimated ages of included vents. This process continued until all vents were classified as a single event. The resultant dendrogram was then used as the basis of a clustering algorithm (step 3).

Step 3: Clustering Temporal Events

Vents were clustered together in a divisive (bottom up) manner from the dendrogram created in step 2 (algorithm 2).
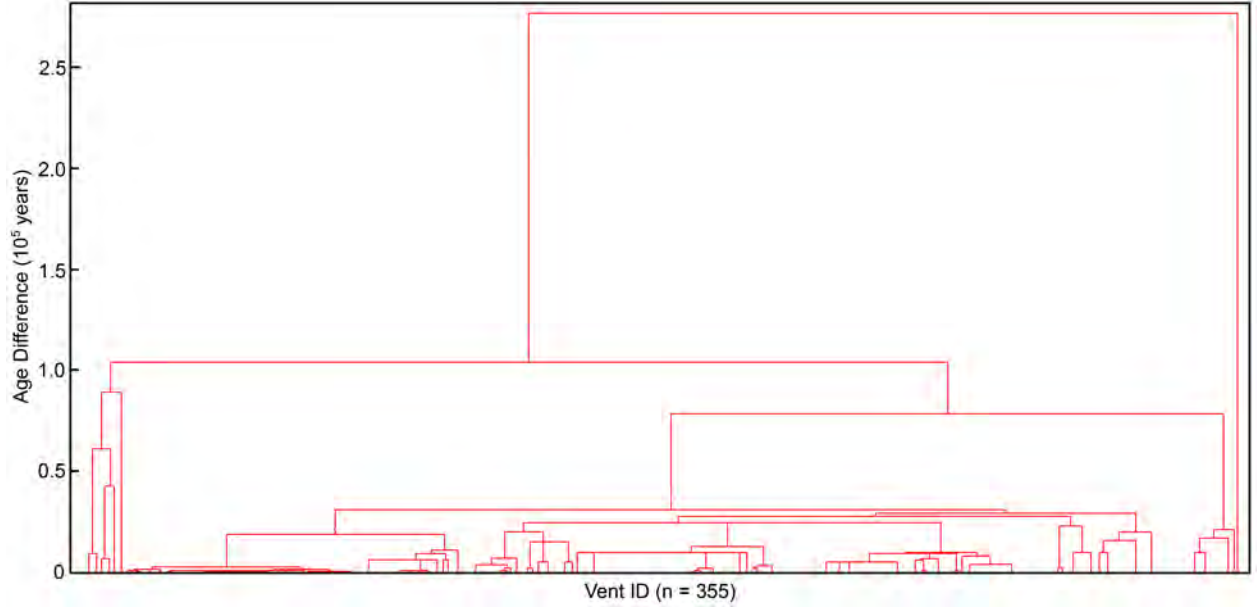
Figure 3.4: Dendrogram of temporally clustered vents. The algorithm from which this dendrogram was created links pairs of vents that are close together in age into binary clusters. It then links these newly formed clusters to each other and to other vents to create larger clusters until all vents are linked together in the hierarchical tree above.

Algorithm 2 - Temporal Divisive Clustering Algorithm

begin initialise k = 1.1, n ← 0

        do n ← n + 1

            C = [c1, c2, ..., cn]

            find μ, σ for each cluster in C

        if any $|x - \mu| > k\sigma$

            continue

        else

    return C, μ

end

where; σ = standard deviation, μ = average age of the cluster, k = standard deviation

The clustering algorithm first assigned all vents to a single cluster, the top of the dendrogram constructed in Step 2. The mean and standard deviation of the ages in each group was then calculated. If any age within the group resided outside of the specified standard deviation from the mean, the function stepped down a level in the dendrogram and repeated this process until all vents in a group were within the specified standard deviation range. A

standard deviation cut-off of 1.1 was selected based on the distribution of vents against age (figure 3.5).
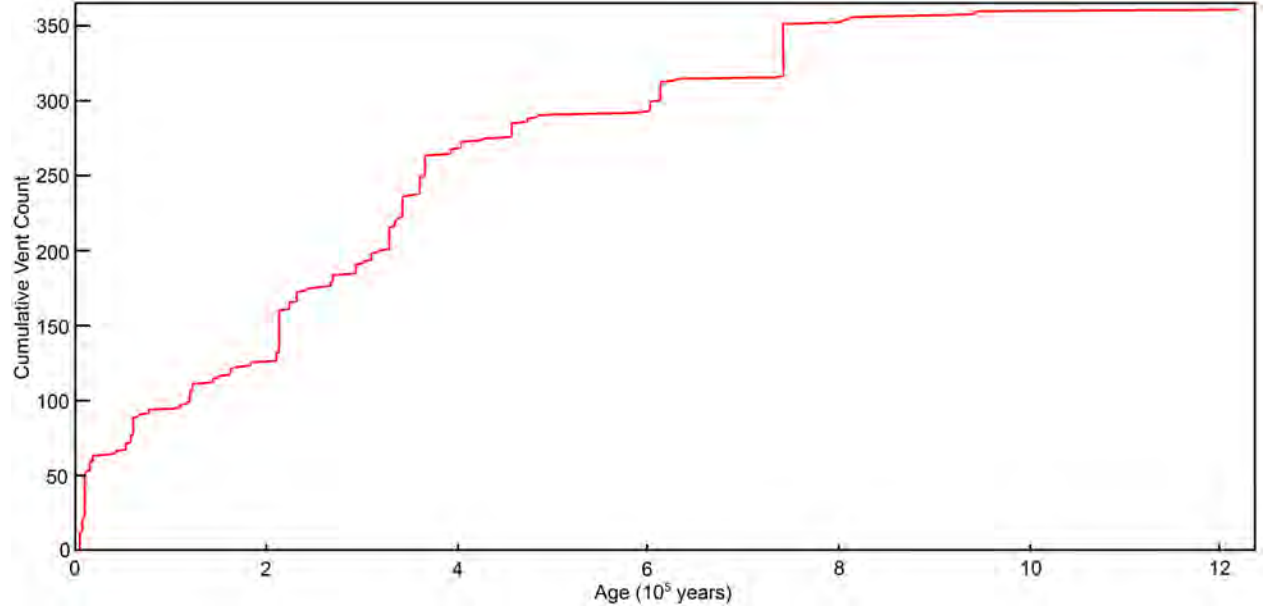
Figure 3.5: Plot of the cumulative number of vents vs. their reported age.

Step 4: Spatially Linking Temporally Clustered Vents

The spatial relationships between vents within a single age cluster were defined by an agglomerative single-linkage algorithm (algorithm 3). These relationships were then organized into a dendrogram.

Algorithm 3 - Spatial Agglomerative Single-linkage Algorithm

begin initialise $c, \hat{c} \leftarrow n$, $Di \leftarrow \mathbf{x}i$, $i = 1,...,n$
         do $\hat{c} \leftarrow \hat{c}$-1
                find nearest clusters, D_a and D_b
                merge D_a and D_b
         until $c = \hat{c}$
     return c clusters
end

where; c = desired number of final clusters and D = distance

Step 5: Spatially Clustering Spatially Linked Vents

A hierarchical clustering algorithm (algorithm 4) was applied to each spatial tree constructed in Step 4.

Algorithm 4 - Spatial Divisive Clustering Algorithm

begin initialise ellipse, n ← 0

        do n ← n + 1

                C = [c1, c2, ..., cn]

                find μN, μE for each cluster in C

                orient ellipse center on μN, μE

        if any vent lies outside of the ellipse template

                continue

        else

      return C, μN, μE

end

where; μN = average Northing of vents in cluster, μE = average Easting of vents in cluster,

Initially all vents in each temporal cluster were assumed to comprise a single spatial cluster. The mean position for the spatial cluster was calculated and included all vents within the age group. A user defined elliptical template was then centered at the mean. This template was defined by the lengths of the semi-major and semi-minor axes, and the angle between the semi-major and north axes. For these data the average alignment of known tectonic structures on the ESRP was used as the orientation of the ellipse (Kuntz, 1992). Values of 10 km for the semi-major axis and 5 km for the semi-minor axis were used based on descriptions from Kuntz et al. (1992). If vents were located outside the elliptical template a new cluster was defined by stepping down a level in the dendrogram from step 4. This was repeated until all vents resided within a template (Figure 3.6). This algorithm was also used to spatially cluster vents with no ages.

Step 6: Creating an Event List

The locations for all vents in each spatial cluster were averaged together to represent the location of the eruptive event. A list of all eruptive events was then utilized to create an event spatial density map.
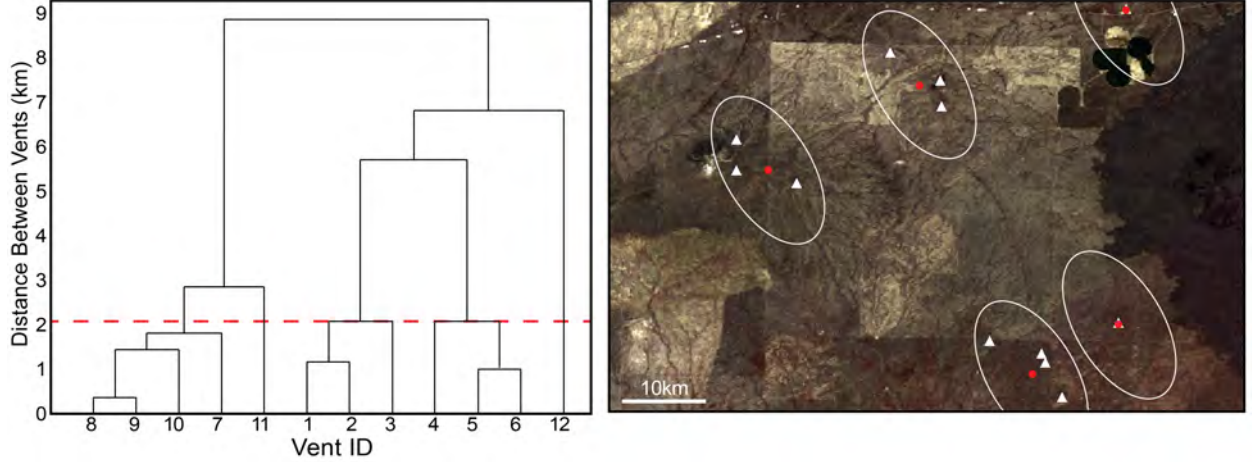
Figure 3.6: Example of the process and outcome for spatially clustering vents. The dendrogram on the left is for the 358 ka age group. The red dashed line illustrates the point in the dendrogram at which all conditions were satisfied (all vents were within an ellipse). The map to the right illustrates the usage of the elliptical template for spatial linkage. The red dots within the center of each ellipse indicate the location returned for the representitive event.

3.2 Spatial Density Estimation

The variation of vent locations within a distributed volcanic field creates a unique problem for appropriately modeling monogenetic volcanism; given the assumption that an eruption will occur in the future, how can the coordinates of a future eruptive vent be determined? Identifying the location of an eruptive center has important implications for lava flow hazard assessment, as a slight variation may have a substantial impact on the path of a flow (Connor et al., 2012). The position of many INL facilities within the Big Lost River Trough leaves them vulnerable to inundation given even slight changes in vent locale. Volcanic fields are usually distributed in an elliptical pattern whose major axis is parallel to the direction of least principal stress (σ_3), though this is not the case for the ESRP. While

volcanism on the ESRP is distributed in an elliptical pattern, its major axis follows the transit of the North American plate over the YSHS, perpendicular to σ_3.

Kernel density estimation is a statistical method that defines spatial intensity (the number of events per unit area). It is a useful method for identifying tectonic control on the distribution of vents and events, as expressed through point clustering within a given region. The spatial intensities of vents and events for the ESRP were estimated using a nonparametric kernel density function (Connor and Hill, 1995; Connor and Connor, 2009; Kiyosugi et al., 2010; Bebbington and Cronin, 2011; Connor et al., 2012). These analyses were based on a bivariate Gaussian kernel function (equation 3.1) and a directional smoothing bandwidth (equation 3.2)(Wand and Jones, 1995).

$$\hat{\lambda}(s) = \frac{1}{2\pi |H|} \sum_{i=1}^{N} exp[-\frac{1}{2}\mathbf{b}^T\mathbf{b}] \tag{3.1}$$

where;

$$\mathbf{b} = H^{-\frac{1}{2}}\mathbf{x} \tag{3.2}$$

The spatial density estimate at a given point, $\hat{\lambda}$, is dependent on the total number of vents or events, N and the distance to each event location from the point of the spatial density estimate. H, a 2 x 2 matrix, is the bandwidth that establishes smoothing in the N-S and E-W directions. $|H|$ is the determinant of the matrix, while $H^{-1/2}$ is the inverse of its square root. $\mathbf{x}$ is a 1 x 2 distance matrix, the x and y distances from (s) to a vent or event. $\mathbf{b}$ is the cross product of $\mathbf{x}$ and H. $\mathbf{b}^T$ is its transform.

The utilization of a bandwidth accounted for the unique orientation of vent and event distribution ellipses. The specific bandwidths chosen represented optimal smoothing, based on the SAMSE (smoothed asymptotic mean integrated squared error) method for multivariate kernel smoothing, and were calculated from the locations of all known vents and estimated eruptive events. The bandwith controls how local intensity diffuses with distance

from the central point. This optimal bandwidth selection method objectively determines the smoothing applied to the Gaussian kernel (Duong and Hazelton, 2003; Duong, 2007; Chacón and Duong, 2011, 2013; Chacón et al., 2011). Bandwidth selectors, such as SAMSE, impart objectivity to the process. A disadvantage of bandwidth selections is that they do not account for the control of geologic structures on volcanism.

3.3 Lava Flow Thicknesses

Lava flow thicknesses were obtained from corehole data reported in the suplementary material of Anderson et al. (1996). Values with uncertainty (noted in the dataset with a $<$ or $>$ symbol) were removed. These data accounted for 256 values out of 4,226. Another 1,575 entries represented sedimentary or rhyolitic layers and were also discarded, leaving 2,395 thickness values. One-sided distributions were fit to the data to determine the best-fit-solution (Figure 3.7). A set of 10,000 experimental thicknesses were drawn from a maximum likelihood fit of a log-normal distribution to the available thickness data. These 10,000 values were used as inputs for both the vent and event lava flow simulations.
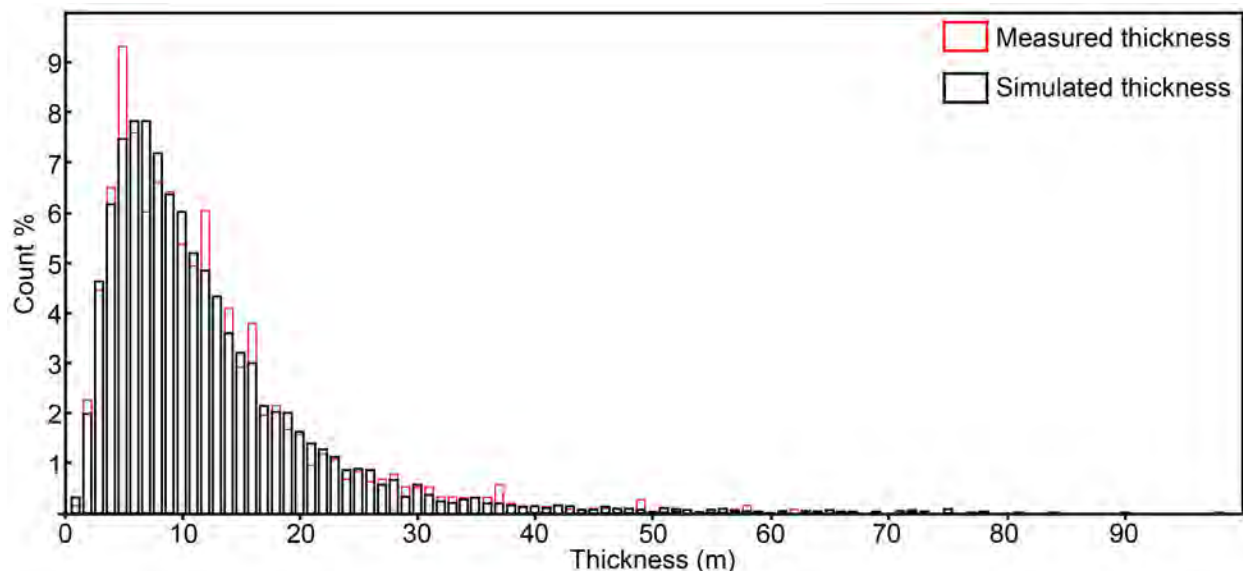
Figure 3.7: Histogram of actual vs. modeled thickness data. The red bars indicate measured values, while the black bars indicate modeled values. The mean thickness of the measured values is 11.8 m, with a standard deviation of 8.8 m. The mean thickness of modeled values is 12.1 m, with a standard deviation of 6.2 m.

3.4 Lava Flow Volumes

Lava flow volumes were reported in the literature of Kuntz (1992); Kuntz et al. (1994). Measurable lava flows whose volumes were not published were obtained by digitizing regional maps in Quantum GIS and multiplying flow areas by the average observed thicknesses (11.8 m)(Table 3.1) (Kuntz et al., 1994, 2007). A lava flow was deemed 'measurable' if its entire surface overlays the surrounding topography (eg. Quaking Aspen and Taber Butte). Flows whose surfaces were obstructed by younger units or sedimentary deposits did not preserve the appropriate aerial extent, and were therefore excluded. A set of 10,000 experimental volumes were drawn from a maximum likelihood fit of a log-normal distribution to the available volume data (Figure 3.8). These 10,000 values were used as inputs for both the vent and event lava flow simulations. Given that the first pulse of activity is usually the most voluminous in an eruption, it is reasonable to model both vent and event flows using the same volume dataset.
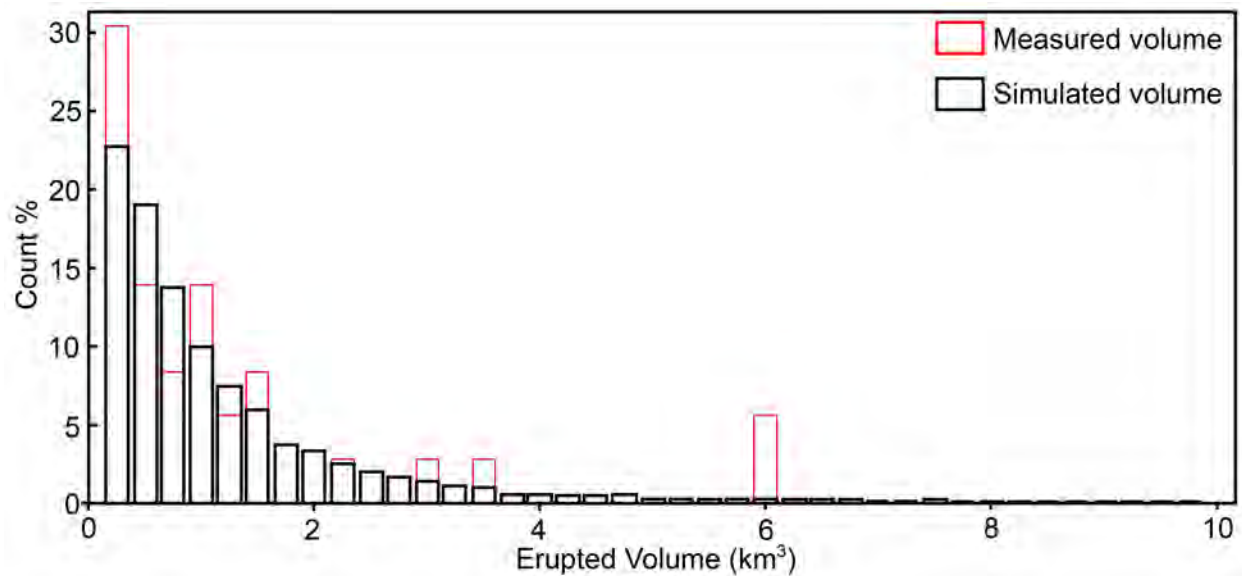
Figure 3.8: Histogram of actual vs. modeled volume data. The red bars indicate measured values, while the black bars indicate modeled values.The mean volume of the measured values is $1.44\,km^3$, with a standard deviation of $1.98\,km^3$. The mean volume of modeled values is $1.21km^3$, with a standard deviation of $1.27\,km^3$.

Table 3.1: ESRP Lava Flows

Name	Volume (km^3)	Length (km)	Area (km^2)
Shoshone	1.500	60.00	190
Broken Top	0.100	3.15	11
Blue Dragon	3.400	22.05	280
Trench Mortar Flat	0.030	6.76	6
North Crater	0.010	1.80	1.5
Big Craters	0.050	2.97	9
Serate/Devil's Orchard	0.500	4.95	27
Vermillion Chasm	0.100	6.98	20
Deadhorse	0.040	4.50	8
Devil's Cauldron	0.900	11.70	90
Minidoka	3.000	23.40	250
Quaking Aspen*	1.970	6.75	179
Wapi	6.000	19.32	325
King's Bowl	0.005	1.07	3
N Robbers	0.050	8.59	5
S Robbers	0.030	5.37	3
Cerro Grande	2.300	18.25	175
Taber Butte*	1.380	17.17	125
Hell's Half Acre	6.000	10.00	400

indicate values obtained through geospatial analysis

3.5 MOLASSES - Lava Flow Simulation

A variety of computational lava flow simulators exist to model different aspects of effusive eruptions. Cellula Automata (CA) lava flow models are volume limited and distribute lava from cell to cell based on a set of rules associated with the elevation of individual cells, thickness within the cell, and possibly temperature (Barca et al., 1993; Connor et al., 2012; Rongo et al., 2015). Three-dimensional computational fluid dynamic models attempt to quantify the highly complex relationships between convection, solidification, temperature dependent magma viscosity, and spreading geometries (Fujita and Nagai, 2015).

Two-dimensional depth-averaged equation models are based on shallow water equations that explore the relationship between fluid depth, terrain surface, depth-averaged fluid velocity components, and the friction coefficient between the flow and terrain (Harris and Rowland, 2001; Costa and Macedonio, 2005). The selection of the appropriate model is dependent upon the reason for which the lava flow is being simulated.

A CA model was chosen for this work due to the quick speeds needed for the large number of runs required. This work is the first lava flow hazard assessment for INL to use a deterministic computational CA lava flow model to assess inundation probability via Monte Carlo simulations. MOLASSES, written in C, is the CA code that was selected for this task and is based on the LavaPL algorithm of Connor et al. (2012). MOLASSES perfomed successfully in a multitude of benchmarking exercises (Richardson, 2016) and was rigorously tested against the 2012-2013 Tobalchik, Kamchatka fissure eruption (Kubanek et al., 2015). Required inputs were accessible with relative ease and included flow thickness, flow volume, vent locations, and a digital elevation model (DEM) of the region. Monte Carlo simulations generated many possible lava flows from which the conditional probabilities of site inundation of areas of interest were estimated, given the opening of a new vent on the ESRP.

MOLASSES works by distributing lava between cells based on specific rules that govern flow behaviour assigned to every cell within a gridded array (see Appendix D for a schematic of the workflow and for more information on cell behaviors). A user-altered configuration file provides the vent location, modal flow thickness, total erupted volume, and pulse volume. An eruption is initiated within the grid, activating the cell. The cells adjacent to the vent are activated. Lava is then pulsed from from this parent cell into these adjacent cells based on the behavior rules, also established by the user. This process is repeated until the total volume has been exhausted. Once finished, a file is output (TIF or ASCII) that 'maps' out the area inundated.

20,000 flows were simulated onto a 90 m DEM (National Elevation Dataset - SRTM) using an eight cell parent-less neighbor sharing relationship with slope-proportional spreading; 10,000 sourced from the vent list and 10,000 from the event list. The entire area of flows that inundated INL were added together as the code iterated over the 10,000 runs. The number of times each individual cell had been hit was tallied at the end of this process. These vent and event intensity maps, along with the source locations that produced inundating flows, were used to identify areas at greatest risk.

3.6 Recurrence Interval

The probability of lava flow inundation of INL and cities on the ESRP is intrinsically linked to the recurrence interval (RI) of volcanism in the region. This calculation is an estimate of the average amount of time between eruptions and does not reflect temporal changes in activity (equation 3.3):

$$\lambda = \frac{N - 1}{T_0 - T_M} \tag{3.3}$$

where N is the total number of eruptions, T_0 is the age of the oldest datum, and T_M is the age of the youngest datum.

The RI is the greatest contributor of uncertainty in assigning inundation probability because the calculation relies heavily on the completeness of the eruption catalog and the accuracy of dating techniques. A variety of approaches may be considered when selecting the appropriate dataset for RI calculation. Should an abbreviated segment of the vent catalog be selected to represent trends in future activity on the ESRP? Examination of the ages of surface vents over time (Figure 3.5) provides insight to the temporal changes in activity. Eruption frequency appears to drop off after ~450 My, though this is likely due to the burial of vents and flow units. Based on the potential for error due to burial, should inputs instead focus on a vertical section from a corehole? This calls into question whether or

not a discrete point is representative of a plain wide trend in volcanism. It quickly becomes apparent why these assumptions introduce uncertainty to the process and that no approach is comprehensive. RI calculations for the vent and event catalogs and for corehole data were compared in order to explore these uncertainties and to determine which was most appropriate for calculating annual probabilities of lava flow inundation.

4. Results

4.1 Eruption Models

The original surface vent list (Anderson et al., 1996; Wetmore, 1998), consisting of 506 entries (355 with relative or absolute ages, 151 without), was distilled into an inventory of 256 events (159 with relative or absolute age averages, 97 without) (Figure 4.1). Each dated event represents an average of 1.97 vents. The 151 vents without ages were grouped into 97 events, translating into 1.56 vents per event. Vent age groups (n = 58) averaged 6.12 vents per group, further distilled into 2.69 events per group. Excluding the 11 age groups that were unaffected by vent-to-event filtering, these values are 7.32 vents per group and 3.09 events per group. For the 220 events that represented the combination of at least two vents, 1.56 was the average number of vents per event. The majority of these clustered vents lie north of the axial volcanic zone within the Craters of the Moon region, southeast of INL, and to the northeast of INL (Figure 4.2).

4.2 Spatial Density Estimation

Values utilized for spatial density estimation included the outputs of the vents-to-events process combined with the list of 32 buried vents. For the 538 vents and 288 events the optimal bandwidths derived from the SAMSE method, $\mathbf{H}_v$ (vents) and $\mathbf{H}_e$ (events), are;

$$\mathbf{Hv} = \begin{bmatrix} 167.812327 & 103.885569 \\ 103.885569 & 105.096492 \end{bmatrix} \quad and \quad \mathbf{He} = \begin{bmatrix} 228.070781 & 151.867503 \\ 151.867503 & 176.583966 \end{bmatrix}$$

37
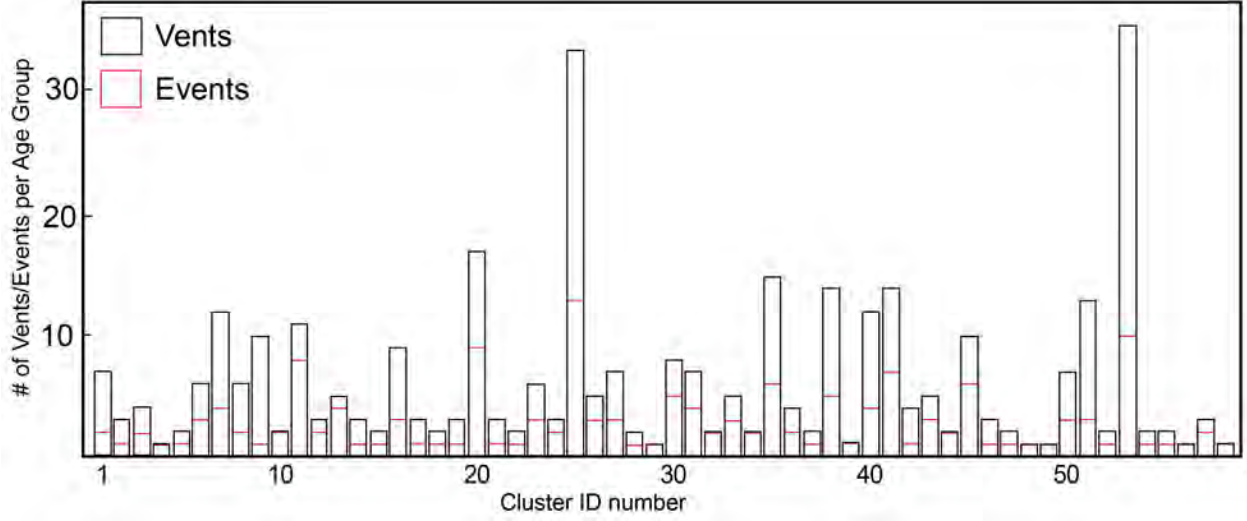
Figure 4.1: Histogram plot of the number of vents and events per temporal cluster. The average number of vents per group is 6.12, while the average number of events per group is 3.98. The ages associated with each of these clusters, numbered 1 through 58, can be found in Table 2 of Appendix C.

These bandwidths describe spatial variations in the 4 cardinal directions (N-S, E-W). The square root of these bandwiths describe the smoothing applied to the spatial varitions, in km, and are:

$$\sqrt{\mathbf{Hv}} = \begin{bmatrix} 11.966341 & 4.961754 \\ 4.961754 & 8.970924 \end{bmatrix} \quad and \quad \sqrt{\mathbf{He}} = \begin{bmatrix} 13.910209 & 5.880211 \\ 5.880211 & 11.916673 \end{bmatrix}$$

These matrix values correspond with smoothing of 9 km in the N-S direction and 12 km in the E-W direction for the vents, oriented at 50°, and 12 km in the N-S direction and 14 km in the E-W direction for events, oriented at 60°. The first and second standard deviations of the Gaussian smoothing ellipses are inset within the spatial density maps (Figures 4.3 and 4.4). The summation of these individual kernels for the vent and event fields were visualized as spatial density maps (Figures 4.3 and 4.4). Two modeled data sets of 10,000 potential eruptive coordinates, one for vents and another for events, were sourced from these plots (Figures 4.5 and 4.6).
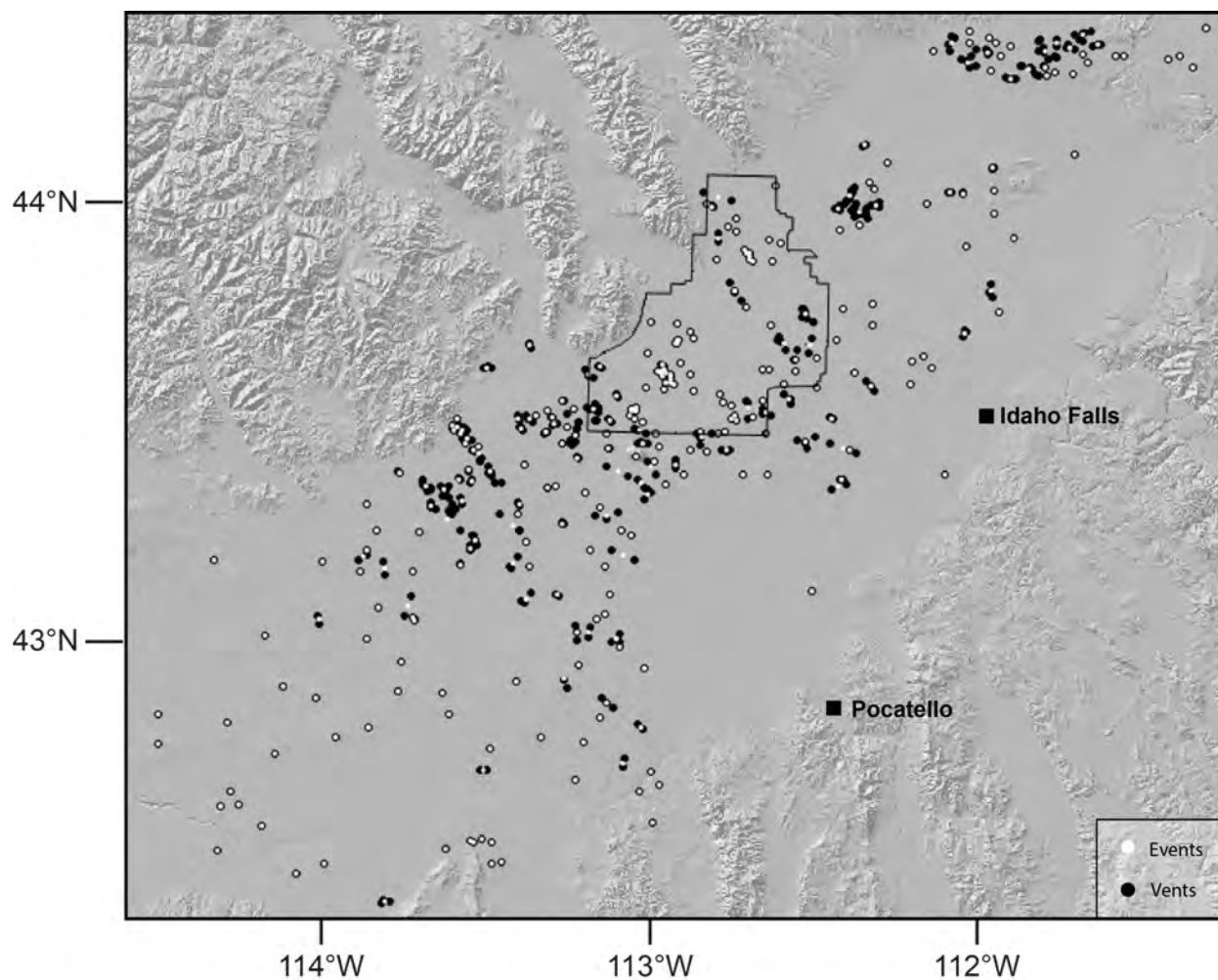
Figure 4.2: Map showing the distribution of vents and events on the ESRP. The black dots represent vents, the white dots events, and the white dots with black outlines locations were vents and events contain the same coordinates. The comparison of these datasets highlights clusters of dependent eruptive centers around Craters of the Moon, along the southwest boarder of INL, just to the northeast of INL, in the northeast corner of the map area, and along the axial volcanic zone.

39
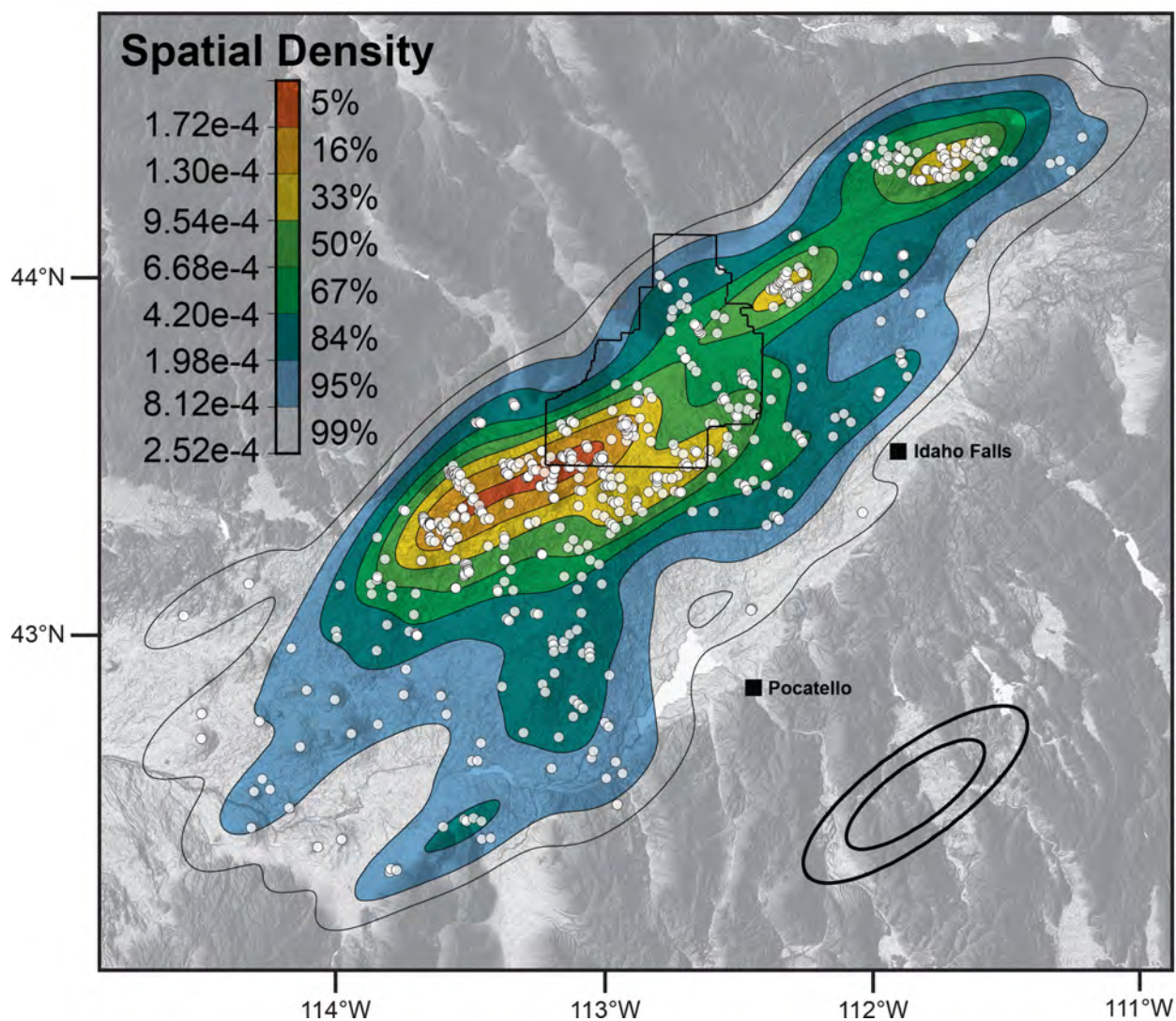
Figure 4.3: Spatial density estimation of vents. Contours are drawn and shaded at the 25th, 50th, 75th, 95th, and 99th percentile boundaries. The ellipse on the lower right illustrates the shape of the kernel density function, with the concentric ellipses representing the 68th and 95th percentiles. The northeast-southwest shape is consistent with the alignment of the axial volcanic zone.
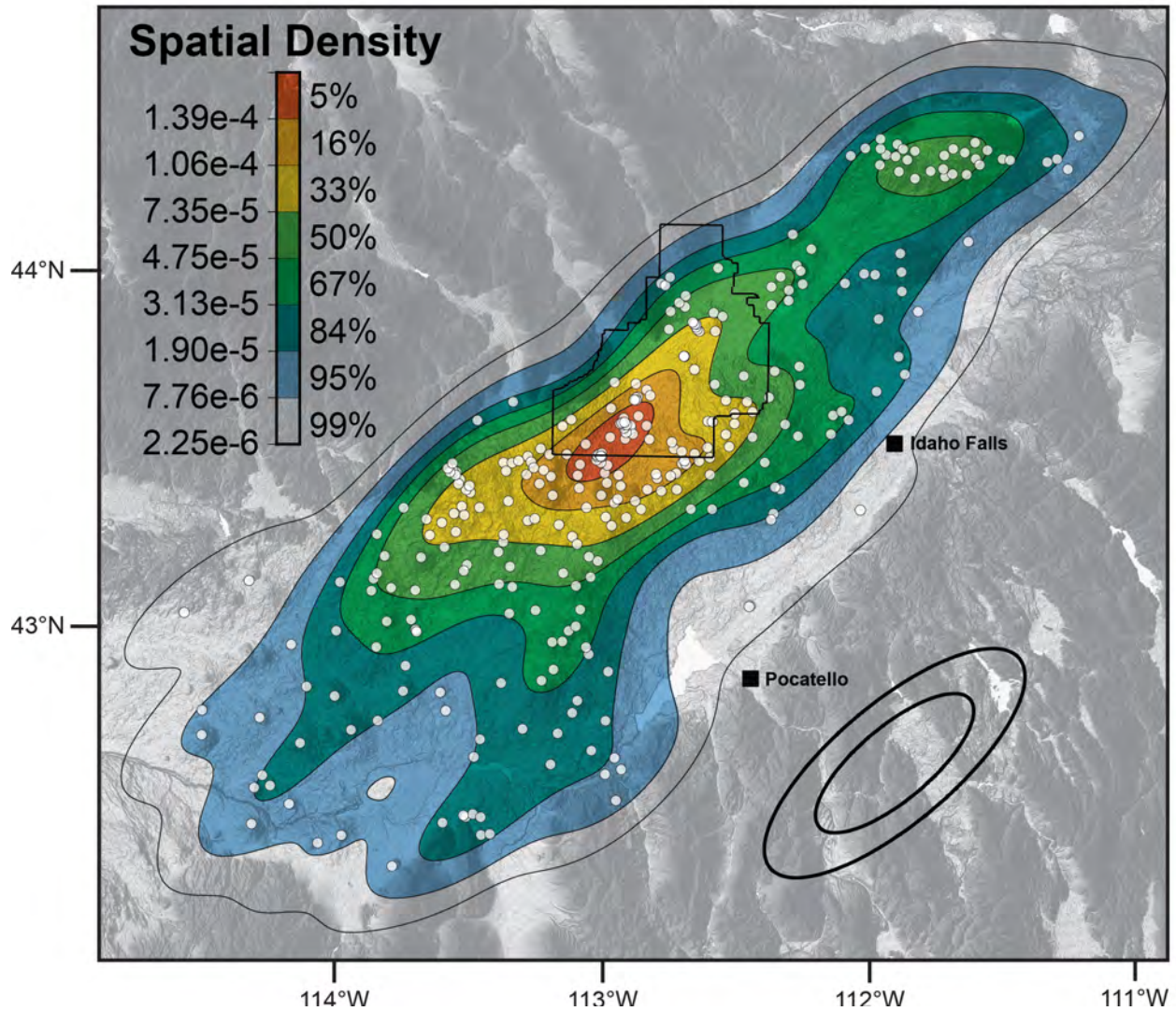
Figure 4.4: Spatial density estimation of events. Contours are drawn and shaded at the 25th, 50th, 75th, 95th, and 99th percentile boundaries. The ellipse on the lower right illustrates the shape of the kernel density function, with the concentric ellipses representing the 68th and 95th percentiles. The northeast-southwest shape is consistent with the alignment of the axial volcanic zone.
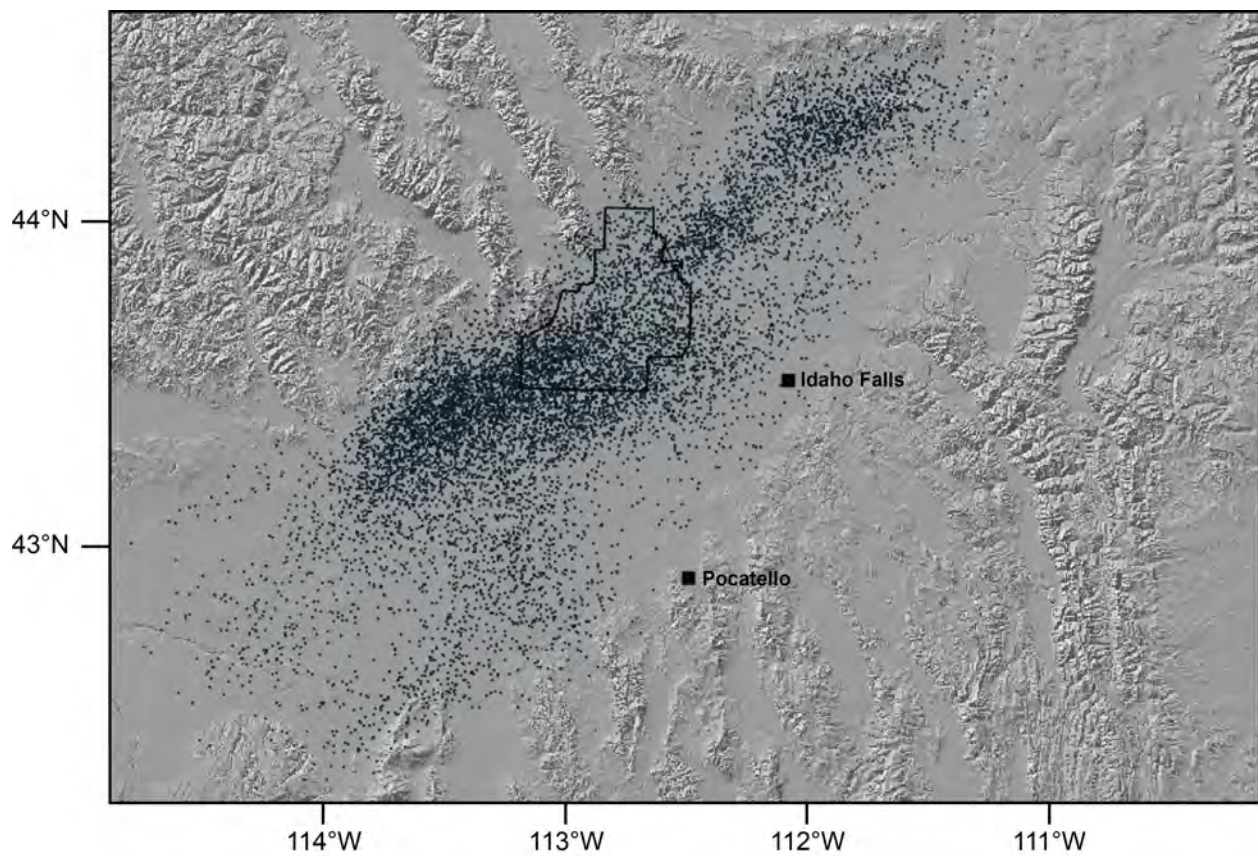
Figure 4.5: Map of 10,000 modeled vent locations. These vent locations were stochastically sampled from the vent spatial density map (Figure 4.3).
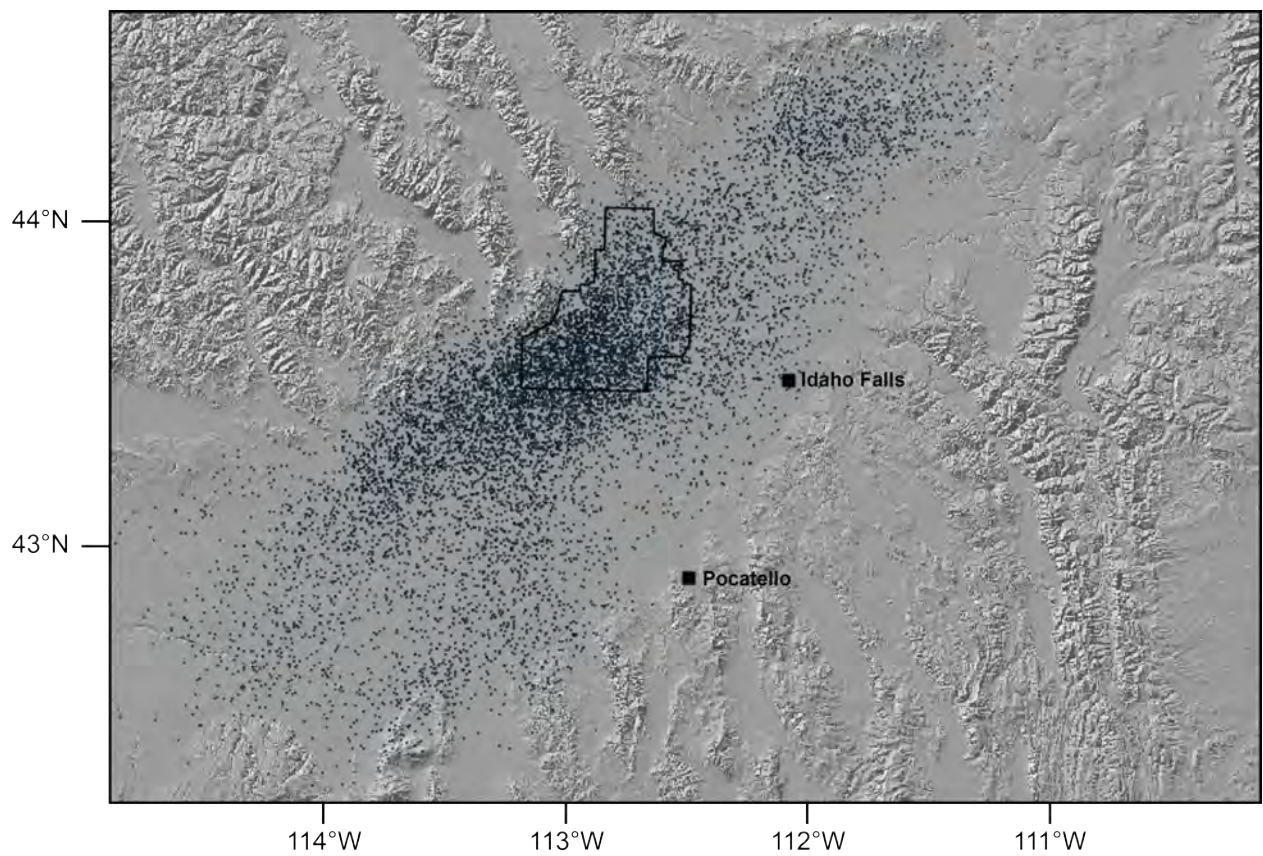
Figure 4.6: Map of 10,000 modeled event locations. These event locations were stochastically sampled from the event spatial density map (Figure 4.4).

Table 4.1: Lava Flow Simulation Results

Hazard	INL	Idaho Falls	Pocatello
Inundation by vent flow	25.45%	0.10%	0.00%
Vent eruption within boundary	18.27%	0.01%	0.00%
Inundation by event flow	33.74%	0.36%	0.00%
Event eruption within boundary	25.85%	0.11%	0.00%

Values based on conditional probability out of 10,000 runs

4.3 MOLASSES - Lava Flow Simulation

10,000 flows were simulated for eruptions initiating from a list of vents stochastically sampled from a spatial density map (Figure 4.7). Of these 10,000 flows, 2,545 breached the boundaries of INL (Figure 4.8) and 1,827 initiated inside the boundaries (Figure 4.9). The city of Idaho Falls was inundated by 10 flows, with 1 source located within a 5 km radius of the city center. Pocatello was not inundated by a single iteration. A flow to the west came within 10 km of the city, but was blocked by the Bannock Mountain Range. Similarly, 10,000 flows were simulated for eruptions initiating from a list of events (Figure 4.10), with 3,374 inundating INL (Figure 4.11) and 2,585 erupting inside the laboratory's boundaries (Figure 4.12). Idaho Falls was inundated 36 times, with 11 eruptions occurring within a 5 km radius. Again, Pocatello was not inundated by lava flows; the closest flow was located 15 km to the north. These results are summarized in Table 4.1.
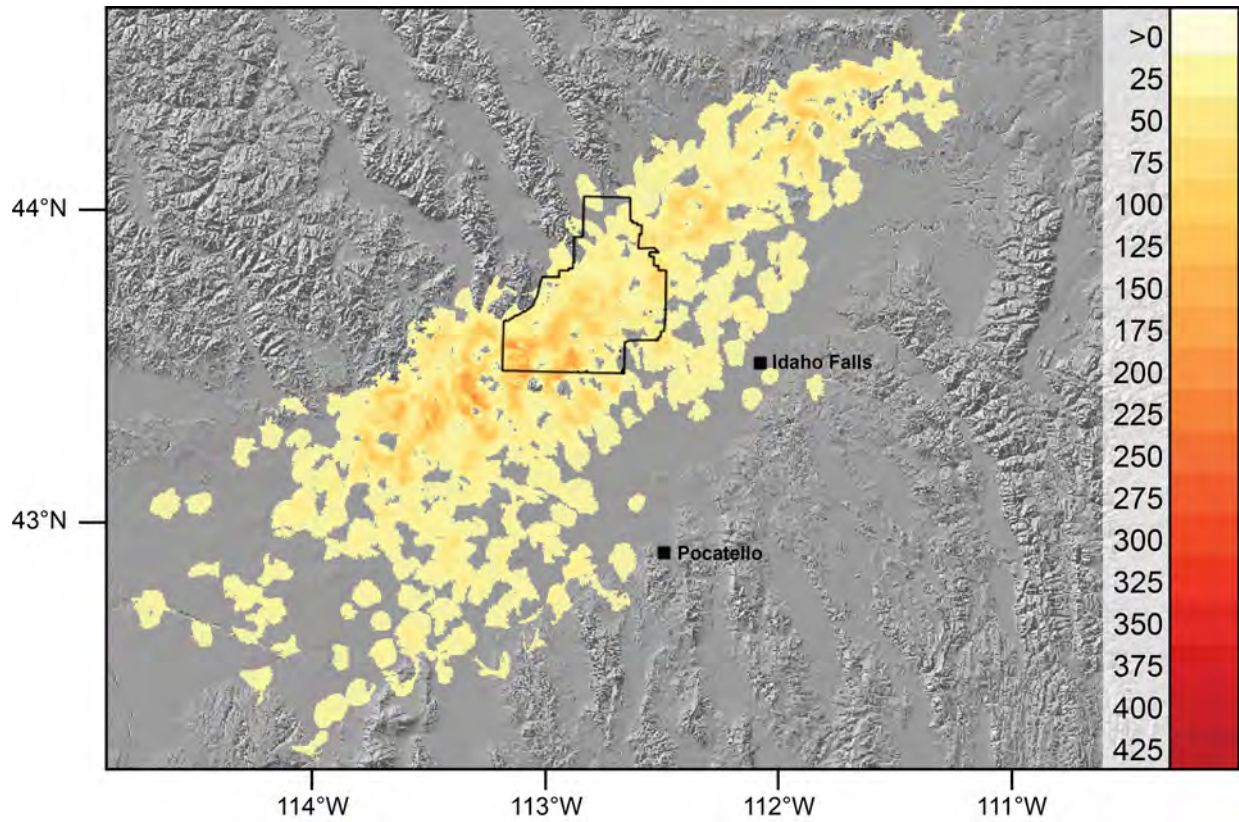
Figure 4.7: Map of 10,000 lava flows erupted from vents. 2,545 flows inundate INL, 10 Idaho Falls, and 0 Pocatello. Within INL the site of greatest inundation is located in the southwest corner, with 200 inundations out of 10,000 runs. The site of greatest inundation plain-wide was impacted 240 times out of 10,000 runs and is located 13.5 km from the southwest corner of INL.
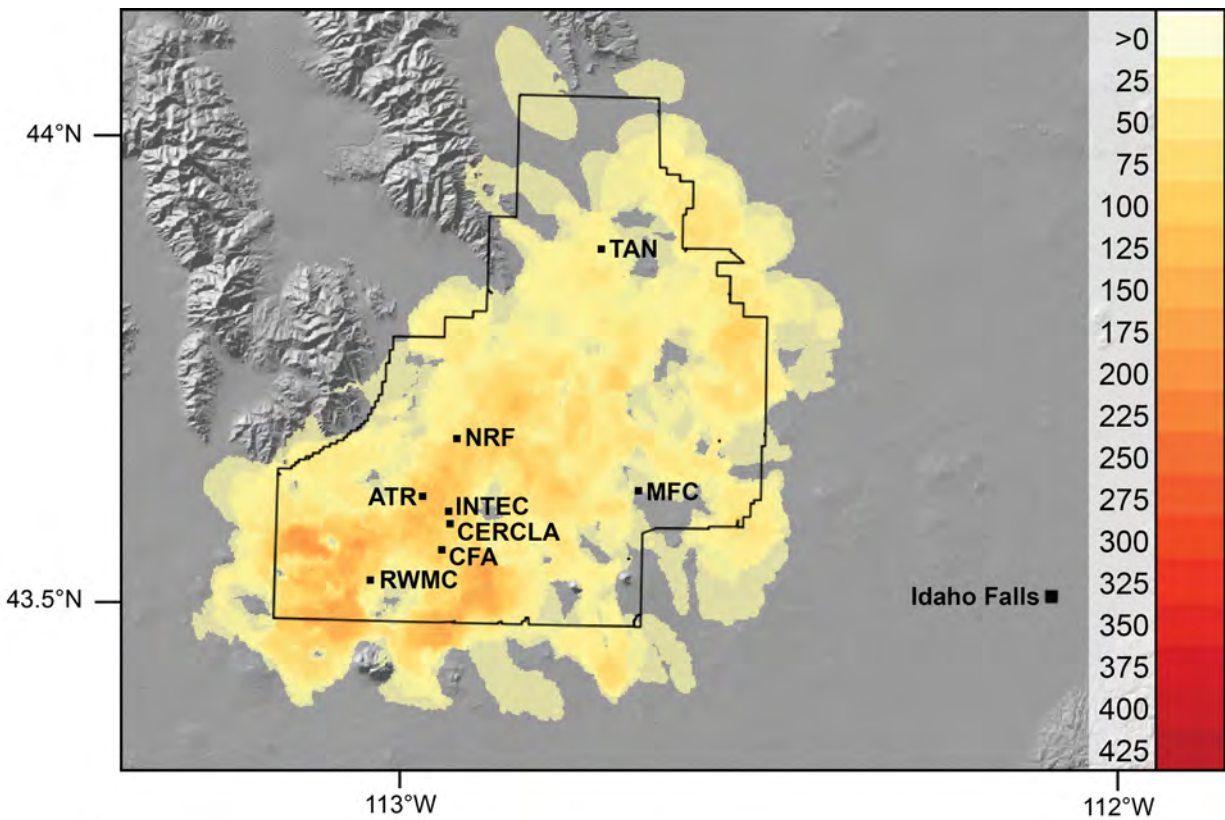
Figure 4.8: Map of vent-sourced lava flows that inundate INL. 2,545 lava flows from 10,000 simulations inundate INL. The southwest corner of INL is the most vulnerable.
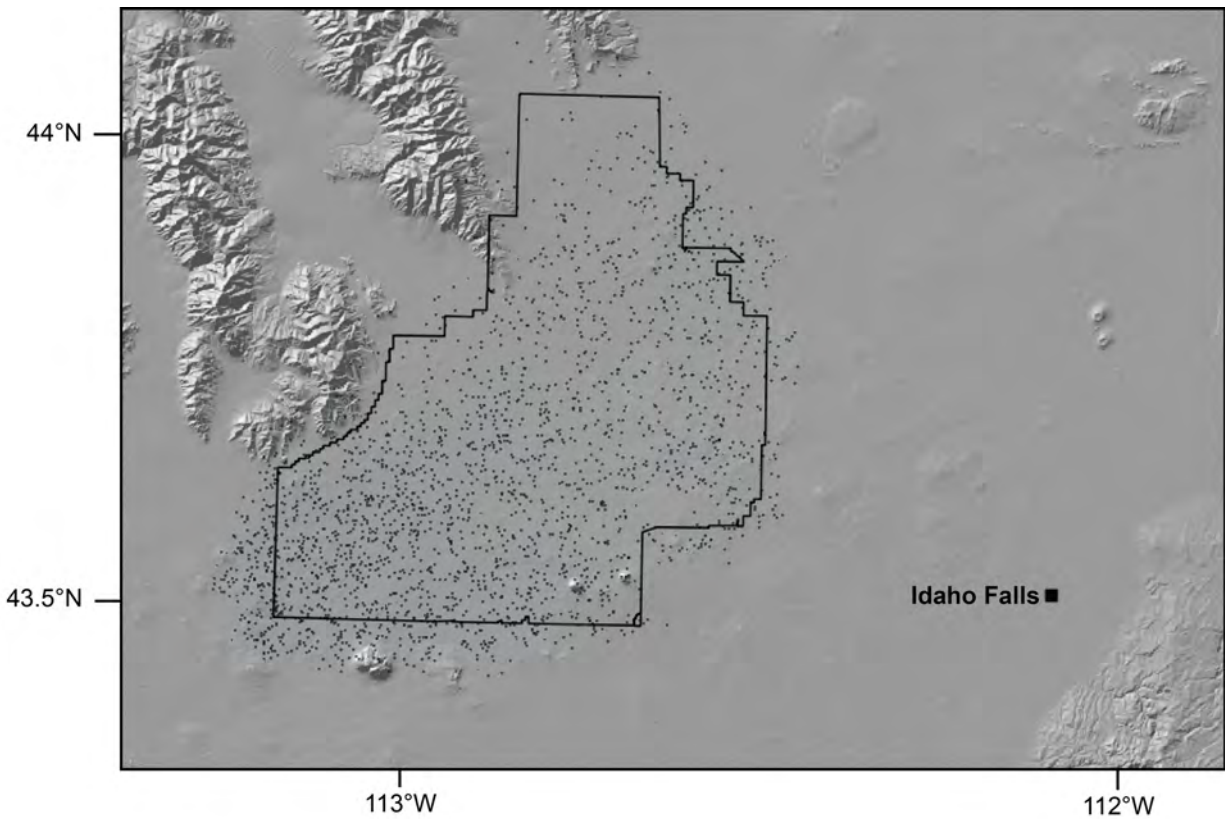
Figure 4.9: Map of 2,545 vent locations that inundate INL. 1,827 of these sources are located within the boundaries of INL. The greatest distance an inundating vent from the boundary is 10 km to the north, located within the Lemhi Valley.
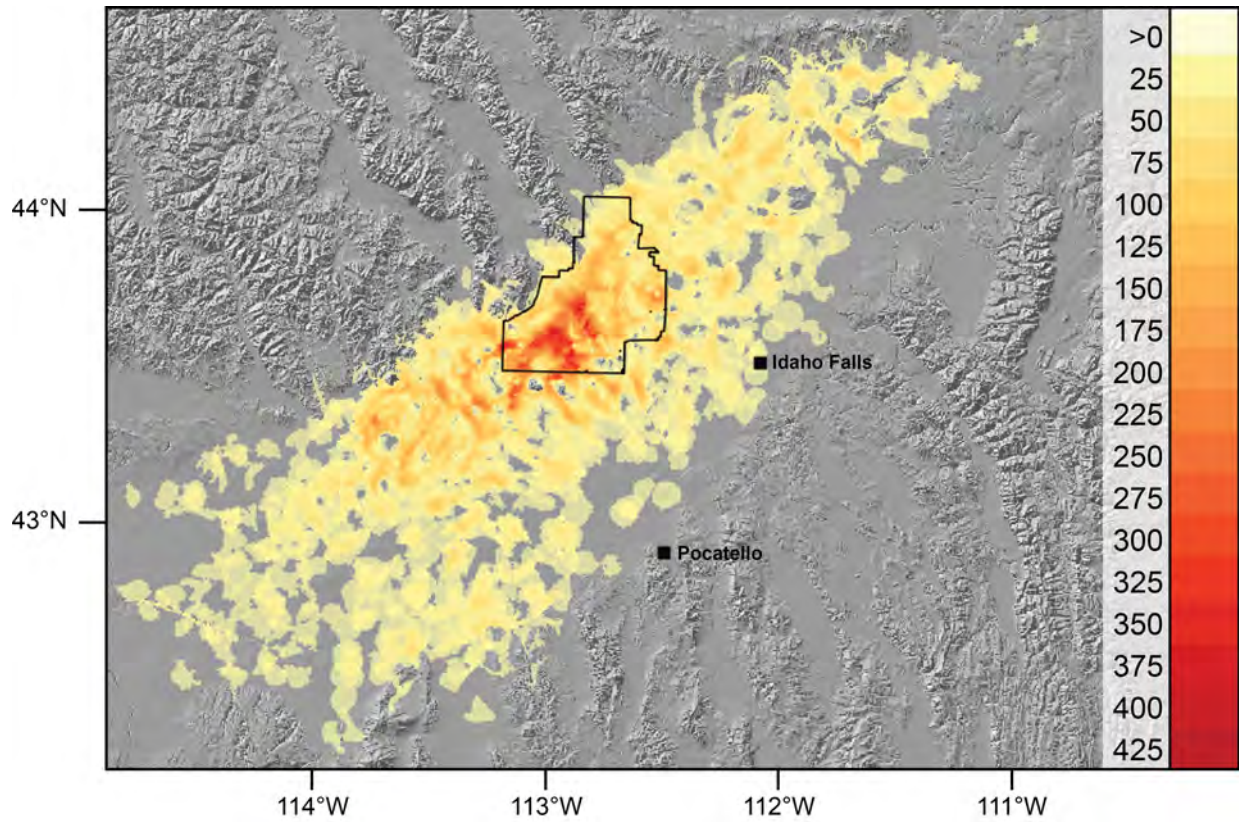
Figure 4.10: Map of 10,000 lava flows erupted from the events. 3,374 flows inundate INL, 36 Idaho Falls, and 0 Pocatello. Within INL the site of greatest inundation is located in the southwest corner, with 414 inundations out of 10,000 runs. This is also the site of greatest inundation plain-wide.
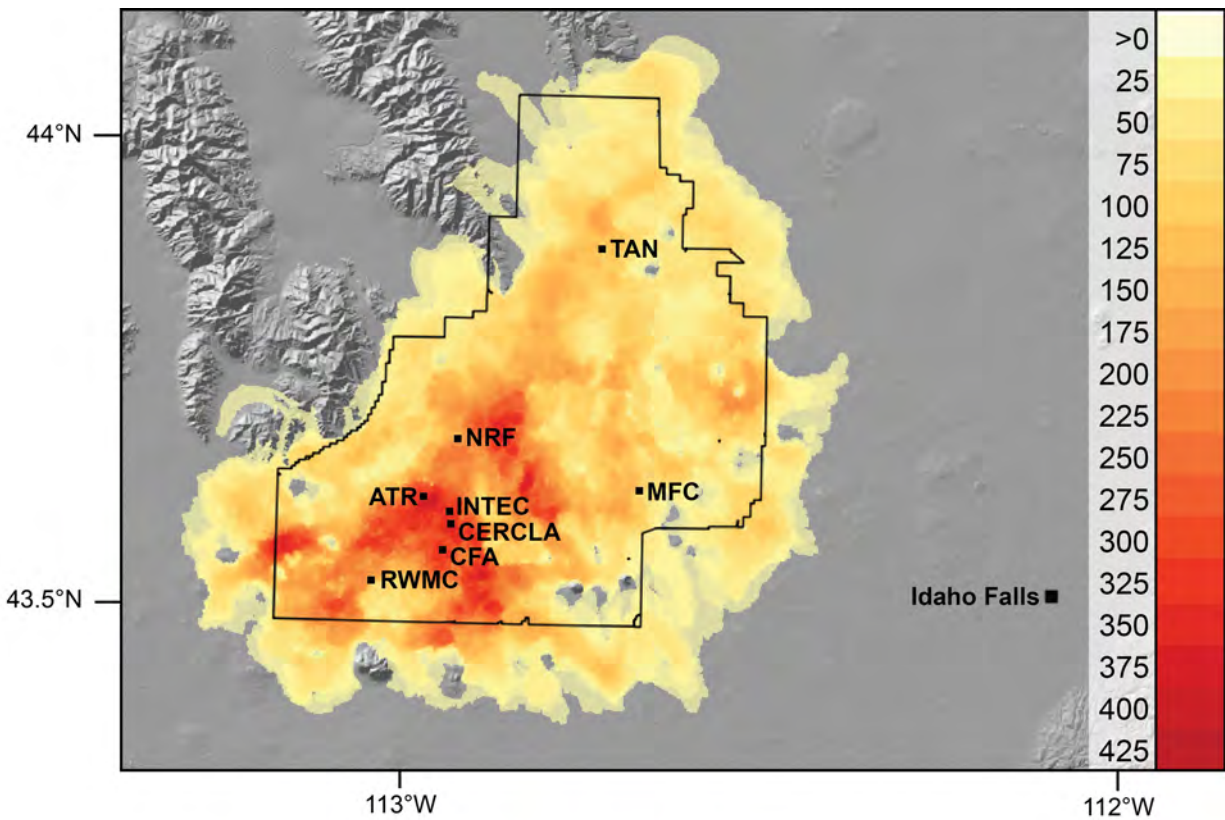
Figure 4.11: Map of vent-sourced lava flows that inundate INL. 3,374 lava flows from 10,000 simulations inundate INL. The western half of INL is the most vulnerable to inundation.
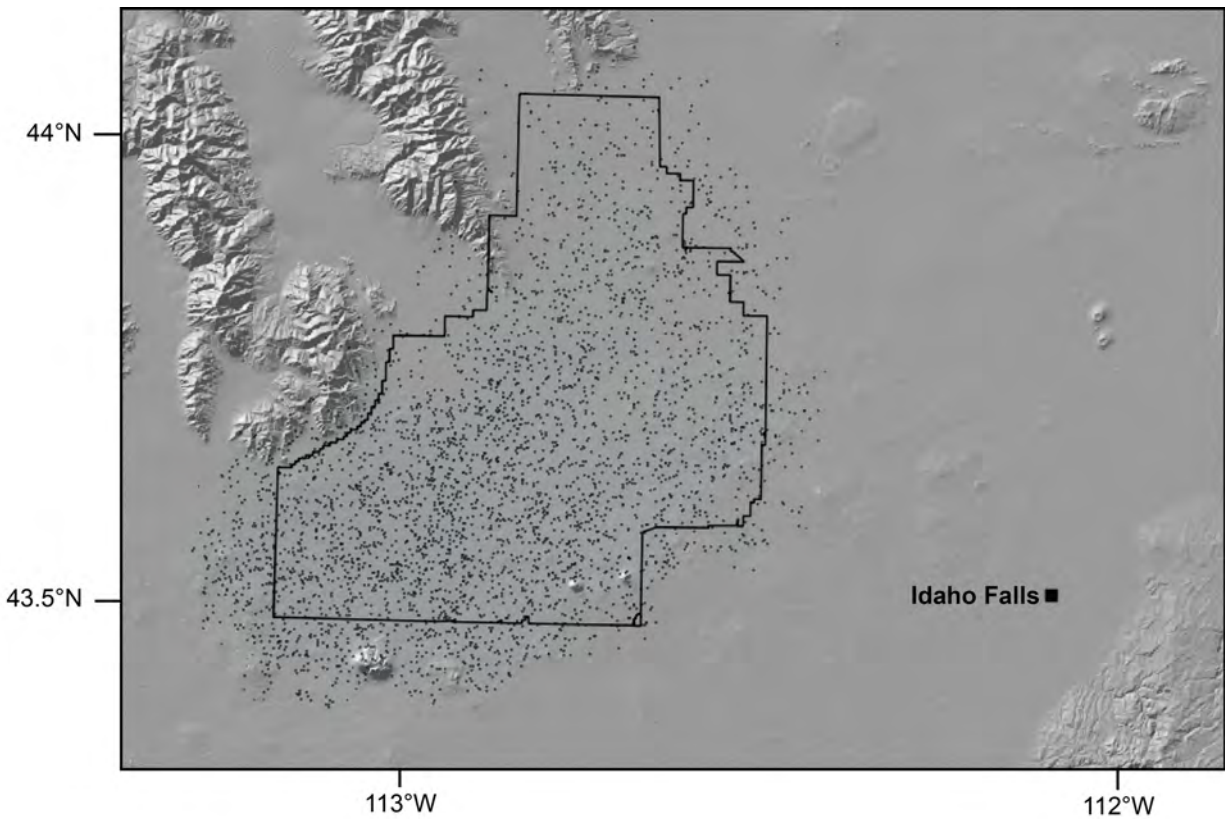
Figure 4.12: Map of 3,374 vent locations that inundate INL. 2,585 of these sources are located within the boundaries of INL. The greatest distance an inundating vent from the boundary is 10 km to the south, west of Big Southern Butte.
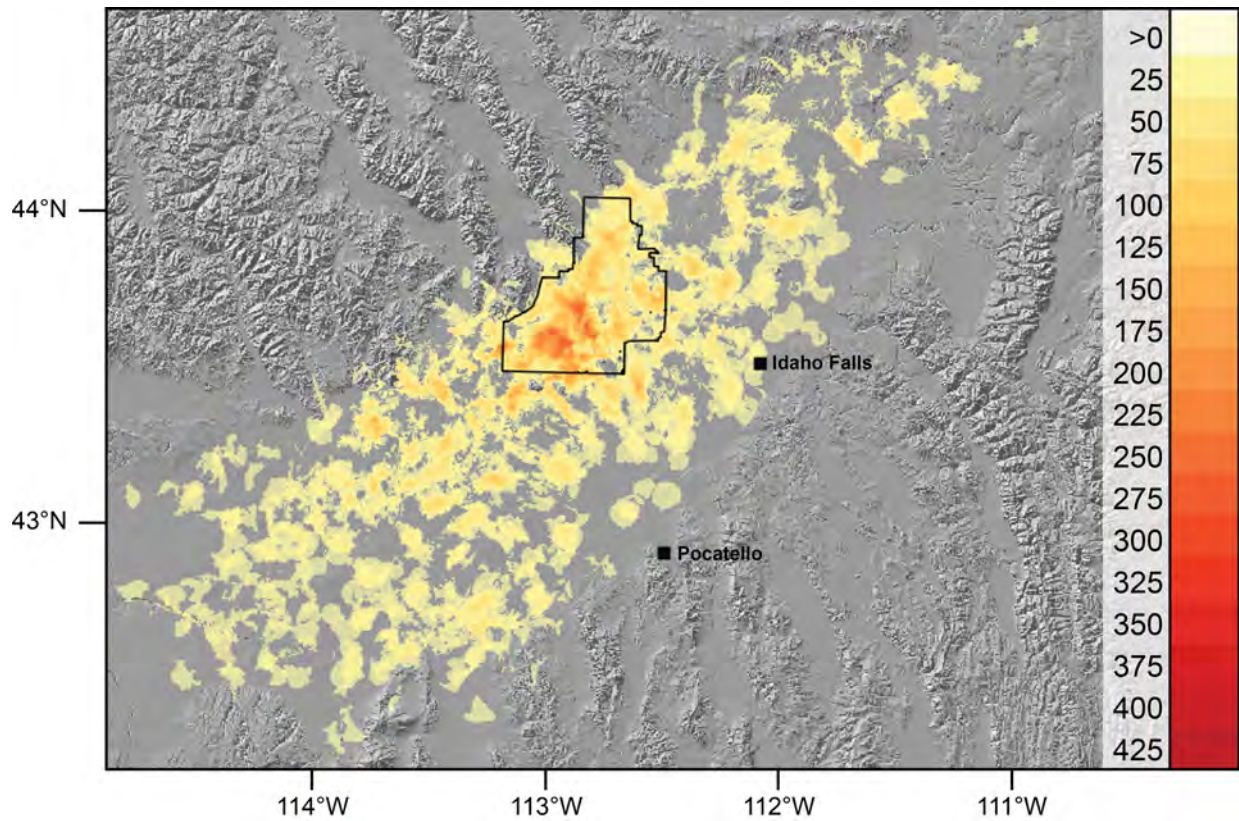
Figure 4.13: Map of the differential between the simulated vent and event flows. The region of greatest disparity is located within the boundaries of INL, focused in its center and soutwest corner.
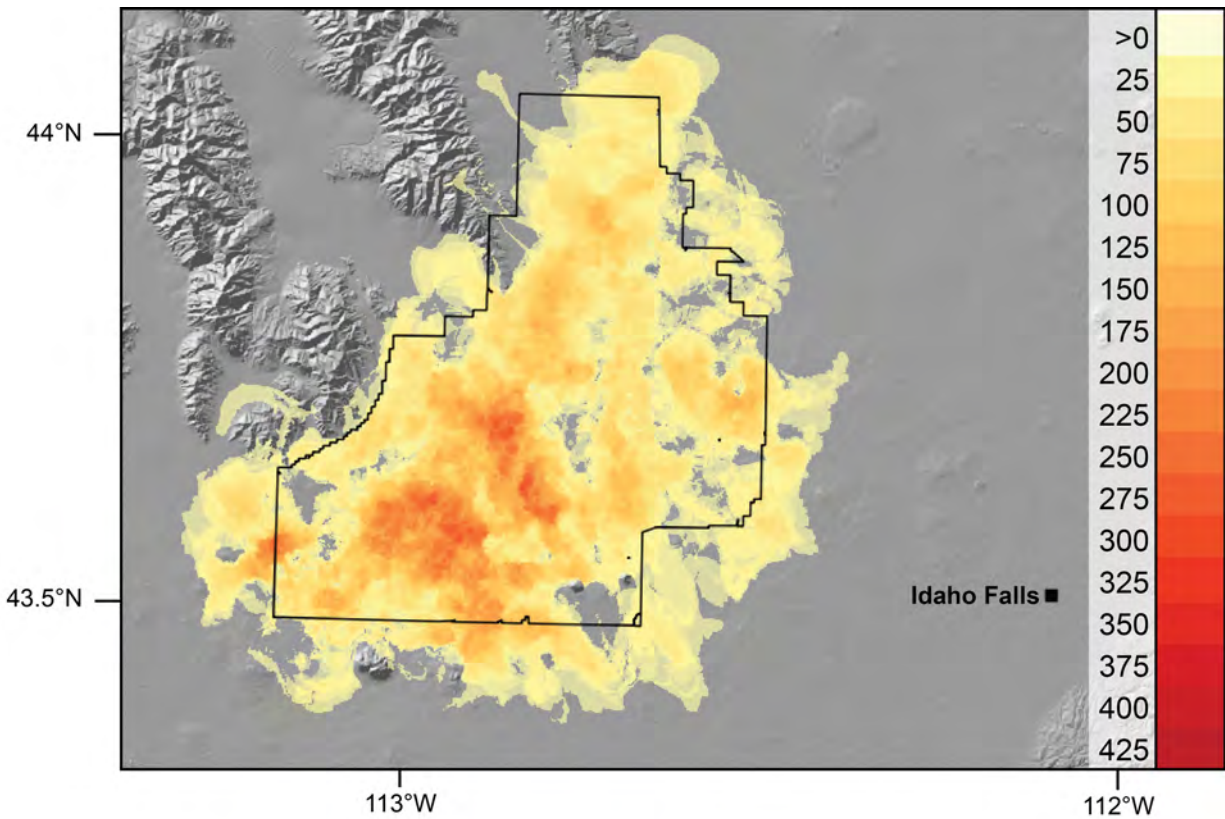
Figure 4.14: Map of the differential between the vent and event flows that inundate INL. The region of greatest disparity is located within the boundaries of INL, focused in its center and soutwest corner.

Table 4.2: Recurrence Interval Inputs

Data Set	# of eruptions (N)	oldest datum (T_0)	youngest datum (T_M)
Surface Vents	506	1.21 Ma	2.08 ka
Surface Events	256	1.21 Ma	2.08 ka
INL corehole	2,394	1.87 Ma	95.00 ka

4.4   Recurrence Interval

Using ages from the surface flows an annual eruption probability of 4.16 x 10^{-4} for vents was obtained using the recurrence rate of 2,404 years, while an annual eruption probability of 2.11 x 10^{-4} for events was calculated using a recurrence rate of 4,737 years between eruptions. Ages from corehole data resulted in an eruption probability of 1.35 x 10^{-3} using a recurrence rate of 739 years between eruptions. Inputs for all RI calculations can be found in Table 4.2.

5. Discussion

This study is intended to provide an estimate of the long-term lava flow hazard potential for INL and cities on the ESRP. This forecast is built on the assumptions that an eruption will transpire in years to come and that previous activity provides a basis from which future occurrence may be extrapolated. The long-term aspect of this hazard assessment is particularly important given the presence of nuclear facilities on the ESRP. Failure to approve the creation of a central repository beneath Yucca Mountain in Nevada has led to the continued containment of spent nuclear fuel on site where it was generated. This, along with the active use of radioactive material at INL, has created an environmentally sensitive location that requires long term consideration for the lava flow hazard it faces. A logic tree was created to combine the different elements of this research in order to assess the total hazard posed by lava flow inundation on the ESRP (Figure 5.1).
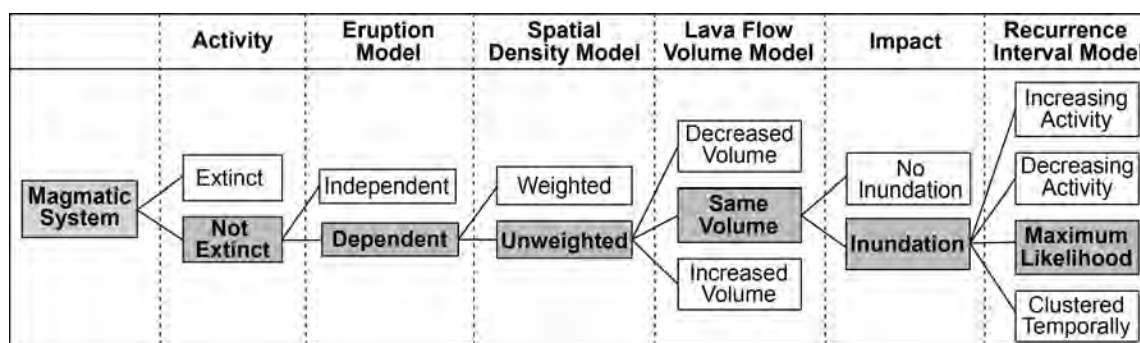
Figure 5.1: Logic tree for lava flow hazard assessment on the ESRP. The tree displays successive decisions required regarding the models used in an assessment. The preferred model determined by this study is noted in the grey tiles.

5.1   Activity

The first step is to determine if the system is still active. Given the geologically recent voluminous activity at Craters of the Moon (~30 km^3 during the latest Pliestocene and Holocene), the expectation of future activity is reasonable. The most recent eruption, 2,076 years ago, still lies within the recurrence interval for surface vent and event datasets, giving further credence to the assumption that renewed activity will occur. These probabilities are represented as '1' for non-extinct and '0' for extinct.

5.2   Eruption Model

Once it has been determined that future activity is likely, an appropriate eruption model is chosen. The type of computational lava flow model employed may place constraints on which eruption model is most suitable. Distilling vents into a list of independent events establishes an eruption model where the probability that one event occurs does not affect the probability of another event occurring. The number of vents per events is summarized in Table 5.1.

It is likely that an event consists of far more vents than is reported using this process. For example, the current eruption of Pu'u Ō'ō on Kīlauea has been ongoing since 1983 and has involved at *least* 15 vents. Many of the early eruptive centers have been paved over by younger lava flows and are only known due to the extensive monitoring of the eruption. It is likely that the same progression occurs on the ESRP. These results suggest further dating is required for regions with high vent concentrations in order to obtain a more accurate assessment of temporal distribution; the un-dated vents clustered in the northeast corner of the study area are the best candidates. Their age is currently listed in publications as 'Pliestocene' (2.6 Ma–11,700 ya), a range too expansive to be useful for classifying events based on the timing of eruptions. Obtaining even relative ages would be beneficial, as determining vent interdependence is more important than weighting vents based solely on age for this step in the process.

Table 5.1: Vent and Event Statistics

	Vent	Event
# of surface points	506	256
# of total points	538	288
Average # vents per eruption	1	1.97
Average # of vents per dated eruption	1	2.23
Average # of vents per undated eruption	1	1.56

5.3 Spatial Density Estimation

After the eruption model is selected, it is then determined if the data points will be weighed based on their age for spatial density estimation. Though hazard assessments often rely upon the age of recent volcanism to help determine the next likely location of eruption (Harburger, 2014), the wide spatial distribution of latest Pliestocene and Holocene flows suggests this approach is not appropriate for the ESRP (Figure 2.2). As the North American plate migrates to the west-southwest over the plume, surface activity will eventually transpose to the east-northeast (a process illustrated by the eastward age progression of calderas in Figure 2.1). The rate at which this is occurring is relatively slow (2.3 cm/year) and is insignificant when compared to the spatial density grid resolution of 1 km x 1 km.

It is assumed by the spatial density models that the locations of vents and events accurately represent the potential distribution of future volcanic activity on the ESRP. This assumption is beholden to the completeness of the vent catalog; the inclusion of buried vents attempts rectify any omissions caused by the burial of older eruptive centers by younger lava flows or s ediment. Given the high concern for INL, it is unsurprising that the majority of past drilling campaigns focus on this locale. This emphasis may create unintentional biasing towards the number of buried vents located in the subsurface in this region. A spatial density map of vents in the region excluding the sub-surface vents can be found in Wetmore et al. (2009).

The vent and event distributions are point processes, where each new vent or event creates an additional point. The spatial density estimates are statistical models of these point processes. It is assumed the respective bandwidths are estimated in a way that reflects a true, but unknown point process. For this reason, it is important to view these results in conjunction with subsurface and geophysical models (Appendix A). Uniting the information present in these models provides insight to the location of magma transport and storage within the crust. The presented geophysical surveys all show an anomaly, assumed to be a mafic sill, whose dominant axis runs parallel the axial volcanic z one. A comparison of the total basalt thickness of the ESRP (Figure 2.3) with the spatial density plots (Figures 4.3 and 4.4) suggests that the vent spatial density model is a better estimation of this unknown point process as it relates to the total distribution of lava across the ESRP.

5.4   Lava Flow Simulation

The next step in the tree concerns choices regarding eruption thicknesses and volumes modeled by the lava flow simulations. These parameters are relatively consistent for flows across the ESRP and are therefore extrapolated from observational data. Other models could address deviations in magma chemistry that affect flow thickness and eruptive volume. Although Craters of the Moon lavas are move evolved than the bulk of those on the rest of the ESRP, they erupted concurrently with primitive lavas elsewhere on the plain. As a result, models that diverge from the geologic record are not currently appropriate for the ESRP and are therefore assigned a probability of '0'. The model based on observational data is assigned a probability of '1'.

Within the choice of using observational data exists the option of modeling vents differently than events. Though an event represents a conceptually different eruption than a vent, it is important to view parameter selection within the context of what is ultimately being modeled; inundation area. In a study of the 1984 Mauna Loa eruption that threatened Hilo, Kauahikaua et al. (2013) assert that, given a longer eruption duration, the city would likely be inundated. (Rowland et al., 2005) dispel this idea through modeling with FLOWGO

and state that effusion rate is a more important factor in determining lava flow length. Effusion rates are highest in the initial phases of an eruption. Subsequent sustained low effusion rate eruptions typically have low length to width ratios (Kilburn and Lopes, 1988). Stated differently, sustained eruptions tend to reach the majority of their maximum length within the first phases of activity but continue to build a compound flow field as the effusion rate drops and levels off. By selecting the same thickness and volume parameters this model is essentially erupting the first vent within an e vent. Given that the greatest concern is whether or not an eruption will impact INL or cities on the ESRP, modeling the furthest extent of flow is the main goal.

5.5   Recurrence Intervals

The final step in the process prior to calculating the annual probability of inundation is to determine the RI of volcanism on the ESRP. This information allows an annual chance of occurrence to be assigned to the results of the lava flow simulations. RI selection is driven by trends in the data, which are greatly affected by the quality of and completeness of the eruption record. RIs can illustrate increases or decreases in activity rate, temporal cluster-ing patterns, or the average distribution of events over a selected time period (maximum likelihood).

Prior to the Craters of the Moon eruptions, trends appear relatively stable through 500 ka (Figure 3.5). It is possible that the lull in activity from 500 ka–1.2 Ma is a reflection of sparse data coverage. Findings from corehole RI directly conflict with this trend and suggest that activity in the past may have been more frequent. Both of these results should be considered in a plain-wide context. To put things into perspective, the total volume of the ESRP ($4 \times 10^4 \, \text{km}^3$ - Kuntz (1992)) divided by the average volume of an eruption ($1.20 \, \text{km}^3$ - this study) yields 3,333 total vents. At best the current RIs consider only 15% of eruptive centers for the surface vent RI and 71% for the corehole RI, though these are likely overly optimistic estimates. Other authors assert the ESRP may be comprised of 8,000 potential shields (Kuntz et al., 1992)) which drop those figures down to only 6.3%

and 30%, respectively. These disparities in coverage suggest a model that makes the fewest assumptions, the maximum likelihood approach, is the best option.

Of the two maximum likelihood models, the surface RI calculations better represent an accurate rate of future eruptions over the corehole RI. Nearly 3 RIs have passed since the last eruption and, with the exception of Craters of the Moon (the data from which the corehole RI does not incorporate), no other eruptions fit in line with this rate. For this reason, only the surface vent/event RI values were used to calculate annual inundation probabilities.

5.6   Probability Calculation

The RIs were combined with the output of the lava flow simulations to determine the annual hazard probabilities using equation 5.1:

$$P\left[I > 1\right] = P\left[E > 1\right] P\left[I|E\right] \tag{5.1}$$

where the probability of an event, P[E], is equal to 1-exp(-λt), where λ is the recurrence rate and t is time. Inundation probabilities of 1.06 x 10^{-4} and 7.12 x 10^{-5} were calculated for vents and events, respectively. The probabilities of an eruption initiating within INL are 7.60 x 10^{-5} for vents and 5.45 x 10^{-5} for events. These values, as well as those for Idaho Falls and Pocatello, can be found in Table 5.2.

These data show that, in spite of careful consideration of vent dependence, flow model parameters, and RI, the difference between probabilities for vents and events is minor. When considered in terms of the International Atomic Energy Agency's (IAEA) determination of 10^{-7} and below as the level of acceptable risk, the disparity between these values is insignificant. Based on these probabilities it is clear that INL would benefit from developing a robust lava flow hazard mitigation plan, especially considering the sensitive nature of the site makes it impossible to relocate. While it may be possible to divert a lava flow around the most critical sites at the expense of surrounding infrastructure, the possibility

of an eruption initiating within close proximity to a nuclear reactor is the most concerning potential scenario. For this reason a lava flow hazard assessment that looks specifically at the inundation probabilities for critical sites within INL is needed. The current method of using INL boundaries as a barrier for inundation determination overestimates the hazard. A $<1\,km^2$ area with the greatest probability of inundation by a vent within INL (7.90×10^{-5}) is located within 5 km of the RWMC, still well above the IAEA's acceptable level.

Table 5.2: Lava Flow Hazard Probabilities for the ESRP

Hazard	Vent	Event
Inundation of INL	1.06×10^{-4}	7.12×10^{-5}
Eruption initiation within INL	7.60×10^{-5}	5.45×10^{-5}
Inundation of Idaho Falls	4.16×10^{-7}	7.60×10^{-7}
Eruption initiation within 5 km of Idaho Falls	4.16×10^{-8}	2.30×10^{-7}
Inundation of Pocatello	≈ 0	≈ 0
Eruption initiation within 5 km of Pocatello	≈ 0	≈ 0

6. Conclusions

This work joins a multitude of other hazard assessments for INL and serves as the first to incorporate computational models to predict the area of inundation for future lava flows. The process used for this work was based on that of Connor et al. (2012) and utilized the findings of Wetmore et al. (2009) as a foundation from which to expand. Two eruption models were used, one for vents (any mapped point on the ESRP from which lava has effused) and another for events (eruptions independent of one another). Potential eruptive centers were drawn from spatial density estimates of these vents and events and were used to simulate effusive eruptions on the ESRP with MOLASSES.

The results show that no flows inundated Pocatello and that few ($<1\%$) impacted Idaho Falls for the vent and event simulations. The values for Idaho Falls are 3 orders of magnitude less than the inundation probability for an eruption facing Flagstaff, Arizona (Harburger, 2014). 25.45% of vent flows and 33.74% of event flows breached the boundaries of INL. 18.27% of the vent and 25.85% of event simulations initiated on INL property. Annual inundation probabilities of 1.06 x 10^{-4} for vent-based flows and 7.12 x 10^{-5} for event-based flows are reported for INL, along with probabilities of annual eruption initiation within INL of 7.60 x 10^{-5} for vents and 5.45 x 10^{-5} for events. All of these values are well above the accepted hazard values listed by the IAEA.

Bibliography

Allmedinger, R. (1982). Sequence of late Cenozoic deformation in the Blackfoot Mountains, southeastern Idaho. *Cenozoic Geology of Idaho: Idaho Bureau of Mines and Geology*, 26:505–516.

Anders, M., Geissman, J., Piety, L., and Sullivan, J. (1989). Parabolic distribution of circumeastern Snake River Plain seismicity and latest Quaternary faulting: Migratory pattern and association with the Yellowstone hotspot. *Journal of Geophysical Research*, 94.B2:1589–1621.

Anders, M., Saltzman, J., and Hemming, S. (2009). Neogene tephra correlations in eastern Idaho and Wyoming: Implications for Yellowstone hotspot-related volcanism and tectonic activity. *GSA Bulletin*, 121.5(6):837–856.

Anders, M. and Sleep, N. (1992). Magmatism and extension: the thermal and mechanical effects of theYellowstone hotspot. *Journal of Geophysical Research*, 97:15379–15393.

Anderson, S., Ackerman, D., Liszewski, M., and Feiburger, R. (1996). Stratigraphic data for wells at and near the Idaho National Engineering Laboratory, Idaho. *U.S. Geological Survey Open-File Report*, 96-248(DOE/ID-22127):27.

Anderson, S. and Liszewski, M. (1997). Stratigraphy of the unsaturated zone and the Snake River Plain Aquifer at and near the Idaho National Engineering and Environmental Laboratory, Idaho. *U.S.Geological Survey Water-Resources Investigations Report*, 97-4183:65.

Aspinall, W., Carniel, R., Jaquet, O., Woo, G., and Hincks, T. (2006). Using hidden multi-state Markov models with multi-parameter volcanic data to provide empirical evidence for alert level decision-support. *Journal of Volcanology and Geothermal Research*, 153:112–124.

Barca, D., Crisci, G., DiGregorio, S., and Nicoletta, F. (1993). Cellular automata method for mode model lava flows: Simulation of the 1986-1987 eruption, Mount Etna, Sicily. In Kilburn, C. and Luongo, G., editors, *Active lavas: Monitoring and Modeling*, pages 291–309. London, University College of London Press.

Bebbington, M. and Cronin, S. (2011). Spatio-temporal hazard sestimation in the Auckland Volcanic Field, New Zealand, with a new event-order Model. *Bulletin of Volcanology*, 73(1):55–72.

Bebbington, M. and Lai, C. (1996). Statistical analysis of New Zealand volcanic occurrence data. *Journal of Volcanology and Geothermal Research*, 74(1-2):101–110.

Bleacher, J. and Greeley, R. (2003). Shield volcano slope distributions: An approach for characterizing Martian Volcanic Provinces. In *Lunar and Planetary Science XXXIV (2003)*.

Braile, L., Smith, R. B., Ansorge, J., Baker, M., Sparlin, M., Prodehl, C., Schilly, M., Healy, J., Mueller, S., and Olsen, K. (1982). The Yellowstone Snake River Plain seismic profiling experiment: crustal structure of the eastern Snake River Plain. *Journal of Geophysical Research*, 87:2597–2609.

Brott, C., Blackwell, D., and Ziagos, J. (1981). Thermal and tectonic implications of heat flow in the eastern Snake River Plain. *Journal of Geophysical Research- Solid Earth*, 86:11709–11734.

Chacón, J. and Duong, T. (2011). Unconstrained pilot selectors for smoothed cross-validation. *Australian & New Zealand Journal of Statistics*, 53(3):331–351.

Chacón, J. and Duong, T. (2013). Data-driven density derivative estimation, with applications to nonparametric clustering and bump hunting. *Electron. J. Statist.*, 7:499–532.

Chacón, J., Duong, T., and Wand, M. (2011). Asymptotics for general multivariate kernel density estimators. *Statistica Sinica*, 21(2):807–840.

Cochran, J. and Talwani, M. (1977). Free-air gravity anomalies in the world's oceans and their relationship to residual elevation. *Royal Astronomical Society Geophysical Journal*, 50:495–552.

Connor, C. and Connor, L. (2009). Estimating spatial density with kernel methods. In *Volcanic and tectonic hazard assessment for nuclear facilities*, pages 346–368. Cambridge University Press.

Connor, C. and Hill, B. (1995). Three nonhomogenous Poisson models for the probability of basaltic volcanism: Application to the Yucca mountain region. *Journal of Geophysical Research*, 100(10):107–110.

Connor, C., Stamatakos, J., Ferrill, D., Hill, B., Ofoegbu, G., Conway, F., Sagar, B., and Trapp, J. (2000). Geologic factors controlling patterns of small volume basaltic volcanism: Application to a volcanic hazards assessment at Yucca Mountain, Nevada. *Journal of Geophysical Research: Solid Earth*, 105(B1):417–432.

Connor, C. B., Chapman, N. A., and Connor, L. J., editors (2009). *Volcanic and Tectonic Hazard Assessment for Nuclear Facilities*. Cambridge University Press.

Connor, L., Connor, C., Meliksetian, K., and Savov, I. (2012). Probabilistic approach to modeling lava flow inundation: a lava flow hazard assessment for a nuclear facility in Armenia. *Journal of Applied Volcanology*, 1(3).

Costa, A. and Macedonio, G. (2005). Numerical simulation of lava flows based on depth-averaged equations. *Journal of Geophysical Research*, 32.

Crisci, G., Di Gregorio, S., Rongo, R., Scarpelli, M., Spataro, W., and Calvari, S. (2003). Revisiting the 1669 Etnean eruptive crisis using a cellular automata model and implications for volcanic hazard in the Catania area. *Journal of Volcanology and Geothermal Research*, 123:211–230.

Dixon, T., Robaudo, S., Lee, J., and Reheis, M. (1995). Constraints on present-day Basin and Range deformation from space geodesy. *Tectonics*.

Dragoni, M. and Tallarico, A. (1994). The effect of crystallization on the rheology and dynamics of lava flows. *Journal of Volcanology and Geothermal Research*, 59:241–252.

Duong, T. (2007). ks: Kernel Density Estimation and kernel Discriminant Analysis for Multivariate Data in R. *Journal of Statistical Software*, 21(1):1–16.

Duong, T. and Hazelton, M. (2003). Plug-in bandwidth selectors for bivariate kernel density estimation. *Journal of Nonparametric Statistics*, 15:17–30.

Fujita, E. and Nagai, M. (2015). LavaSIM: its physical basis and applicability. *Geological Society, London, Special Publications*, 426.

Furlong, K. (1979). An analytic stress model applied to the Snake River Plain (Northern Basin and Range province U.S.A.). *Tectonophysics*, 58(3):T11 – T15.

Greensfelder, R. and Kovach, R. (1982). Shear wave velocities and crustal structure of the Eastern Snake River Plain, Idaho. *Journal of Geophysical Research. Solid Earth*, 87:2643–2653.

Griffiths, R. (2000). The Dynamics of Lava Flows. *Annual Review of Fluid Mechanics*, 32:477–518.

Hackett, W. and Morgan, L. (1988). Explosive basaltic and rhyolitic volcanism of the eastern Snake River Plain. In Link, P. K. and Hackett, W. R., editors, *Guidebook to the Geology of Central and Southern Idaho*, pages 283–301. Idaho Geological Survey Bulletin.

Hackett, W. and Smith, R. (1994). Volcanic Hazards of the Idaho National Engineering Laboratory and Adjacent Areas. *Lockheed Martin Idaho Technologies Report*, INEL-94/0276:31.

Hackett, W., Smith, R., and Khericha, S. (2002). Volcanic hazards of the Idaho National Engineering and Environmental Laboratory, southeast Idaho. In Bonnichsen, B., White, C. M., and McCurry, M., editors, *Tectonic and Magmatic Evolution of the Snake River Plain Volcanic Province*, volume 30. Idaho Geological Survey Bulletin.

Harburger, A. (2014). Probabilistic Modeling of Lava Flows: A Hazard Assessment for the San Francisco Volcanic Field, Arizona. Master's thesis, University of South Florida.

Harris, A. and Rowland, S. (2001). FLOWGO: A kinematic thermo-rheological model for lava flowing in a channel. *Bulletin of Volcanology*, 63(1):20–44.

Hawaiian Volcano Observatory (2007). Can Hawaiian lava flows be diverted? website: http://hvo.wr.usgs.gov/volcanowatch/archive/2007/07$_1$2$_0$6.*html*.

Hemphill-Haley, M., Sawyer, T., Knuepfer, P., Forman, S., and Wong, I. (1994). Late Quaternary paleoseismicity and segmentation along the southern Lemhi Fault, southeastern Idaho. In Prentice, C., Schwartz, D., and Yeats, R., editors, *Proceedings of the Workshop on Paleoseismology*, pages 81–83. US Geological Survey Open File Report.

Hildreth, W., Halliday, A., and Christiansen, R. (1991). Isotopic and chemical evidence concerning the genesis and contamination of basaltic and rhyolitic magma beneath the Yellowstone Plateau volcanic field. *Journal of Petrology*, 32:63–138.

Hill, R., Cahalan, J., Khalil, H., and Wade, D. (1998). Development of small, fast reactor core designs using lead-based coolant. *Argonne National Laboratory*.

Hughes, S., Wetmore, P., and Casper, J. (2002). Evolution of Quaternary Tholeiitic Basalt Eruptive Centers on the Eastern Snake River Plain, Idaho. In Husges, S. S. and Thackray, G. D., editors, *Tectonic and Magmatic Evolution of the Snake River Plain, Idaho*, pages 143–168. Idaho Geological Survey.

Idaho National Laboratory (Accessed March 17, 2016a). Idaho National Laboratory: General Information. https://www.inl.gov/about-inl/general-information/.

Idaho National Laboratory (Accessed: March 17, 2016b). Idaho National Laboratory: INL Capabilities. https://www.inl.gov/about-inl/capabilities/.

Idaho State University (Accessed: November 13, 2015). Basalt Thickness - Snake River Plain. http://imnh.isu.edu/digitalatlas/geo/snkrvpln/basalt/srpbslt.htm.

Kauahikaua, J., Margriter, S., Lockwood, J., and Trusdell, F. (2013). Applications of GIS to the Estimation of Lava Flow Hazards on Mauna Loa Volcano, Hawai'i. In *Mauna Loa Revealed: Structure, Composition, History, and Hazards*, pages 315–325. American Geophysical Union.

Kilburn, C. and Lopes, R. (1988). The growth of AA lava flow fields on Mount Etna, Sicily. *Journal of Geophysical Research: Solid Earth*, 93(B12):14759–14772.

Kinman-Tavarez, S. (2015). Geophysical evidence for mid-crustal magma reservoirs in the Lassen Volcanic Region, California. Master's thesis, University of South Florida.

Kiyosugi, K., Connor, C., Zhao, D., Connor, L., and Tanaka, K. (2010). Relationships between volcano distribution, crustal structure, and P-wave tomography: an example from the Abu Monogenetic Volcano Group, SW Japan. *Bulletin of Volcanology*, 72:331–340.

Kubanek, J., Richardson, J., Charbonnier, S., and Connor, L. (2015). Lava flow mapping and volume calculations for the 2012–2013 Tolbachik, Kamchatka, fissure eruption using bistatic TanDEM-X InSAR. *Bulletin of Volcanology*, 77(12):1–13.

Kuntz, M. (1978). Geology of the Arco-Big Southern Butte area, eastern Snake River Plain, and potential volcanic hazards to the Radioactive Waste Management Complex, and other waste storage and reactor facilities at the Idaho National Engineering Laboratory, Idaho. Technical report, USGS.

Kuntz, M. (1992). A model-based perspective of basaltic volcanism, eastern Snake River Plain, Idaho. *in Link, P. K., Kuntz, M. A., and Platt, L. P., eds., Regional geology of eastern Idaho and western Wyoming: Geological Society of America Memoir 179*, pages 289–304.

Kuntz, M., Champion, D., Spiker, E., and Lefebvre, R. (1986). Contrasting magma types and steady-state, volume-predictable basaltic volcanism along the Great Rift, Idaho. *Geological Society of America Bulletin*, 97:579–594.

Kuntz, M., Skipp, B., Champion, D., Gans, P., Van Sistine, D., , and Snyders, S. (2007). Geologic map of the Craters of the Moon 30' x 60' quadrangle, Idaho. *U.S. Geological Survey Scientific Investigations Map 2969*, 1 plate(scale 1:100,000):64p pamphlet.

Kuntz, M. A., Champion, D. E., Spiker, E. C., Lefebvre, R. H., and McBroome, L. A. (1982). The Great Rift and the evolution of the Craters of the Moon lava field, Idaho. In Bonnichsen, B. and Breckenridge, R. M., editors, *Cenozoic Geology of Idaho*, pages 423–438. Idaho Bureau of Mines and geology.

Kuntz, M. A., Covington, H. R., and Schorr, L. J. (1992). Chapter 12: An overview of basaltic volcanism of the eastern Snake River Plain, Idaho. *Geological Society of America Memoirs*, 179:227–268.

Kuntz, M. A. and Dalrymple, G. B. (1979). Geology, geochronology and potential volcanic hazards in the Lava Ridge – Hells Half Acre area, eastern Snake River Plain, Idaho. *U.S. Geological Survey*, File Report 79(1657).

Kuntz, M. A., Skipp, B., Lanphere, M. A., Scott, W. E., Pierce, K. L., Dalrymple, G. B., Champion, D. E., Embree, G. F., Page, W. R., Morgan, L. A., Smith, R. P., Hackett, W. R., and Rodgers, D. W. (1994). Geologic map of the Idaho National Engineering Laboratory and adjoining areas, eastern Idaho. US Geological Survey Miscellaneous Investigations Series. Map 1-2330, scale 1:100,000.

Lanphere, M., Champion, D., and Kuntz, M. (1993). Petrography, age and paleomagnetism of basalt lava flows in coreholes Well 80, NRF 89-04, NRF 89-05, 116 and ICPP 123, Idaho National Engineering Laboratory. *U.S. Geological Survey Open File Report*, 93-327:40.

Leeman, W. (1982a). Development of the Snake River Plain-Yellowstone Plateau Province, Idaho and Wyoming: an overview and petrologic model. In Bonnichsen, B. and Breckenridge, R. M., editors, *Cenozoic Geology of Idaho*, volume 26, pages 155–177. Idaho Bureau of Mines and geology.

Leeman, W. (1982b). Oliving tholeiitic basalts of the Snake River Plain, Idaho. In Bonnichsen, B. and Breckenridge, R. M., editors, *Cenozoic geology of Idaho*, pages 181–192. Idaho Bureau of Mines and geology.

Leeman, W. and Vitaliano, C. (1976). Petrology of the McKinney basalt, Snake River Plain, Idaho. *Geological Society of America Bulletin*, 87:1777–1792.

Lockwood, J. and Lipman, P. (1987). Holocene eruptive history of Mauna Loa volcano. *US Geological Survey Professional Paper*, 1350(1):509–535.

Lockwood, J. and Torgerson, F. (1980). Diversion of lava flows by aerial bombing — lessons from Mauna Loa volcano, Hawaii. *Bulletin Volcanologique*, 43(4):727–741.

Mabey, D. (1982). Geophysics and Tectonics of the Snake River Plain. In Bonnichsen, B. and Breckenridge, R. M., editors, *Cenozoic Geology of Idaho*. Idaho Bureau of Mines and geology.

Mahony, S., Sparks, R., Connor, L., and Connor, C. (2009). Exploring long-term hazards using a Quaternary volcano database. In Connor, C., Chapman, N., and Connor, L., editors, *Volcanic and Tectonic Hazard Assessment for Nuclear Facilities*, pages 326–345. Cambridge University Press.

Marti, J., Aspinall, W., Sobradelo, R., Felpeto, A., Geyer, A., Ortiz, R., Baxter, P., Cole, P., Pacheco, J., Blanco, M., and Lopez, C. (2008). A long-term volcanic hazard event tree for Teide-Pico Viejo stratovolcanoes (Tenerife, Canary Islands). *Journal of Volcanology and Geothermal Research*, 178:543–552.

Martin, A., Umeda, K., Connor, C., Weller, J., Zhao, D., and Takahashi, M. (2004). Modeling Long-Term Volcanic Hazards Through Bayesian Inference: An Example from the Tohoku Volcanic Arc, Japan. *Geology Faculty Publications*.

Marzocchi, G., Sandri, L., Gasparini, P., Newhall, C., and Boschi, E. (2004). Quantifying probabilities of fvolcanic events: The example of volcanic hazard at Mount Vesuvius. *Journal of Geophysical Research*, 109.

Marzocchi, G., Sandri, L., and Selva, J. (2008). A probabilistic tool for long- and short-term eruption forecasting. *Bulletin of Volcanology*, 70:623–632.

Marzocchi, G., Sandri, L., and Selva, J. (2010). BET VH: A probablistic tool for long-term volcanic hazard assessment. *Bulletin of Volcanology*, 72(6):705–716.

Marzocchi, G. and Zaccarelli, L. (2006). A quantitative model for the time-size distribution of eruptions. *Journal of Geophysical Research*, 111.

Marzocchi, W. and Bebbington, M. (2012). Probabilistic eruption forecasting at short and long time scales. *Bulletin of Volcanology*, 74(8):1777–1805.

McCurry, M. and Rodgers, D. (2009). Mass transfer along the Yellowstone hotspot track I: Petrologic constraints on the volume of mantle-derived magma. *Journal of Volcanology and Geothermal Research*, 188(13):86–98.

McQuarrie, N. and Rodgers, D. (1998). Subsidence of a volcanic basin by flexure and lower crustal flow: The eastern Snake River Plain, Idaho. *Tectonics*, 17(2):203–220.

McQuarrie, N. and Wernicke, B. (2005). An animated Tectonic Reconstruction of Southwestern North America since 36ma. *Geosphere*, pages 147–172.

Mullineaux, D., Peterson, D. W., and Crandell, D. (1987). Volcanism in Hawai'i. volume Professional Paper 1350, chapter Volcanic Hazards in the Hawaiian Islands, pages 599–621. U.S. Geological Survey.

Nash, B., Perkins, M., Christensen, J., Lee, D., and Halliday, A. (2006). The Yellowstone hotspot in space and time: Nd and Hf isotopes in silicic magmas. *Earth and Planetary Science Letters*, 247:143–156.

Newhall, C. and Hoblitt, R. (2002). Constructing event trees for volcanic crises. *Bulletin of Volcanology*, 64:3–20.

Okui, Y. and Horii, H. (1997). Stress and time-dependent failure of brittle rocks under compression: A theoretical prediction. *Journal of Geophysical Research: Solid Earth*, 102(B7):14869–14881.

Olig, S., Gorton, A., Bott, J., Knuepfer, P., Smith, R., and Forman, S. (1995). Temporal clustering of large earthquakes during the latest Pleistocene on the southern Lost River fault zone, Idaho. In *Geological Society of America Abstracts with Programs*, volume 27, pages A–395.

Orr, T., Poland, M., Patrick, M., Thelen, W., Sutton, A., Elias, T., Thornber, C., Parcheta, C., and Wooten, K. (2015). Klauea's 5–9 March 2011 Kamoamoa Fissure Eruption and its Relation to 30+ Years of Activity from Pu'u 'O'o. In *Hawaiian Volcanoes*, pages 393–420. John Wiley & Sons, Inc.

Parsons, T., Thompson, G., and Smith, R. (1998). More than one way to stretch: A tectonic model for extension along the plume track of the Yellowstone hot spot and adjacent Basin and Range Province. *Tectonics*, 17:221–234.

Payne, S., McCaffrey, R., and King, R. (2012). A new interpretation of deformation rates in the Snake River Plain and adjacent basin and range regions based on GPS measurements. *Geophysical Journal International*, 189:101–122.

Pelton, J. and Smith, R. (1979). Recent crustal uplift in Yellowstone National Park. *Science*, 206(4423):1179–1182.

Richardson, J.A. (2016). Modeling the Construction and Evolution of Distributed Volcanic Fields on Earth and Mars, Doctoral Dissertation, University of South Florida.

Rodgers, D., Ore, H., Bobo, R., McQuarrie, N., , and Zentner, N. (2002). Extension and subsidence of the eastern snake river plain. In Bonnichsen, B., White, C., and McCurry, M., editors, *Tectonic and Magmatic Evolution of the Snake River Plain Volcanic Province*, pages 121–155. Idaho Geological Survey.

Rongo, R., Lupiano, V., Spataro, W., D'Ambrosio, D., Iovine, G., and Crisci, G. M. (2015). SCIARA: Cellular automata lava flow modelling and applications in hazard prediction and mitigation. *Geological Society, London, Special Publications*, 426.

Rowland, S., Gabriel, H., and Harris, A. (2005). Lengths and hazards of channel-fed lava flows on Mauna Loa (Hawaii), determined from thermal and downslope modeling with FLOWGO. *Bulletin of Volcanology*, 67:634–647.

Runge, M., Bebbington, M., Cronin, S., Lindsay, J., Kenedi, C., and Moufti, M. (2014). Vents to events: determining an eruption event record from volcanic vent structures for the Harrat Rahat, Saudi Arabia. *Bulletin of Volcanology*, 76(3):1–16.

Sandri, L., Jolly, G., Lindsay, J., Howe, T., and Marzocchi, W. (2012). Combining long- and short-term Probabilistic volcanic hazard assessment with cost-benefit analysis to support decision making in a volcanic crisis from the Auckland Volcanic Field, New Zealand. *Bulletin of Volcanology*, 74(3):705–723.

Shervais, J., Hanan, B., and Barry, B. (2008). Lithospheric topography, tilted plumes, and the track of the Snake River–Yellowstone hot spot. *Tectonics*, 27(5):17.

Shervais, J., Vetter, S., and Hanan, B. (2006). Layered mafic sill complex beneath the eastern Snake River Plain: evidence from cyclic geochemical variations in basalt. *Geology*, 34(5):365–369.

Siebert, L., Cottrell, E., Venzke, E., and Andrews, B. (2015). Chapter 12 - earth's volcanoes and their eruptions: An overview. In Sigurdsson, H., editor, *The Encyclopedia of Volcanoes (Second Edition)*, pages 239 – 255. Academic Press, Amsterdam, second edition edition.

Smith, R. and Sbar, M. (1974). Contemporary tectonics and seismicity of the western United States with emphasis on the Intermountain seismic belt. *Geological Society of America Bulletin*, 83:1205–1218.

Sobradelo, R. and Marti, J. (2010). Bayesian event tree for long-term volcanic hazard assessment: Application to Teide-Pico Viejo stratovolcanoes, Tenerife, Canary Islands. *Journal of Geophysical Research*, 115.

Sobradelo, R., Marti, J., Mendoza-Rosas, A., and Gomez, G. (2011). Volcanic hazard assessment for the Canary Islands (Spain) using extreme value theory. *Natural Hazards and Earth System Sciences*, 11:2741–2753.

Sparlin, M., Braile, L., and Smith, R. (1982). Crustal structure of the eastern Snake River Plain determined from ray trace modeling of seismic refraction data. *Journal of Geophysical Research*, 87:2619–2633.

Spear, D. and King, J. (1982). The Geology of Big Southern Butte, Idaho. In Bonnichsen, B. and Breckenridge, R. M., editors, *Cenozoic Geology of Idaho*. Idaho Bureau of Mines and geology.

Stout, M. and Nicholls, J. (1977). Mineralogy and petrology of Quaternary lava from the Snake River Plain, Idaho. *Canadian Journal of Earth Sciences*, 14:2140–2156.

Swanson, D., Duffield, W., Jackson, D., and Peterson, D. (1979). 1969-71 Mauna Ulu eruption of Kilauea Volcano, Hawai'i. *Geological Survey Professional Paper*, 1056.

Takada, A. (1994). The influence of regional stress and magmatic input on styles of monogenetic and polygenetic volcanism. *Journal of Geophysical Research: Solid Earth*, 99(B7):13563–13573.

Tanner, L. and Calvari, S. (2012). *Volcanoes: Windows on the Earth.* New Mexico Museum of Natural History & Science. p. 81.

Turcotte, D. and Schubert, G. (2002). *Geodynamics*, volume p.47. Cambridge University Press.

Turner, M., Cronin, S., Bebbington, M., and Platz, T. (2008). Developing probabilistic eruption forecasts for dormant volcanoes: A case study from Mt Taranaki, New Zealand. *Bulletin of Volcanology*, 70(4):507–515.

Valentine, G. and Perry, F. (2009). Volcanic risk assessment at Yucca Mountain, NV, USA: integration of geophysics, geology and modeling. In Connor, C. B., Chapman, N. A., and Connor, L. J., editors, *Volcanic and Tectonic Hazard Assessment for Nuclear Facilities.* Cambridge University Press.

Volcanism Working Group (1990). Assessment of potential volcanic hazards for New Production Reactor Site at the Idaho National Engineering Laboratory. *EG&G Informal Report*, EGG-NPR-10624.

Volentik, A., Connor, C., Connor, L., and Bonadonna, C. (2009). Aspects of volcanic ahazard assessment for the Bataan nuclear power plant, Luzon Peninsula, Philippines. In Connor, C. B., Chapman, N. A., and Connor, L. J., editors, *Volcanic and Tectonic Hazard Assessment for Nuclear Facilities.* Cambridge University Press.

Wand, M. and Jones, M. (1995). Kernel Smoothing. In Chapman and Hall, editors, *No. 60 in Monographs on Statistics and Applied Probability.*

Welhan, J., Gwynn, M., Payne, S., McCurry, M., Plummer, M., and Wood, T. (February 24-26, 2014). The Blackfoot Volcanic Field, Southeast Idaho: A Hidden High-Temperature Geothermal Resource in the Idaho Thrust Belt. In University, S., editor, *Thirty Ninth Workshop on Geothermal Reservoir Engineering - Stanford University, Stanford, CA.* Stanford, California.

Weller, J. (2004). Bayesian inference in forecasting volanic hazards: an example from Armenia. Master's thesis, University of South Florida.

Weren, S., Sakimoto, S., Hughes, S., and Gregg, T. (2004). Comparison of Plains Volcanism in the Tempe Terra Region of mars to the eastern Snake River Plain, Idaho with implications for geochemical constraints. In *Lunar and Planetary Science XXXV (2004)*, number Abstract 2090.

Wetmore, P. (1998). An assessment of physical volcano and tectonics of the central eastern Snake River Plain based on the correlation of subsurface basalts at an near the Idaho National Engineering and Environmental Laboratory, Idaho. Master's thesis, Idaho State University.

Wetmore, P., Hughes, S., Connor, L., and Caplinger, M. (2009). Spatial distribution of eruptive centers about the Idaho National Laboratory. In Connor, C., Chapman, N., and Connor, L. J., editors, *Volcanism, Tectonism, and Siting Nuclear Facilities.* Cambridge University Press.

Whitehead, R. (1994). Ground Water Atlas of the United States: Idaho, Oregon, Washington. *U.S. Geological Survey*, v.HA 730-H.

Williams, R. and Moore, J. (1983). Man against volcano: The eruption on Heimaey, Vestmannaeyjar, Iceland. *U.S. Geological Survey General Interest Publication*, page 27.

World Health Organisation (2013). Health risk assessment from the nuclear accident after the 2011 great east Japan Earthquake and Tsunami based on a preliminary dose estimation.

Wright, T., Takahashi, T., and Griggs, J. (1992). Hawai'i Volcano Watch; A Pictorial History, 1779–1991. *University of Hawai'i Press and Hawai'i Natural History Association: Honolulu.*

Yuan, H. and Dueker, K. (2005). Teleseismic P-wave tomogram of the Yellowstone plume. *Geophysical Research Letters*, 32(7).

Appendices

Appendix A - Geophysical Models of the ESRP
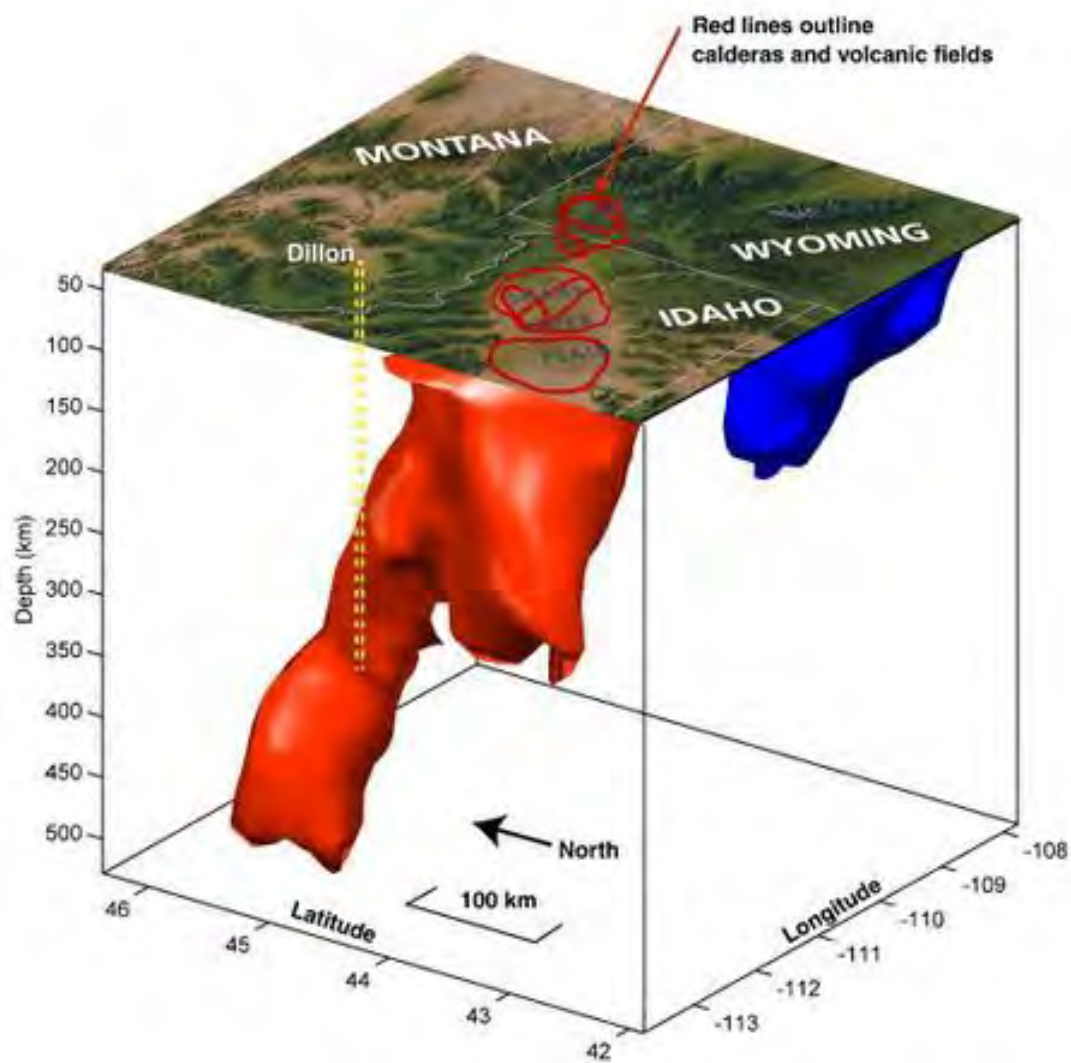
Figure 1: Seismic tomography reveals a conduit of warm mantle material (thermal plume) inclined to the northwest from beneath Yellowstone illustration from Yuan and Dueker (2005).
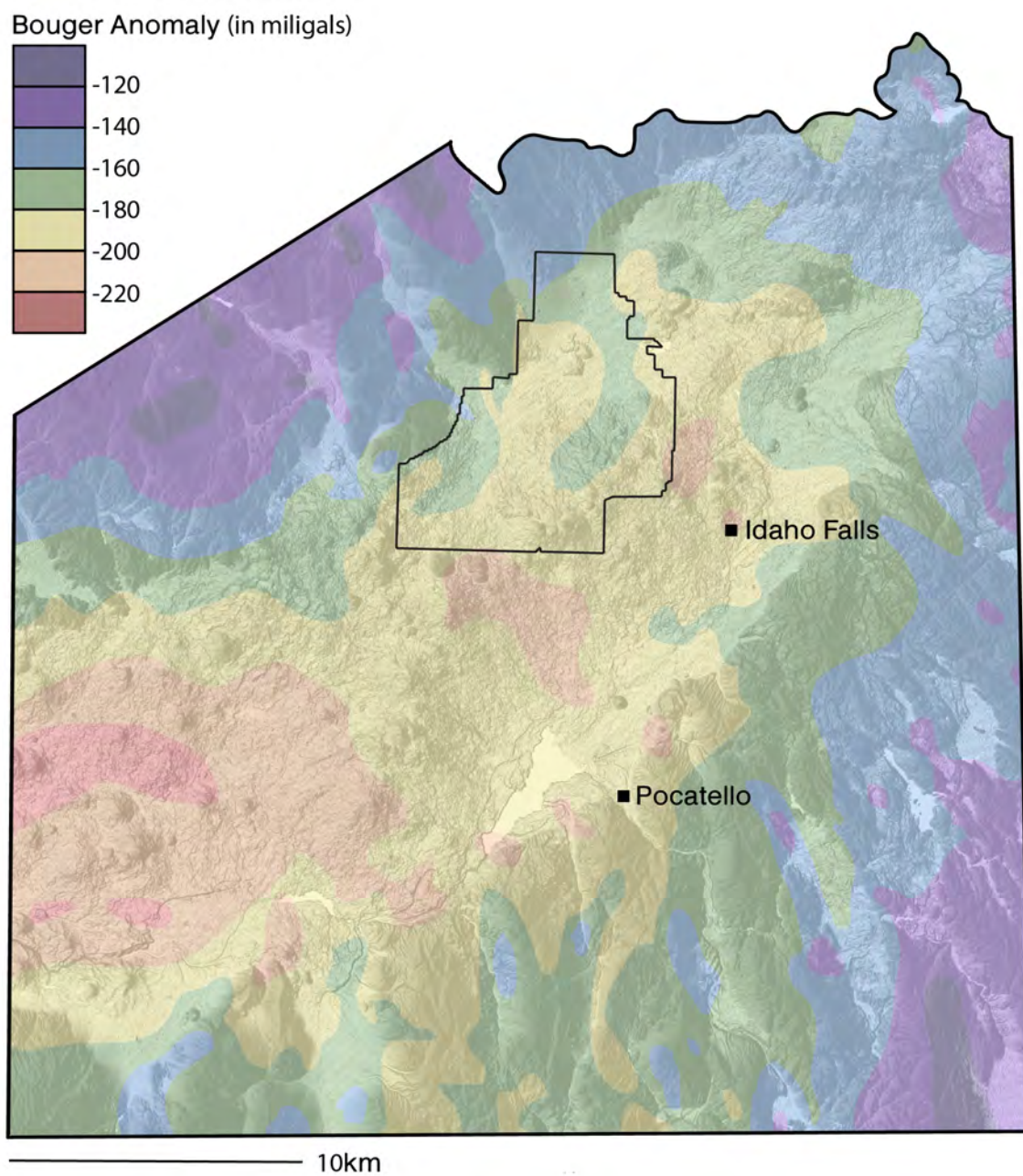
Figure 2: Bouger gravity anomaly map of southeastern Idaho (adapted from Mabey (1982)).

74
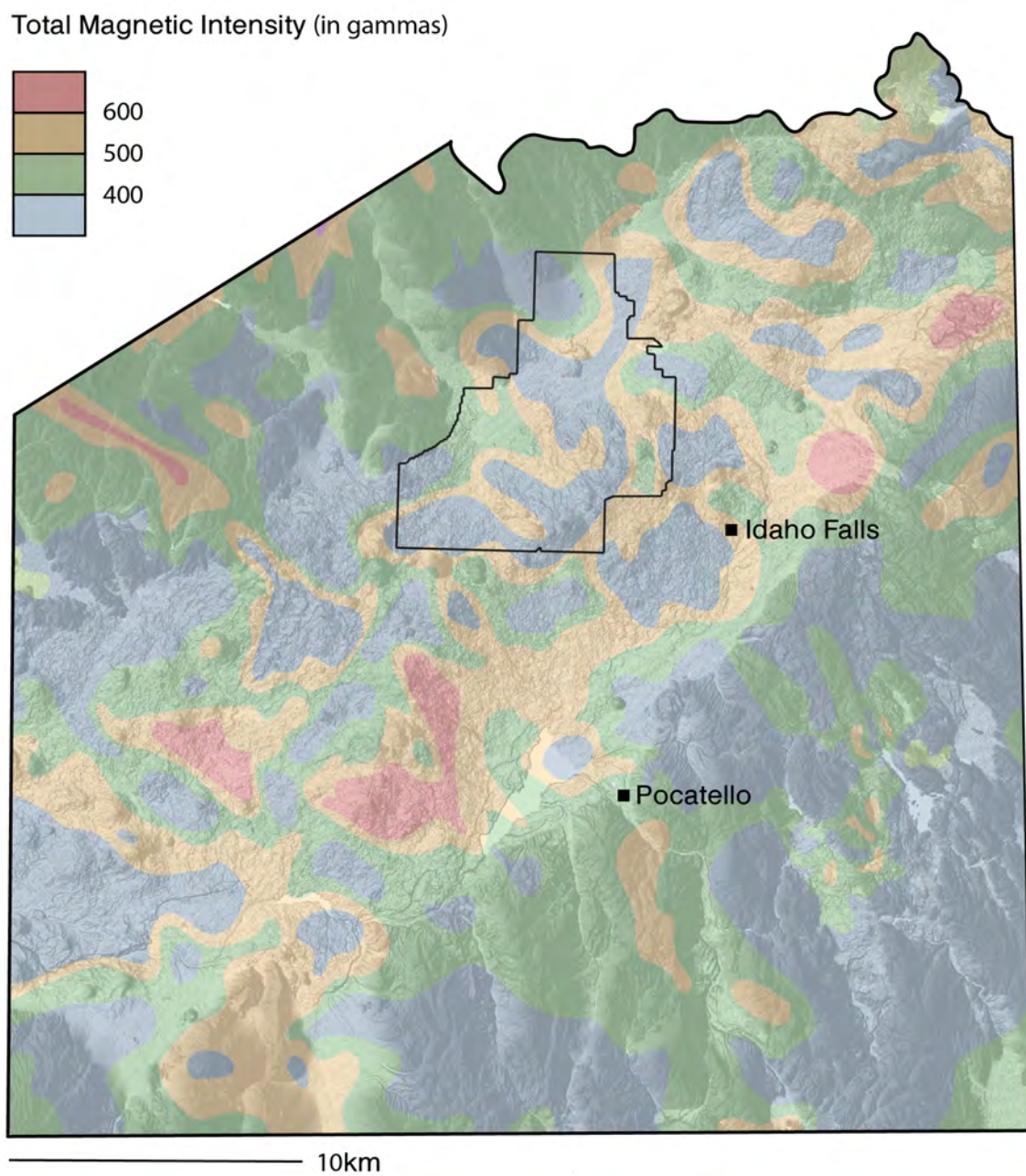
Figure 3: Total intensity aeromagnetic map of southeastern Idaho. Flight elevations were 2750 to 3700 meters above sea level. (adapted from Mabey (1982)).

Appendix B - INL Volcanic Hazard Assessment information from previous assessments

Phenomenon	Relative Frequency	Size or Area of Influence	Comments
Lava flow	Common	0.1 km² to 400 km² in area; up to 25 km in length based on sizes of ESRP lava flows of the past 400 Ka	Significant hazard; typical basaltic phenomenon; lava from fissures or shield volcanoes may inundate large areas downslope of vents
Ground deformation: fissuring, faulting, and uplift	Common; associated with virtually all shallow magma intrusion and eruption	Fissuring could affect areas to 2 x 10 km; minor tilting and broad uplift in areas to 5 x 20 km	Significant hazard; due to shallow dike intrusion; "dry" intrusion may occur without lava flows; affects smaller areas than for lava inundation
Volcanic earthquakes	Common; associated with magma intrusion before and during eruption	Maximum M = 5.5 and most events M < 4; ground vibration may affect facilities within 25 km	Low to moderate hazard; swarms of shallow earthquakes (< 4 km focal depth) occur as dikes propagate underground
Gas release (toxic and corrosive vapors)	Common; associated with fissuring and lava eruption	Restricted to near-vent areas; may affect several square-km area downwind	Low hazard; local plume of corrosive vapor, downwind from eruptive vent or fissure; cooled vapor may collect in local topographic depressions
Tephra fall (volcanic ash and bombs)	Common	Restricted to near-vent areas; may affect several square-km area downwind	Low hazard; basaltic eruptions are inherently nonexplosive and may form small tephra cones but little fine ash to be carried downwind
Base surge (ground-hugging blast of steam and tephra)	Rare	Effects limited to radius of several km from vent; < 10 km² area	Low hazard; steam explosions due to interaction between ascending magma and shallow ground water; water table too deep under most of INEEL (> 200 m)
Tephra flow (ground-hugging flow of hot, pyroclastic material)	Extremely rare	Near vent; may affect area < 1 km²	Very low hazard; as per tephra fall but affecting even smaller areas

Figure 4: A list of the volcanic phenomena present on the ESRP with recurrence intervals, magnitudes, and hazard potential (from Hackett et al. (2002)).
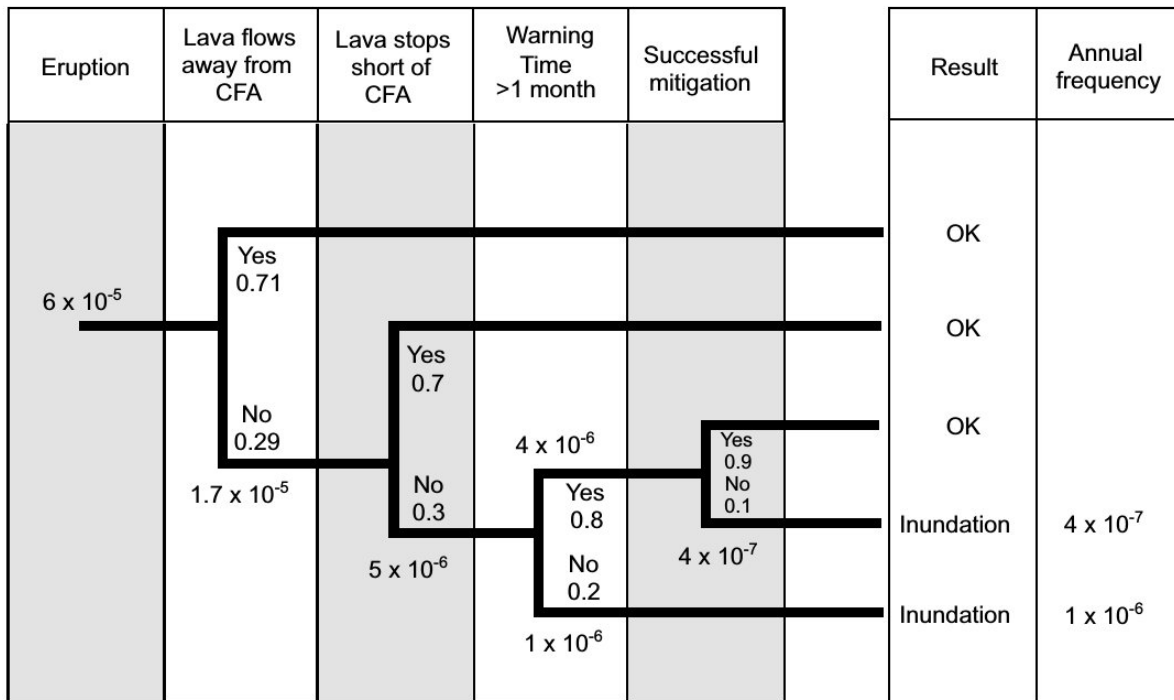
Figure 5: Lava flow event tree for the Central Facilities Complex of INL from Hackett et al. (2002). This study assumes a flow front advance rate of 2 km/day. This process differs from the one presented in this thesis by including flow direction, inclusion of precursory event monitoring, and mitigation potential.

Volcanic Zone or Borehole	Data Sources	Time Interval of Volcanism	Number of Vents, Fissures, or Flow Groups	Comments	Estimated Recurrence Interval
Great Rift (25 km southwest of INEEL)	Kuntz and others, 1986, 1988	2.1-15 Ka (radiocarbon dating)	> 100 vents; 8 Holocene eruptive periods (each lasting a few decades or centuries, and each including multiple flows and cones)	No impact on INEEL; most recently and frequently active of all ESRP rift zones; thus provides minimum recurrence for entire ESRP; most probable area of future ESRP volcanism	2 Ka (5 x 10^{-4}/year)
Axial Volcanic Zone (southern INEEL)	Kuntz and others 1986, 1994	5-730 Ka (K-Ar dating; radiocarbon data)	73 vents and fissure sets; 4 Holocene lava fields, 3 of them shared by volcanic rift zones, 45 cogenetic vent and fissure groups	Could affect much of southern INEEL; most recently and frequently active of all volcanic zones that could impact INEEL	16 Ka (6.2 x 10^{-5}/year)
Arco Volcanic Rift Zone (southwestern INEEL)	Kuntz, 1978; Smith and others, 1989; Kuntz and others, 1994	10-600 Ka (radiocarbon, K-Ar and thermoluminescence dating; paleomagnetic data)	83 vents and fissure sets; 2 Holocene lava fields, 35 cogenetic vent and fissure groups	Volcanism could affect southwestern INEEL	17 Ka (5.9 x 10^{-5}/year)
Lava Ridge-Hell's Half Acre Volcanic Rift Zone (includes Circular Butte/Kettle Butte volcanic rift zone) (north and eastern INEEL)	Kuntz and others, 1986, 1994	5 Ka-1.2 Ma (K-Ar dating; radiocarbon; paleomagnetic data)	48 vents and fissure sets; 1 Holocene lava field: Hell's Half Acre. 30 cogenetic vent and fissure groups	Could affect northern and eastern INEEL; extremely long eruptive history; includes oldest and youngest basalts in the INEEL area	40 Ka (2.5 x 10^{-5}/year)
Howe-East Butte Volcanic Rift Zone (central INEEL)	Kuntz, 1978, 1992; Golder Associates, 1992	230-730 Ka (K-Ar dating; paleomagnetic data)	7 vents and fissure sets; no Holocene features. 5 cogenetic vent and fissure groups	Old, poorly exposed, and sediment-covered; identified in part by subsurface geophysical anomalies	100 Ka (1.0 x 10^{-5}/year)
Borehole NPR SITE E (south-central INEEL)	Champion and others, 1988	230-640 Ka (K-Ar dating; paleomagnetic data)	9 lava-flow groups (each group contains multiple lava flows, erupted over a short time)	Dates from 600-foot interval of subsurface lavas give recurrence estimate consistent with surficial geology of the area	45 Ka (2.2 x 10^{-5}/year)
Borehole RWMC 77-1 (southwestern INEEL)	Kuntz, 1978; Anderson and Lewis, 1989	100-565 Ka (K-Ar and TL dating; paleomagnetic data)	11 lava-flow groups (each group contains multiple lava flows, erupted over a short time)	Dates from 600-foot interval of subsurface lavas give longer recurrence interval than nearby Arco and Axial zones, reflecting flow-group (subsurface) vs. vent-counting (surface geology) methods	45 Ka (2.2 x 10^{-5}/year)

¹ 16 vent/fissure groups in overlap zone of Axial Volcanic Zone and Arco Volcanic Rift Zone and Arco Volcanic Rift Zone are divided between the two zones. 17 vent/fissure groups in overlap zone of Axial Volcanic Zone and Lava Ridge-Hell's Half Acre Volcanic Rift Zone are divided between the two zones.

Figure 6: Exploration of hazard impact from various regions on the ESRP. The findings of which areas may threaten INL are similar to the ones presented in this thesis, although the approach diverges. The differentiation of volcanic regions is a vast departure from this thesis and has important implications for recurrence intervals and probabilities. From Hackett et al. (2002).

Appendix C - Vent and Event Information

Table 1: ESRP vent locations and ages

Easting*	Northing*	Flow Name	Age
292676	4813268	Craters of the Moon	2076
292880	4813035	Craters of the Moon	2076
293568	4812893	Craters of the Moon	2076
293780	4813779	Craters of the Moon	2076
294457	4813059	Craters of the Moon	2076
306907	4816489	Craters of the Moon	2076
307436	4815406	Craters of the Moon	2076
293584	4811017	Craters of the Moon	2100
294231	4811400	Craters of the Moon	2100
295880	4810687	Craters of the Moon	2100
296765	4808265	Craters of the Moon	2205
292194	4813819	Craters of the Moon	2300
292575	4814074	Craters of the Moon	2300
298306	4806335	Craters of the Moon	2400
307065	4792865	Craters of the Moon	3660
307165	4795428	Craters of the Moon	4510
307296	4794649	Craters of the Moon	4510
382670	4816284	Hell's Half Acre	5200
382957	4816090	Hell's Half Acre	5200
383369	4815625	Hell's Half Acre	5200
385138	4801140	Hell's Half Acre	5200
385931	4801039	Hell's Half Acre	5200
387558	4808185	Hell's Half Acre	5200
293229	4812366	Craters of the Moon	6020
294087	4809802	Craters of the Moon	6020
295982	4808249	Craters of the Moon	6020
296664	4807928	Craters of the Moon	6020
297884	4805878	Craters of the Moon	6020
297903	4805427	Craters of the Moon	6020
299932	4802618	Craters of the Moon	6020
299934	4804279	Craters of the Moon	6020
300560	4802594	Craters of the Moon	6020
300746	4802032	Craters of the Moon	6020
301551	4800141	Craters of the Moon	6020

ESRP vent locations and ages (Continued)

Easting*	Northing*	Flow Name	Age
302862	4800396	Craters of the Moon	6020
285706	4795390	Craters of the Moon	6500
285742	4795080	Craters of the Moon	6500
285869	4794118	Craters of the Moon	6500
291248	4813343	Craters of the Moon	6500
291564	4813014	Craters of the Moon	6500
292013	4813234	Craters of the Moon	6500
283740	4800918	Craters of the Moon	6600
283863	4799833	Craters of the Moon	6600
283867	4800667	Craters of the Moon	6600
284008	4800138	Craters of the Moon	6600
284112	4799310	Craters of the Moon	6600
285158	4798190	Craters of the Moon	6600
285603	4799253	Craters of the Moon	6600
285733	4799095	Craters of the Moon	6600
285816	4798845	Craters of the Moon	6600
285879	4798719	Craters of the Moon	6600
290977	4814316	Craters of the Moon	7360
281630	4767418	Craters of the Moon	7470
233302	4781687	Craters of the Moon	10130
309077	4785768	Craters of the Moon	11000
338324	4805497	North Robbers	11980
339107	4804900	North Robbers	11980
340488	4802420	South Robbers	11980
292363	4815759	Craters of the Moon	12010
347108	4802380	Cerro Grande	13380
281865	4766978	Craters of the Moon	15100
281947	4766728	Craters of the Moon	15100
297274	4809234	Craters of the Moon	15100
309701	4779823	Craters of the Moon	15100
268804	4778742	Craters of the Moon	34000
321280	4806552	Quaking Aspen Butte	40000
321618	4806322	Quaking Aspen Butte	40000
259684	4781257	Unnamed	49000
268530	4781598	Unnamed	49000
270347	4782890	Unnamed	49000
270625	4741008	Unnamed	49000
273246	4769825	Unnamed	49000
337820	4796207	Unnamed	55000
338468	4798710	Unnamed	55000
339280	4797857	Unnamed	55000
336020	4800995	Unnamed	56000
337698	4799218	Unnamed	56000
270444	4783783	Unnamed	57000

Easting*	Northing*	Flow Name	Age
295802	4787513	Unnamed	57000
296407	4787340	Unnamed	57000
296625	4786346	Unnamed	57000
296767	4785786	Unnamed	57000
296783	4785569	Unnamed	57000
296925	4785040	Unnamed	57000
317580	4809886	Fingers Butte	57000
317652	4809767	Fingers Butte	57000
295561	4784000	Unnamed	58000
295613	4784987	Unnamed	58000
295688	4784460	Unnamed	58000
328965	4815652	Coyote Butte	64000
329799	4815155	Coyote Butte	64000
321055	4765408	Unnamed	75000
321313	4764012	Unnamed	75000
321447	4762006	Unnamed	75000
307779	4771617	Unnamed	106000
308531	4771044	Unnamed	106000
310185	4773666	Unnamed	106000
328208	4780111	Unnamed	113000
274705	4777956	Unnamed	115000
274404	4781179	Unnamed	116000
309676	4834040	Unnamed	116000
309966	4833667	Unnamed	116000
310233	4833080	Unnamed	116000
335418	4813514	Unnamed	116000
336158	4813139	Unnamed	116000
338101	4812173	Unnamed	116000
258447	4768013	Unnamed	120000
258781	4766174	Unnamed	120000
270422	4795149	Unnamed	120000
272648	4788835	Unnamed	120000
323260	4797887	Unnamed	120000
302499	4792595	Unnamed	140000
307219	4788754	Unnamed	140000
307281	4788567	Unnamed	140000
324102	4762959	Unnamed	145000
324374	4764982	Unnamed	145000
305165	4780106	Unnamed	160000
305282	4779454	Unnamed	160000
307193	4782362	Unnamed	160000
316012	4773123	Unnamed	160000
316930	4772926	Unnamed	160000
367706	4802405	Taber Butte	165000

Easting*	Northing*	Flow Name	Age
277871	4802956	Unnamed	180000
278449	4802650	Unnamed	180000
329451	4773240	Unnamed	182000
348956	4808110	Unnamed	207000
352982	4807705	Unnamed	207000
356409	4808371	Unnamed	207000
357730	4807941	Unnamed	207000
358264	4808067	Unnamed	207000
324497	4783840	Unnamed	209000
288269	4799416	Unnamed	210000
288769	4797210	Unnamed	210000
289251	4798366	Unnamed	210000
289584	4798202	Unnamed	210000
290367	4796541	Unnamed	210000
290382	4793391	Unnamed	210000
290454	4799348	Unnamed	210000
290704	4792856	Unnamed	210000
290897	4792510	Unnamed	210000
291160	4795189	Unnamed	210000
291262	4794846	Unnamed	210000
291517	4794313	Unnamed	210000
291559	4794219	Unnamed	210000
291688	4794030	Unnamed	210000
292982	4796491	Unnamed	210000
293642	4795205	Unnamed	210000
295054	4803098	Unnamed	210000
295065	4803437	Unnamed	210000
295511	4713432	Unnamed	210000
295642	4800431	Unnamed	210000
295922	4800918	Unnamed	210000
308539	4804741	Unnamed	210000
308944	4816458	Saddle Butte	210000
309435	4815993	Saddle Butte	210000
310578	4815190	Saddle Butte	210000
313555	4812343	Cruthers Butte	210000
313924	4812493	Cruthers Butte	210000
314126	4812595	Cruthers Butte	210000
287105	4793956	Unnamed	220000
292927	4788773	Unnamed	220000
327117	4794454	Unnamed	220000
328602	4804081	Unnamed	220000
333878	4801764	Unnamed	220000
293040	4780618	Unnamed	230000
293125	4780430	Unnamed	230000

ESRP vent locations and ages (Continued)

Easting*	Northing*	Flow Name	Age
317766	4790593	Unnamed	230000
317918	4790373	Unnamed	230000
318094	4790183	Unnamed	230000
328778	4808650	Unnamed	230000
329495	4808459	Unnamed	230000
279628	4767884	Unnamed	240000
280982	4772786	Unnamed	240000
281551	4778879	Unnamed	250000
314144	4799243	Pratt Butte	263000
314275	4798970	Pratt Butte	263000
326058	4767069	Unnamed	265000
356661	4819951	Unnamed	268000
359003	4815676	Unnamed	268000
362256	4820097	Unnamed	268000
362715	4819659	Unnamed	268000
363009	4815784	Unnamed	268000
326532	4828611	Crater Butte	292000
326572	4828641	Crater Butte	292000
327428	4828139	Crater Butte	292000
330810	4821745	Crater Butte	292000
331238	4820891	Crater Butte	292000
338410	4831723	Crater Butte	292000
339401	4839249	Crater Butte	292000
371699	4824130	Unnamed	299000
335540	4806477	Big Southern Butte	300000
314249	4817770	Box Canyon	306000
328140	4768405	Unnamed	306000
329819	4761646	Unnamed	306000
331691	4763575	Unnamed	306000
331826	4761769	Unnamed	306000
334512	4787351	Unnamed	315000
388909	4827053	Kettle Butte	316000
307564	4813711	Unnamed	325000
307838	4813683	Huddle's Hole	325000
308352	4813141	Huddle's Hole	325000
315150	4816195	Wildhorse Butte	325000
315223	4816104	Wildhorse Butte	325000
358411	4849051	Unnamed	325000
359526	4846709	Unnamed	325000
361307	4844685	Unnamed	325000
370052	4834800	Unnamed	325000
370584	4835574	Unnamed	325000
370960	4834731	Unnamed	325000
372154	4832507	Unnamed	325000

Easting*	Northing*	Flow Name	Age
374257	4827258	Unnamed	325000
374970	4832536	Unnamed	325000
379458	4830687	Unnamed	325000
315514	4814408	Unnamed	330000
316394	4814457	Unnamed	330000
329548	4783750	Unnamed	330000
335315	4781644	Unnamed	330000
320883	4811965	Unnamed	335000
320991	4811886	Unnamed	335000
318965	4816821	Unnamed	340000
319575	4810059	Unnamed	340000
319660	4810404	Unnamed	340000
319675	4810823	Unnamed	340000
319826	4809758	Unnamed	340000
320174	4809533	Unnamed	340000
320938	4810102	Unnamed	340000
321366	4813461	Unnamed	340000
321372	4813434	Unnamed	340000
321751	4814999	Tin Cup Butte	340000
321826	4814874	Tin Cup Butte	340000
325743	4815254	Unnamed	340000
326279	4815352	Unnamed	340000
331966	4788620	Unnamed	340000
358949	4819179	Unnamed	350000
366395	4818336	Unnamed	358000
366406	4817175	Unnamed	358000
368396	4816665	Unnamed	358000
371562	4821633	Unnamed	358000
373234	4820571	Unnamed	358000
373288	4819582	Unnamed	358000
374882	4810644	Unnamed	358000
376624	4810166	Unnamed	358000
376745	4809832	Unnamed	358000
377322	4808513	Unnamed	358000
379200	4811354	Unnamed	358000
379464	4823314	Unnamed	358000
374071	4830327	Unnamed	362000
374519	4829981	Unnamed	362000
375876	4842527	Unnamed	362000
376057	4840707	Unnamed	362000
376574	4842372	Unnamed	362000
376890	4841709	Unnamed	362000
377229	4840319	Unnamed	362000
377538	4831958	Unnamed	362000

ESRP vent locations and ages (Continued)

Easting*	Northing*	Flow Name	Age
378259	4835352	Unnamed	362000
378920	4839263	Unnamed	362000
384258	4834881	Unnamed	362000
385891	4842499	Unnamed	362000
393052	4843882	Unnamed	362000
393224	4838597	Unnamed	362000
336227	4809915	Unnamed	390000
336881	4810249	Unnamed	390000
337294	4809885	Unnamed	390000
338338	4809970	Unnamed	390000
341195	4809176	Cedar Butte	400000
345260	4804898	Cedar Butte	400000
345436	4805693	Cedar Butte	400000
345460	4803730	Cedar Butte	400000
368193	4859447	Unnamed	400000
370782	4858423	Antelope Butte	423000
283233	4788423	Unnamed	425000
350667	4812263	Unnamed	454000
351288	4809586	Unnamed	454000
351391	4811041	Unnamed	454000
351438	4811995	Unnamed	454000
354003	4812130	Unnamed	454000
357327	4812814	Unnamed	454000
360168	4815418	Unnamed	454000
361546	4802441	Unnamed	454000
366407	4820306	Twin Butte	454000
367140	4812415	Unnamed	454000
325616	4792239	Unnamed	470000
328730	4791554	Unnamed	470000
331274	4792955	Unnamed	470000
292592	4801413	Unnamed	480000
292959	4800908	Unnamed	480000
359701	4816461	Alluvium and Colluvium	500000
348758	4837090	Unnamed	579000
382818	4810017	Unnamed	600000
383009	4798640	Baldy Knoll	600000
386618	4800064	Unnamed	600000
389259	4807542	Morgan's Pasture	600000
391709	4824844	Butterfly Butte	600000
392877	4823598	Butterfly Butte	600000
393376	4822509	Butterfly Butte	600000
317885	4820042	Sixmile and Tea Kettle Buttes	609000
318039	4820001	Sixmile and Tea Kettle Buttes	609000
323506	4827833	Sixmile and Tea Kettle Buttes	609000

ESRP vent locations and ages (Continued)

Easting*	Northing*	Flow Name	Age
323845	4818555	Sixmile and Tea Kettle Buttes	609000
323986	4818364	Sixmile and Tea Kettle Buttes	609000
324213	4826230	Sixmile and Tea Kettle Buttes	609000
324529	4818074	Sixmile and Tea Kettle Buttes	609000
325194	4825624	Sixmile and Tea Kettle Buttes	609000
325861	4819438	Sixmile and Tea Kettle Buttes	609000
326207	4817944	Sixmile and Tea Kettle Buttes	609000
326497	4818361	Sixmile and Tea Kettle Buttes	609000
326721	4818771	Sixmile and Tea Kettle Buttes	609000
326729	4817479	Sixmile and Tea Kettle Buttes	609000
341521	4829134	Unnamed	626000
342614	4828502	Unnamed	626000
352937	4867989	Lava Ridge	730000
384078	4866885	Table Butte	739000
384991	4861732	Table Butte	739000
385133	4867515	Table Butte	739000
385236	4866573	Table Butte	739000
385279	4867072	Table Butte	739000
386271	4868187	Table Butte	739000
386669	4868953	Table Butte	739000
387138	4868906	Table Butte	739000
387569	4869375	Table Butte	739000
387937	4866265	Table Butte	739000
388015	4871130	Table Butte	739000
388021	4870264	Table Butte	739000
388491	4866233	Table Butte	739000
388541	4870718	Table Butte	739000
388807	4867195	Table Butte	739000
388916	4864884	Table Butte	739000
388922	4872023	Table Butte	739000
389342	4868131	Table Butte	739000
389550	4865632	Table Butte	739000
389919	4863023	Table Butte	739000
390087	4865646	Table Butte	739000
390690	4882073	Table Butte	739000
390769	4865766	Table Butte	739000
391450	4865086	Table Butte	739000
391558	4866911	Table Butte	739000
391611	4882433	Table Butte	739000
391618	4865904	Table Butte	739000
391860	4864501	Table Butte	739000
392325	4873236	Table Butte	739000
392782	4867507	Table Butte	739000
393433	4871623	Table Butte	739000

ESRP vent locations and ages (Continued)

Easting*	Northing*	Flow Name	Age
393486	4867793	Table Butte	739000
394188	4868026	Table Butte	739000
394802	4867363	Table Butte	739000
394832	4868276	Table Butte	739000
353945	4867648	Lava Ridge	800000
354334	4867176	Lava Ridge	800000
352068	4870893	Lava Ridge	807000
358950	4868769	Richard Butte	807000
369458	4872463	Montview Butte	850000
355204	4854686	Unnamed	939000
355484	4858813	Unnamed	939000
355847	4860896	Unnamed	939000
368678	4854122	Circular Butte	1216000
214441	4772420	Unnamed	N/A
219534	4736858	Unnamed	N/A
219634	4744086	Unnamed	N/A
233966	4711026	Unnamed	N/A
234768	4721531	Unnamed	N/A
236364	4741883	Unnamed	N/A
237117	4725113	Unnamed	N/A
239376	4722124	Unnamed	N/A
244889	4716791	Unnamed	N/A
245531	4763115	Unnamed	N/A
248091	4734491	Unnamed	N/A
249961	4750895	Unnamed	N/A
253184	4705427	Unnamed	N/A
258147	4748144	Unnamed	N/A
260058	4707649	Unnamed	N/A
262901	4738285	Unnamed	N/A
270221	4762356	Unnamed	N/A
274000	4698202	Unnamed	N/A
274278	4699147	Unnamed	N/A
276001	4698758	Unnamed	N/A
278002	4749569	Unnamed	N/A
278710	4756923	Unnamed	N/A
288766	4749219	Unnamed	N/A
289453	4711320	Unnamed	N/A
290397	4743881	Unnamed	N/A
296178	4712988	Unnamed	N/A
297735	4730386	Unnamed	N/A
298235	4713821	Unnamed	N/A
298762	4828337	Unnamed	N/A
299139	4828172	Unnamed	N/A
299402	4730441	Unnamed	N/A

ESRP vent locations and ages (Continued)

Easting*	Northing*	Flow Name	Age
299978	4828456	Unnamed	N/A
300347	4735555	Unnamed	N/A
300438	4828071	Unnamed	N/A
300514	4712932	Unnamed	N/A
300625	4707763	Unnamed	N/A
303182	4708041	Unnamed	N/A
306446	4751927	Unnamed	N/A
312687	4738557	Unnamed	N/A
318190	4752620	Unnamed	N/A
320802	4728273	Unnamed	N/A
321664	4755821	Unnamed	N/A
322859	4737278	Unnamed	N/A
327084	4743226	Unnamed	N/A
327250	4748006	Unnamed	N/A
328584	4746728	Unnamed	N/A
329969	4745590	Unnamed	N/A
331905	4760272	Unnamed	N/A
332383	4731273	Unnamed	N/A
332920	4733276	Unnamed	N/A
336241	4741549	Unnamed	N/A
336644	4725383	Unnamed	N/A
337350	4740301	Unnamed	N/A
337555	4755225	Unnamed	N/A
339368	4730108	Unnamed	N/A
339812	4717768	Unnamed	N/A
341313	4726773	Unnamed	N/A
378500	4774116	Unnamed	N/A
396539	4878003	Unnamed	N/A
402222	4824208	Unnamed	N/A
402817	4829664	Unnamed	N/A
405316	4830797	Unnamed	N/A
406307	4868032	Unnamed	N/A
407347	4828342	Unnamed	N/A
407957	4905079	Unnamed	N/A
410773	4802133	Unnamed	N/A
411396	4870720	Unnamed	N/A
411659	4906842	Unnamed	N/A
412005	4905184	Unnamed	N/A
412270	4908598	Unnamed	N/A
412356	4870864	Unnamed	N/A
412977	4908421	Unnamed	N/A
414654	4903035	Unnamed	N/A
414920	4870700	Unnamed	N/A
415185	4870392	Unnamed	N/A

Easting*	Northing*	Flow Name	Age
415228	4835577	Unnamed	N/A
415401	4837214	Unnamed	N/A
415773	4902535	Unnamed	N/A
415831	4836999	Unnamed	N/A
416053	4857646	Unnamed	N/A
416509	4901269	Unnamed	N/A
416597	4907156	Unnamed	N/A
416626	4909981	Unnamed	N/A
416921	4903771	Unnamed	N/A
418275	4901416	Unnamed	N/A
418275	4905360	Unnamed	N/A
420629	4905390	Unnamed	N/A
420865	4904153	Unnamed	N/A
421071	4905125	Unnamed	N/A
421512	4904830	Unnamed	N/A
421512	4908421	Unnamed	N/A
421621	4846478	Unnamed	N/A
421669	4848350	Unnamed	N/A
421954	4900504	Unnamed	N/A
422193	4876871	Unnamed	N/A
422237	4876430	Unnamed	N/A
422341	4845373	Unnamed	N/A
422677	4876783	Unnamed	N/A
422725	4871296	Unnamed	N/A
422821	4865680	Unnamed	N/A
423190	4907008	Unnamed	N/A
423685	4841581	Unnamed	N/A
424397	4903889	Unnamed	N/A
425280	4898708	Unnamed	N/A
426074	4898296	Unnamed	N/A
426604	4906479	Unnamed	N/A
427458	4898502	Unnamed	N/A
427525	4859823	Unnamed	N/A
427723	4898414	Unnamed	N/A
428959	4901593	Unnamed	N/A
429312	4901387	Unnamed	N/A
431343	4901151	Unnamed	N/A
431755	4900857	Unnamed	N/A
432520	4899474	Unnamed	N/A
433227	4899268	Unnamed	N/A
433285	4907627	Unnamed	N/A
433550	4905184	Unnamed	N/A
433609	4907833	Unnamed	N/A
434463	4905978	Unnamed	N/A

ESRP vent locations and ages (Continued)

Easting*	Northing*	Flow Name	Age
434522	4901357	Unnamed	N/A
434698	4904536	Unnamed	N/A
435110	4901210	Unnamed	N/A
435375	4898973	Unnamed	N/A
435934	4903241	Unnamed	N/A
437524	4903771	Unnamed	N/A
437553	4899768	Unnamed	N/A
437642	4906273	Unnamed	N/A
437818	4907980	Unnamed	N/A
437965	4903535	Unnamed	N/A
440349	4905919	Unnamed	N/A
440703	4906655	Unnamed	N/A
441615	4899621	Unnamed	N/A
442057	4909069	Unnamed	N/A
442119	4880129	Unnamed	N/A
442145	4905390	Unnamed	N/A
443469	4907833	Unnamed	N/A
443999	4909628	Unnamed	N/A
444087	4907627	Unnamed	N/A
444264	4904183	Unnamed	N/A
444588	4909363	Unnamed	N/A
445441	4902446	Unnamed	N/A
446354	4910040	Unnamed	N/A
446501	4906479	Unnamed	N/A
447914	4906832	Unnamed	N/A
448561	4906773	Unnamed	N/A
452064	4904124	Unnamed	N/A
454242	4903800	Unnamed	N/A
465014	4903241	Unnamed	N/A
467869	4904124	Unnamed	N/A
471019	4901181	Unnamed	N/A
474256	4910894	Unnamed	N/A

* Eastings and northings reported in UTM Zone 12 coordinates.

Table 2: ESRP event group information

Age Block	Age	# Vents	# Events
1	2,076	7	2
2	2,100	3	1
3	2,301	4	2
4	3,660	1	1
5	4,510	2	1
6	5,200	6	2
7	6,020	12	4
8	6,500	6	2
9	6,600	12	1
10	7,415	2	2
11	12,987	11	9
12	38,000	2	2
13	49,000	5	4
14	55,000	3	1
15	56,000	2	1
16	57,000	9	3
17	58,000	3	1
18	64,000	2	1
19	75,000	3	1
20	115,176	17	8
21	140,000	3	1
22	145,000	2	1
23	160,833	6	3
24	180,667	3	2
25	209,529	34	11
26	220,000	5	3
27	230,000	7	3
28	240,000	2	1
29	250,000	1	1
30	266,375	8	5
31	292,000	7	4
32	299,500	2	2
33	306,000	5	3
34	315,500	2	2
35	325,000	15	6
36	330,000	4	2
37	335,000	2	1
38	340,000	14	5
39	350,000	1	1
40	358,000	12	4
41	362,000	14	7
42	390,000	4	1
43	400,000	5	3
44	424,000	2	2

ESRP event group information (Continued)

Age Block	Age	# Vents	# Events
45	454,000	10	6
46	470,000	3	1
47	480,000	2	1
48	500,000	1	1
49	579,000	1	1
50	600,000	7	3
51	609,000	13	3
52	626,000	2	1
53	738,750	36	10
54	800,000	2	1
55	807,000	2	1
56	850,000	1	1
57	939,000	3	2
58	1,216,000	1	1
no age	N/A	151	97

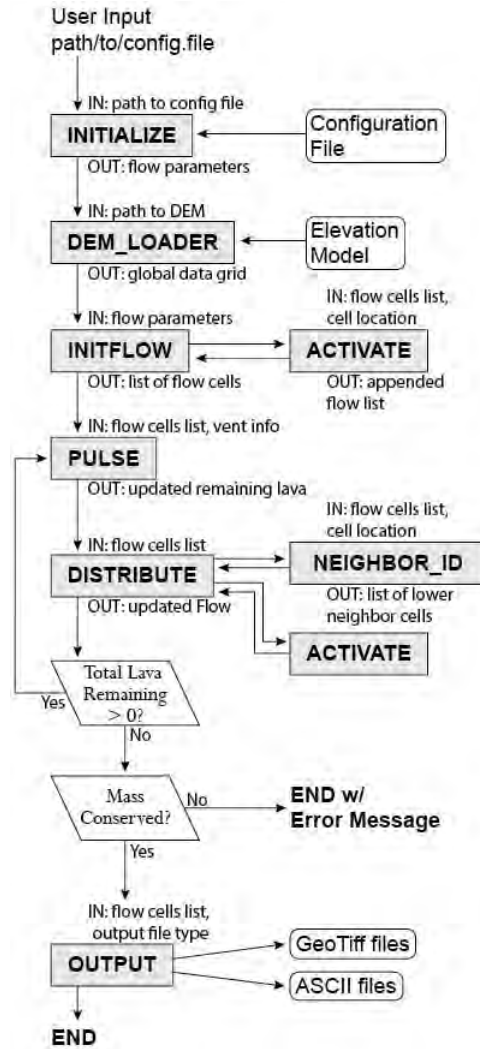# Appendix D - MOLASSES Workflow and Cell Behavior

Figure 7: High-level workflow for MOLASSES lava flow simulator. This flowchart illustrates the decisions from inputs to total execution for a single lava flow. This process is iterated over thousands of times to complete the probabilistic assessment. This code is available at https://github.com/USFvolcanology/molasses. At the time of publication a probabilistic version of MOLASSES was nearing completion (Richardson, 2016).
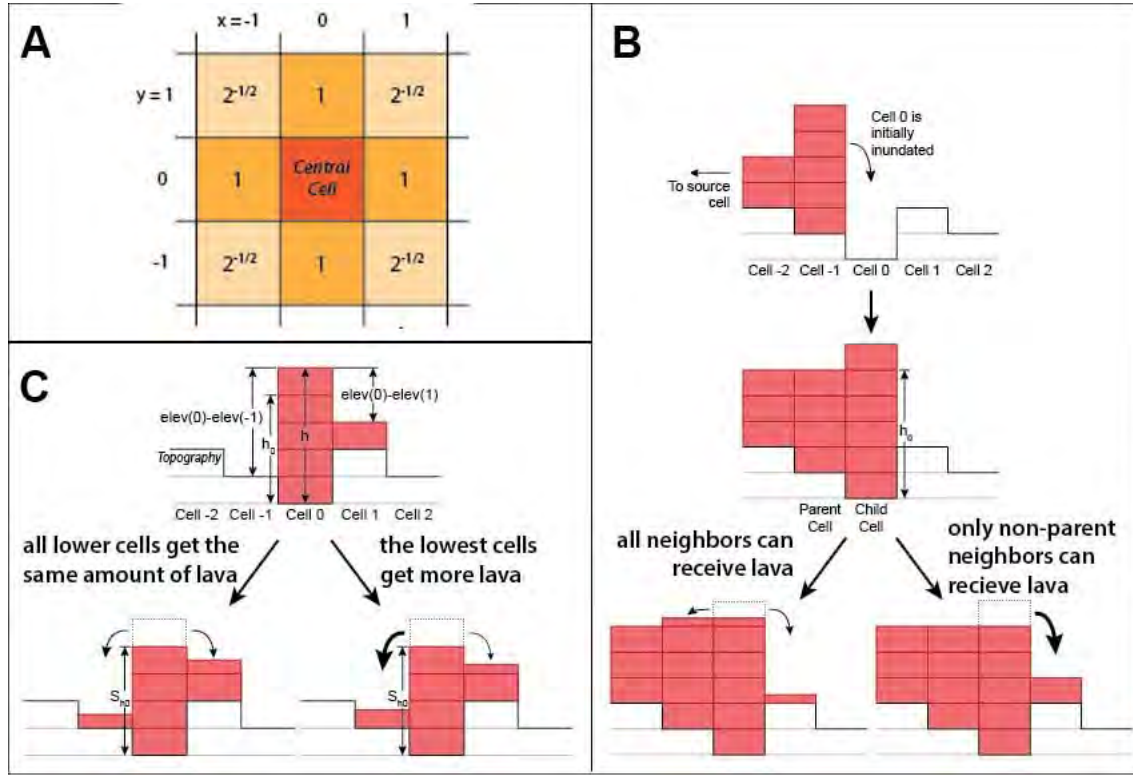
Figure 8: MOLASSES cell behaviors from Richardson (2016). **A:** The sharing proportions of lava between a parent cell and its 8 neighbors on a flat surface. **B:** The distribution relationship between parent cells and receiver cells. The model on the right illustrates the distribution pattern of a parent cell that is able to receive lava. The model on the left illustrates a distribution pattern of a parent cell unable to receive lava. The right model, parent-less sharing, was used for this thesis. **C:** The distribution relationship between upslope parents and downslope neighbors. The model on the left distributes the same amount of lava to the neighbors regardless of slope difference. The model on the right distributes more lava to the cell with the greatest difference in elevation between the parent and receiving cells. The model on the right, slope proportional spreading, was used for this thesis.